Precision and Selectivity: New Techniques in Image Guided Focused Ultrasound

By

Vandiver L. Chaplin

Dissertation
Submitted to the Faculty of the
Graduate School of Vanderbilt University
in partial fulfillment of the requirements
for the degree of

DOCTOR OF PHILOSOPHY
In

Chemical and Physical Biology

May 11, 2018

Nashville, Tennessee

Approved:
William Grissom, PhD
Charles Caskey, PhD
Daniel Brown, MD
Michael Miga, PhD
Brett Byram, PhD

TABLE OF CONTENTS

Page

LIST OF FIGURES

LIST OF ACRONYMS

1. FUS – Focused ultrasound
2. HIFU – High intensity focused ultrasound
3. PAM – Passive acoustic mapping
4. MR – Magnetic resonance
5. MRgFUS – Magnetic resonance-guided focused ultrasound
6. ARFI – Acoustic radiation force imaging
7. BBB – Blood Brain Barrier
8. NPV – Non-perfused volume
9. FLE – Fiducial localization error
10. FRE – Fiducial registration error
11. TRE – Target registration error
12. GPU – Graphics processing unit
13. dB – Decibels
14. Pa – Pascals
15. V – Volts
16. W – Watts

CHAPTER 1
INTRODUCTION

Focused ultrasound (FUS) is a non-invasive technology with a growing body of applications in interventional therapy and preclinical research. FUS uses geometrically focused transducers to make spatially convergent acoustic fields. The region where acoustic waves reach maximal convergence is the focus, and in general the goal of FUS treatments is to arrange transducers so that maximum energy delivery occurs in a specific target tissue. Broadly speaking, FUS can be applied in either destructive (e.g., thermal necrosis, mechanical liquefaction for tissue ablation) or non-destructive (e.g. neuromodulation, immune stimulation, drug delivery) modalities [1]–[6]. The destructive regime is often termed high intensity focused ultrasound (HIFU). With proper tuning of parameters such as transducer geometry, wave power, frequency and duty factor, FUS devices can be used to achieve a variety of pressure and heat-related biological effects at the acoustic focus. In this respect FUS is somewhat unique among bioengineering tools in that is at once non-invasive, spatially precise, and to a degree biologically selective. However, significant work remains to realize its full potential.

The majority of ongoing FUS research and development can be thought of as pursuant to one (or more) of the critical attributes of non-invasiveness, precision, and selectivity. For example, array steering and aberration-correction methods have been developed to account for bone (e.g., skull, ribs) in the sonication path, which would otherwise require an invasive surgery (craniotomy or costectomy) or contraindicate FUS altogether [7], [8]. Spatial precision has been well established in thermal therapy, but in neuromodulation it is less understood whether there is a direct mapping between the targeted neurons and observed brain neuronal modulation [9]–[11]. Finally, biological selectivity and tunability of FUS treatments, particularly in the low-intensity regime, is commonly hypothesized but remains practically elusive. One need only observe the variety of parameters, devices, experimental models and results that have been published – in particular for neuromodulation – to see that the field is in an ongoing process of discovery [12]. This makes it difficult to point to reliably tunable FUS parameters that have had widely reproducible success. A notable exception is thermal ablation with high-intensity focused ultrasound[1] (HIFU), which is by far the most mature FUS application and is beginning to see regular clinical use [13], [14].

The work presented in this dissertation fits into the broader context of FUS research through three original contributions: 1) a tunable hyperthermia treatment method that reduces potentially damaging acoustic cavitation effects, 2) a novel technique for optically-guided calibration and targeting of a FUS transducer that provides real-time beam projection and unprecedented beam mapping next to the interior surface of an *ex vivo* skull, and 3) a new transducer for aberration-corrected neuromodulation. Chapter 1 introduces key concepts in acoustic propagation and interaction of ultrasound with cells and tissues. Chapter 2 explains relevant technologies and prior development work that was used as a starting point for the original methods presented in subsequent chapters. Chapter 3 presents original work combining multi-focal HIFU with passive acoustic mapping to reduce cavitation. Chapter 4 presents novel development, validation, and *in vivo* use of image guided FUS with passive optical tracking. Chapter 5 develops requirements, simulation-based design, and characterization of a new phased-array transducer for transcranial FUS.

---

[1] Due to the prevalence of HIFU treatments, people outside the field tend to use the terms HIFU and focused ultrasound interchangeably. However, HIFU is actually a subset of focused ultrasound that uses high-intensities and long pulses / continuous wave and generally implies a thermal ablation procedure. In this document FUS will refer to any application of focused ultrasound.

1.1 Overview of acoustic physics

Acoustic waves are longitudinal travelling waves in which alternating phases of compression and rarefaction propagate from a source through a medium. In the wave compression phase the medium at a fixed point experiences an upward perturbation in density (units such as kg / ml) and pressure (typically in units of Pascals, symbol Pa) above ambient levels. In the rarefaction phase, the medium is expanded and experiences density and pressure below ambient. In ultrasound such waves are typically generated by vibrations of a piezoelectric transducer coupled to the skin via gel or water. If one were to measure the rate of alternation between positive and negative phases at an arbitrary fixed point in the wave path, a frequency spectrum would be observed that is similar to the transducer's vibration, but modified by frequency-dependent attenuation as the wave passes through multiple layers of tissue. Transducers and materials are explained in more depth in Chapter 2, but in general there is sub-linear relationship between the driving voltage amplitude applied to piezo elements, and peak acoustic pressure experienced by the medium. At low pressure the relationship is linear, but at high pressure it becomes sub-linear due to decreasing ability of the medium to support waves. Eventually, if the rarefactional pressure becomes large enough, the medium can pass phase transition and undergo spontaneous vaporization.

At low pressure with no absorption, acoustic waves in a homogeneous medium follow the basic wave equation:

$$\nabla^2 p - \frac{1}{c_o^2}\frac{\partial^2 p}{\partial t^2} = 0 \qquad (1)$$

where $p(\mathbf{x}, t)$ is the scalar pressure and c_o the uniform speed of sound of the medium. This equation can be derived by treating compression and rarefaction perturbations as small, keeping only 1st order terms. In the case of infinite media without boundaries this equation admits solutions of the form

$e^{j(\mathbf{k}\cdot\mathbf{x}-\omega t)}$, where $c_o = \omega/k$ and ω is the wave angular frequency (rad /s). A foundational and extremely useful result arises from the fact that the wave equation has a Green's function, meaning the following equation:

$$\nabla^2 p - \frac{1}{c_o^2}\frac{\partial^2 p}{\partial t^2} = \delta(\mathbf{x}-\mathbf{x_o})\delta(t-t_o)$$

has a unique solution. It is of the form:

$$G(\mathbf{x},\mathbf{x_o},t,t_o) = \frac{\delta(t-t_o-\frac{|\mathbf{x}-\mathbf{x_o}|}{c_o})}{4\,\pi|\mathbf{x}-\mathbf{x_o}|}$$

By Green's theorem, equation (1) with a non-zero right hand side $f(\mathbf{x},t)$, has the general solution

$$p(\mathbf{x},t) = \int G(\mathbf{x},\mathbf{x_o},t,t_o)\,f(\mathbf{x},t)\,d^3\mathbf{x_o}\,dt_o$$

Being a partial differential equation, the solution $p(\boldsymbol{x},t)$ is not fully defined unless initial and boundary conditions are specified. In a series of developments in scalar diffraction theory, Gustav Kirchoff, John William Strutt (the 3rd Lord Rayleigh), and Arnold Sommerfeld progressively developed a general method for solving the wave equation within a section of homogenous medium surrounded on all sides by an arbitrary boundary, assuming either the pressure or it's derivative are specified everywhere on the boundary [15]. Taking the time-domain Fourier transform of equation (1) yields the Helmholtz equation for $P(\mathbf{x},\omega)$:

$$\nabla^2 P + \frac{\omega^2}{c_o^2}P = 0$$

Applying Green's theorem and Neumann boundary conditions specifying the pressure gradient along the boundary, $\nabla P(\mathbf{x}',\omega)$ = $j\rho\omega\,\mathbf{u}(\mathbf{x}',\omega)$, it can be shown that the acoustic pressure inside the boundary is:

$$P(\mathbf{x},\omega) = j\,\frac{\rho\omega}{2\pi}\iint \frac{e^{j\,\omega\frac{|\mathbf{x}-\mathbf{x}'|}{c_o}}}{|\mathbf{x}-\mathbf{x}'|}\mathbf{u}(\mathbf{x}',\omega)\cdot\hat{\mathbf{n}}\,dA' \qquad (2)$$

where the integral is taken over the bounding surface, $\mathbf{u}(\mathbf{x}',\omega)$ is the surface velocity of the vibrating transducer along the boundary, and $\mathbf{n}$ is the surface normal vector. This is known as the frequency domain Rayleigh or Rayleigh-Sommerfeld integral. In many instances of low-pressure ultrasound modelling, equation (2) is a reasonably accurate approximation to the acoustic field since the speed of sound and density typically vary by no more than 10% in soft tissue [16]. In practice, equation (2) is greatly simplified by assuming that each transducer element is flat, and has a uniform surface velocity and area A. An ad-hoc de-rating factor for exponential attenuation, $e^{-\alpha|\mathbf{x}-\mathbf{x}'|}$ is also frequently applied [17]. The resulting equation is:

$$P(\mathbf{x},\omega) = j\,\frac{\rho\omega}{2\pi}\frac{e^{j\,\omega\frac{|\mathbf{x}-\mathbf{x}'|}{c_o}}\,e^{-\alpha|\mathbf{x}-\mathbf{x}'|}}{|\mathbf{x}-\mathbf{x}'|}uA \qquad (2b)$$

where α is the attenuation factor and has units of nepers/distance. This equation is used in Chapter 5 in the optimized design of a new phased-array transducer.

Equation (2b) is accurate in the linear approximation with nearly homogenous media. But at higher pressures and in highly absorptive media, terms of higher order must be included. A modified form of the Westervelt equation has become a standard theoretical model for acoustic waves in non-linear, non-homogenous, absorbing media [18]. Absorption follows a frequency-dependent power law with $\alpha = \alpha_0\omega^{\gamma}$. The equation for pressure is:

$$\nabla^2 p - \frac{1}{c_o^2}\frac{\partial^2 p}{\partial t^2} + \frac{\beta_o}{\rho_o c_o^4}\frac{\partial^2 p^2}{\partial t^2} = -\left\{\tau_o\frac{\partial}{\partial t}(-\nabla^2)^{\frac{\gamma}{2}} + \eta_o(-\nabla^2)^{\frac{\gamma+1}{2}}\right\}p \qquad (3)$$

The left hand side describes wave propagation with a non-linear term appended. The right hand side contains fractional derivative operators that account for frequency-dependent absorption and dispersion in heterogeneous media. $\tau_o = -2\,\alpha_o {c_o}^{\gamma-1}$ is the coefficient of absorption and $\eta_o = 2\,\alpha_o {c_o}^{\gamma}\,\tan\left(\frac{\pi\gamma}{2}\right)$ the coefficient of dispersion. The derivation and a method for numerically solving this equation are described in Treeby et al., and the solution implemented in the acoustic simulation package k-Wave [19].

As acoustic waves propagate, a portion of their energy is dissipated into the medium through viscous heating. Since absorption increases with frequency, higher sonication frequency results in more heating and reduced wave penetration. Thermal HIFU generally uses frequencies in the 0.65 – 1.2 MHz range. Lower intensity FUS may use frequencies down to 0.2 MHz since it has better transmission through multiple tissue layers. Regardless of vibrational frequency spectrum, the time-averaged rate of energy flux through an infinitesimal cross-section is:

$$I = \frac{1}{\rho c \tau} \int_0^{\tau} p(t)^2 dt$$

This is typically referred to as wave intensity and commonly has the unit $\mathrm{W/cm^2}$. To first order, $I = I_o e^{-2\alpha x}$, with intensity decreasing along the propagation path due to absorption. The specific rate of absorbed thermal energy is

$$\frac{dQ}{dt} = 2\alpha I$$

which has units of $\mathrm{W/cm^3}$. Some commonly accepted values for the absorption coefficient in various tissues at 1 MHz are $\alpha =$0.3 dB/cm (brain), 1.0 dB/cm (skeletal muscle), 0.8 dB/cm (bone), 0.6 dB/cm (liver) [16]. These equations can be used to model FUS treatments in order to examine off-target heating and power safety limits [16], [20]–[22].

1.2 Clinical status of focused ultrasound procedures

Therapeutic focused ultrasound has been explored since the 1940s, with early experiments showing spatially selective focal destruction in cerebral tissue for treatment of tumors and motion disorder [23], [24]. Development of MRI--and compatible transducers--has helped increase clinical feasibility of FUS therapy by offering image guidance for tissue-selective targeting, feedback via real-time MR thermometry, and immediate post-treatment assessment with contrast enhanced MRI [25]–[31]. Currently, ablative procedures are the only FUS treatments that have received (or are in latter stages of) regulatory approval, though sub-lethal acoustic treatments are being explored in both pre-clinical (e.g., the work presented in this dissertation) and early-to-middle phase human studies, for example to activate drug carriers or modulate biological processes [32]. In the last two decades MR-guided acoustic thermal ablation has been shown to be a safe and effective treatment for a variety of conditions including essential tremor, uterine fibroids, palliation of bone metastases, and benign and malignant breast tumors [13], [14], [33], [34]. Additional indications, such as cancers of the prostate, liver and kidney are currently under investigation, but so far have had mixed results [32], [35]–[37].

Non-thermal ablation (lithotripsy and histotripsy) uses short high-pressure pulses to induce acoustic shocks and cause tissue lysis, and can be guided with an ultrasound imaging probe [38]–[40]. Lithotripsy for focal disruption of renal calcifications (kidney stones) dates to the late 1970s, but has become less common because of improving endoscopic techniques that can remove large masses in a single procedure [41]. Histotripsy, which uses even shorter pulses and higher pressure to achieve soft tissue disruption, is being investigated for a variety of conditions such as tumor destruction and thrombolysis [38], [42], [43]. Perhaps due to its complicated nonlinear shock physics that makes accurate modelling a challenge, and the competing thermal treatments already accepted by the interventional community, mechanical ablation beyond renal lithotripsy represents a small fraction of current FUS research and is still in clinical trials. The remainder of this section will focus on thermal and sub-ablative uses of FUS, describing successes and limitations of the most common FUS procedures.

1.2.1 Background: Thermal Ablation

In thermal ablation the goal is to reach a lethal thermal dose inside targeted tissue volumes via conversion of input energy into heat. Rising temperature creates a variety of effects in living tissue that become non-reversible as heating accumulates, including heat shock protein formation, enzyme and protein conformational modification, pH and biochemical kinetic changes [44]. With sufficient thermal dose, cellular necrosis begins. An empirically-derived metric for thermal dose is the “cumulative equivalent minute at 43° C” or CEM43. This normalizes treatment temperature and duration to a cumulative scale upon which hyperthermia-induced cell death and coagulative necrosis have been reliably quantified [16], [45]. A CEM of 240 has been shown to correlate to >99% cell death in histological samples following *in vivo* ablation [26]. Common ablation technologies include radiofrequency (RF) and microwave (MW) ablation. In RF ablation a set of electric diode probes are inserted around the target and emit alternating current that is absorbed in the tissue. In MW ablation electromagnetic waves transmitted by antennae are absorbed [46]. By contrast, HIFU ablation heats tissue via direct loss of acoustic wave energy to shear vibration and viscous heating [16]. HIFU can be performed as a completely non-invasive procedure using only extracorporeal devices, whereas RF and MW ablation are minimally-invasive or open surgical procedures. In addition, MR-compatible HIFU transducers allow real-time temperature maps using MR thermometry during treatment, enabling feedback-controlled procedures that can achieve technical treatment success (reaching a CEM of 240 or more over 90% of the target volume) with a minimal amount of excess energy [36]. RF and MW ablation use probe-mounted temperature sensors that provide only rough estimates of temperature in the treatment volume [47]. These are often cited as the major advantages of HIFU over alternative ablation techniques.

Despite these promising advantages of HIFU, in practice a number of difficulties have been encountered that have so far limited its success to a select few conditions where it offers a unique value proposition, and its relative benefit and cost-effectiveness are still being evaluated. In prostate ablation for example, a significant portion of HIFU procedures experience local treatment failure and require salvage treatment. This is most likely due to the difficulty of detecting tumor borders and overall disease burden (which is multi-focal in roughly 75% of cases) via biopsy or MRI, and not the device or physics underlying this treatment approach [48]. However it does lead to valid skepticism about the overall utility and cost-effectiveness of MR-guided HIFU vs. radiation therapy or prostatectomy.

MR-guided HIFU is more promising for treatment of essential tremor and symptomatic uterine fibroids, where ablation targets are easily identified in a pre-treatment MR scan (typically some variant of a T2 weighted sequence). However two practical difficulties are outstanding: 1) the long treatment times required to reach technical ablation success, and 2) pre-focal heating or cavitation that can cause damage to healthy tissues along the treatment path. These two problems are somewhat related, in that pre-focal heating necessitates cooling periods interspersed between successive sonications, typically 4-5 times the duration of heating [34], [49], [50]. However long treatment times are also a result of the practical difficulty in working with awake patients that must remain stationary for long periods in the MR bore to maintain good acoustic coupling and transducer positioning, which leads to discomfort. Patients remain awake to report pain or other sensations and can abort the procedure with a push-button control, or respond to prompts during functional neurosurgery. In practice, occasional movement occurs in procedures that don’t use stereotaxis (e.g., uterine / abdominal), and the tedious process of removing air bubbles or reapplying coupling gel may need to be repeated. Reported treatment times for uterine fibroids and essential tremors are between two to three hours, and as high as four hours in some experimental liver and kidney procedures [50], [51]. Detailed consideration of essential tremor and fibroid ablation with HIFU are discussed in the following sections.

1.2.2 Essential Tremor: Ablation of the thalamus

Essential tremor (ET) is the most common adult movement disorder, estimated to affect between 0.4% - 4% of the global population [52]. The condition results in progressively worsening tremors that typically affect hands, especially in the dominant arm, to the point of partial or complete loss of use in routine activities such as self-feeding and care. A typical diagnosis assesses the location of tremors and their severity using a tremor rating score (the Clinical Rating Scale for Tremor, CRST) [13]. The majority of patients can be treated medically with regular doses of primidone or propranolol that improve tremor score by 60% in about half of all cases. However surgical interventions are considered in the event of side-effects or medication resistance. Surgical options are RF ablation or deep brain stimulation (DBS), both targeting the Vim nucleus in the thalamus, which is a central relay in neural motor control. Both destructive RF ablation and non-destructive DBS have been shown to suppress tremors with 80-90% effectiveness [13], [53]. But due to the highly invasive nature of these procedures, few patients elect to undergo them, resulting in some 25-30% of patients with no treatment option [54].

Impact and Limitations: Transcranial HIFU for ablation of the Vim nucleus offers the chance for these patients to receive treatment if first-line drugs are ineffective or cause side effects. The procedure has recently received FDA approval using the 1000-element MR-compatible phased array manufactured by InSightec (Haifa, Isreal). This is a full-hemispherical transducer (radius / diameter = 0.5), coupled to the patient's head via a circulating cold water bath. The head is held in a stereotactic frame. In the recent Phase III clinical trial concluded in 2016, hand tremor improved following HIFU thalamotomy, with mean tremor severity score 12-months post-procedure dropping by 50% for the treatment group compared to no change in the sham group ($P < 0.001$), and quality of life and disability outcome measures showing equal improvement. After unblinding, the sham group was treated and saw a nearly identical change. At three months approximately 1% of the treatment group experienced worsening tremor, compared to roughly 50% of the sham group. Adverse event rates at 12 months were predominantly numbness (14%) and gait disturbance (9%), or local pain or bruising due to the stereotactic frame (35%) [13]. Investigators concluded that the procedure can reduce tremor in enough cases to warrant clinical adoption.

HIFU thalamotomy is not effective for every patient, for reasons that remain largely unknown. Roughly a third of patients see positive and long-lasting results, a third see no change, and a third see temporary effects (InSightec, private communication), but these rates are similar for RF ablation [54]. In addition, 6% of patients in the HIFU trial seemed to have cranial tissue that conducted sound less efficiently than others, making it difficult to reach ablative temperature. An explanation for these cases was not readily apparent in the imaging data [13]. Future work is being directed at better understanding the nature of acoustic waves and viscoelasticity through an *in vivo* skull and predictive modelling of skull transmission efficiency.

It is unknown why the underlying biology of the disease makes ablative thalamotomy in general an imperfect treatment, but a negative outcome has potential consequences beyond continued symptoms. Aside from risk of an adverse event, a patient who experiences no change in condition after thalamotomy has no additional treatment options. Recently there has been an attempt to salvage such cases, and evidence shows that DBS following a refractory ablation procedure can exhibit a partial controlling effect over the thalamus [55]. For now DBS remains the most effective non-medicinal treatment for ET, but has greater perceived risk, and further data is required to help patients and physicians make informed decision on treatment course.

1.2.3 Uterine Fibroid Ablation

Uterine fibroids (leiomyomas) are noncancerous growths that first appear in women of childbearing age. Estimated worldwide prevalence is between 5% - 10% in the age range of 15-49 years [56]. While they can be mild with few symptoms, common fibroid complications include bleeding abnormalities, such as menorrhagia and dysmenorrhea, increased urinary frequency, and bulk-related symptoms such as acute pressure or pain in the pelvis [57]. Symptomatic fibroids may result in complications during pregnancy or infertility. Large fibroids (diameter 2-3 cm or more) often lead to acute pain, a result of the tumor outgrowing its blood supply. Interventional treatment is recommended in these cases, for which there are numerous options including percutaneous or laparscopic ablation, uterine artery embolization or occlusion (UAE or UAO), or surgical hysterectomy [56]. The goal of non-surgical procedures is to maintain uterine health and fertility while reducing symptoms, with minimal damage to surrounding tissues such as the endometrium and abdominal wall. To that end, the safety of non-invasive MR guided FUS (HIFU) has been established in clinical trials conducted between 2003 and 2013, and shown to reduce procedural complications [14], [58]–[60].

Impact and Limitations: Relative effectiveness of FUS ablation compared to other treatment modalities is still a subject of scrutiny, as prospective trials testing scientific equipoise are ongoing. A large randomized prospective comparison between FUS ablation and UAE has only recently been completed and results are yet to be published (clinicaltrials.gov, NCT00995878) [61]. However retrospective analysis suggests FUS ablation is equally efficacious to both RF and UAE with less associated risks. A large review conducted by the Canadian Agency for Drugs and Technologies in Health (CADTH) of published approaches to uterine leiomyoma management revealed that RF and UAE had similar impact on fibroid-related symptoms, fibroid volume, and quality of life improvement, and UAE had more associated complications [62]. FUS treatments had the lowest rate of complications, but also lower treatment efficacy and increased need for re-treatment compared to RF and UAE. On its face this might suggest FUS is generally less efficacious, but advocates for the procedure point out that the majority of trial data comes from Phase I-II FDA trials, which restricted the allowable ablation volume [57]. Typical fibroid volume reduction at 6 months post HIFU treatment in these studies is 10-20% [57], [59], [63]. However, taking the case of a European trial with 13 women, average volume reduction at 6 months was 45%, comparable to UAE and RF ablation [14], [64], [65]. This suggests less restrictive procedures would result in similar outcomes, though the impact of patient population and selection is unknown.

In initial clinical experience it was shown that the non-perfused volume (NPV) visible on an MR contrast-enhanced T2 image following ablation correlated with improved patient outcomes [59]. Since

MR guided FUS offers an easy, immediate opportunity to image NPV, this possibly offers some benefit over surgical procedures. While additional data is needed, current evidence suggests acoustic ablation of uterine fibroids is medically advantageous. Its major limitations, aside from unverified comparative efficacy, are the long treatment times and risk of skin and abdomen heating discussed earlier.

1.3 Pre-clinical and research stage FUS

Ablation modalities like the ones detailed above are frequently characterized as the main value of focused ultrasound tools, offering a unique combination of non-invasive and precise therapy. However, given the challenges and technical limitations of HIFU procedures, and the often imperfect efficacy of ablative treatments in general (e.g., Abdalla [66]), it reasonable to posit that the long-term utility of FUS lies elsewhere. A wide array of sub-lethal, biomodulatory uses and complementary technologies are on the horizon, for example to deliver drugs past the blood-brain barrier, to selectively elicit neuronal responses, or to activate drug-carriers at specific locations *in vivo*. These offer similarly unique abilities to non-invasively pinpoint a desired biological effect. The tools and methods in this dissertation advance preclinical FUS research endeavors through developments in: 1) tunable control of mild-hyperthermia (a broad technique with multiple applications), 2) accurate targeting of brain cortical regions for neuro-functional studies, and 3) a new phased array and design architecture for cortical targeting. These advancements are detailed in chapters 3-5. In the remainder of this chapter, the scientific background motivating their development and potential applications is put forward.

1.3.1 Background - Cavitation

Acoustic cavitation is the formation and subsequent collapse of small bubbles from gas nuclei in fluids due to high negative pressures. Rarefaction phases of an acoustic wave can cause spontaneous nucleation of dissolved gasses or vaporization of the fluid medium. Cavitation has been observed in HIFU and used to enhance thermal therapy by increasing the rate of temperature gain in the target. Heating acceleration is thought to work through dissipation of the primary acoustic wave via viscoelastic and acoustic effects that create viscous shear flows at bubble-tissue interfaces, and generating energy at higher harmonics of the transmitted frequency which are preferentially absorbed in most tissues [16], [67]. Due to depletion of nucleation sites, movement of cavitation bubbles under radiation force, and inertial collapse at large rarefaction pressure, cavitation is a stochastic, transient phenomenon. The probability of forming an endogenous cavitation bubble depends primarily on the ultrasound peak negative pressure (PNP), but also on the abundance and solubility of gas in the tissue/material being sonicated. 'Stable cavitation' is the term typically assigned to the forced oscillations of bubbles that maintain their integrity under continued acoustic driving. When PNP is large enough, during expansion the gas bubble interior becomes so tenuous it can no longer resist the pressure of the surrounding medium, and it will violently collapse via 'inertial cavitation', producing local fluid jets and shock waves that can damage or disrupt nearby structures [68]. The occurrence of cavitation is a random phenomenon, but is strongly dependent on PNP and gas solubility. It has been repeatedly observed that the transition from 0% to 100% cavitation probability follows a steep sigmoid curve, occurring rapidly as PNP approaches the cavitation threshold.

1.3.2 Mild hyperthermia

Mild-hyperthermia therapy (40-45°C) HIFU is a technique being considered in a number of different treatments such as thermally activated drug delivery, immune-stimulation, and as a chemotherapy adjuvant. Many researchers are currently studying temperature-sensitive drug carriers loaded with chemotherapeutics. Thermally sensitive liposomal carriers loaded with doxorubicin have been used pre-clinically with ultrasound-induced hyperthermia to effectively treat several cancer models [70]–[74]. Studies using mild hyperthermia to activate biological pathways such as apoptosis or immune responses might see confounding effects from mechanically-induced cell damage, which has been shown to directly correlate with inertial cavitation dose [69]**.**

New contributions**:** The violent mechanical forces resulting from bubble collapse can be used to lyse cells and disrupt vasculature. But cavitation may also pose a risk in some treatments that aim to modulate a biological process rather than destroy tissue. For this reason, the ability to perform certain mildly intense procedures, near the cavitation threshold but still below it, may be advantageous. In Chapter 3 a system for doing sub-cavitation mild hyperthermia is presented.

1.3.3 FUS Neuromodulation

Direct Acoustic Effect: Neuromodulation via direct application of low-intensity acoustic waves in the 0.2 – 2 MHz band has recently seen a resurgence of interest. A connection between ultrasound and modulation of neuronal activity has been known for some time, but the mechanisms of action remain an open question [75]. Tyler et al. and others have shown with electrophysiology and fluorescence microscopy that ultrasound can cause activation of Na+ and Ca2+ ion channels and release of neurotransmitter (synaptic exocytosis) that are steps in neuron firing [76]. It has been shown in numerous studies that ultrasound can both stimulate and inhibit motor circuits in mouse and rat brain [11], [77], [78]. Visual saccade motion in a behaving non-human primate was inhibited while sonicating the frontal eye field [79]. A 2014 human study showed increased discrimination between stimuli while sonicating the S1 sensorimotor cortex [80]. A later study compared fMRI and EEG activation during ultrasound sonication of the human V1 visual cortex and photic stimulation [81]. While the mechanism and spatial relationship between the acoustic focus and activated functional networks is not yet understood, it is likely that targeted application of ultrasound can alter the activity of specific neural circuits.

To summarize the current state of knowledge, it is known that FUS can modulate neurons, but the mechanism remains a mystery. Some hypothetical models have been proposed. In one, shear waves at the membrane external boundary induce, either through direct mechanical transduction or an indirect signal cascade, activation of the transmembrane ion channels. A second, possibly related explanation is that exocytosis of neurotransmitter through the synaptic cleft is caused (again by an unknown mechanism) by incident acoustic waves. A third model, though supported by little subsequent data, is that cavitation occurs in the cell membranes of neurons that in turn activate mechanical transduction pathways [82]. Therapeutic benefits of direct, low intensity FUS neuromodulation are being explored in early animal and human studies for treatment of major depression, obsessive compulsive disorder, and post-traumatic disorders of consciousness [12], [83]. So far only isolated cases resulting in symptom relief have been reported, and it remains unclear if the technique is a practical and efficacious treatment option.

Indirect Effect - Activation of Drug Carriers and BBB Opening: An alternative method for modulating neural activity in the brain is through spatially targeted delivery of pharmacological substances past the endothelial layer known as the blood brain barrier (BBB). The BBB is a highly selective semipermeable endothelium that regulates the passage of molecules from blood into the central nervous system. While water and some small molecules such as alcohols and opiates can diffuse into the extra vascular space, a small number of large molecules utilize specialized transporter proteins that have evolved over time to regulate uptake of intrinsic nutrients and hormones [84]. BBB selectivity allows it to play a crucial role in maintaining homeostasis, but also limits the possibilities for pharmacological targets in the brain. Artificially modifying the permeability of the BBB to large extrinsic molecules has been suggested, for example with the use of steroids, but off-target effects limit this approach [85]. More recently it was hypothesized that FUS could be used to achieve controlled extravasation and micro-vasculature hemorrhaging effects [86].

After more than a decade of work mapping parameters and developing MR and PET validation, FUS-induced opening of the BBB can now be done with reliability, and researchers have developed a partial understanding of the mechanisms, safety limits, and efficacy of drug carriers [36], [87]–[89]. A number of drug carriers have been successfully tested, including microbubbles loaded with doxorubicin and iron oxide nanoparticles transfected with anti-tumor immune cells [54], [90], [91]. These same techniques can be applied for delivery of neuromodulatory drugs. Recently Airan et al. showed that nanoparticles loaded with the anesthetic agent propofol could be uncaged at specific targets in rats, leading to reduced EEG signals (an indicator of successful delivery beyond the BBB) [92]. The efficacy of a BBB-opening approach is very promising, but additional studies establishing safety and specific protocols are ongoing.

New contributions: With both direct neuromodulation and mediated BBB-opening, the ability to spatially pinpoint the location of desired effects makes FUS a unique probe for understanding the brain and addressing localized pathologies. While previous work in image-guided transcranial targeting exists, the methods are not sufficient for our purposes. The work presented in chapters 4-5 creates two new tools that enable accurate targeting of FUS as a non-invasive neurological probe. Initial *in vitro* and *in vivo* experiments detailed in the proceeding chapters have validated their performance, and the door is open for future discoveries. In the next chapter, a review of prerequisite technical background is presented.

CHAPTER 2
REVIEW OF TRANSDUCERS AND IMAGE GUIDANCE

Despite its long history, focused ultrasound has only recently begun to mature as a viable clinical tool, largely thanks to development of enabling methods and technologies. Materials and fabrication techniques for making high-power array transducers with customized geometries have helped to facilitate pre-clinical FUS investigations for a variety of diseases and conditions. MR image guidance has led to safe and accurate targeting, and real-time control of acoustic power delivery. This chapter describes transducer materials, design, and image guidance as enabling technologies for FUS, and presents a brief review of concepts and published research studies. The original work presented in Chapters 3-5 draws heavily on the background presented in this chapter. In particular, transmit beam forming from an annular random array is used to broaden the focal zone in mild hyperthermia (Chapter 3); registration-based image guidance and optical tracking are used to improve transcranial targeting accuracy and align motion-encode gradients (Chapter 4); and ultrasound phased-arrays are considered in the development of a new transducer (Chapter 5).

2.1 Transducer Materials

Ultrasound transducers are made of piezoelectric materials designed to oscillate in response to electromechanical stimuli over a specified frequency band. An oscillating electric current applied across the piezo will cause the element to vibrate. When coupled to a medium that supports acoustic waves in its frequency band, some of the transducer’s vibrational energy is transferred to the medium in the form of longitudinal pressure waves used acoustic therapy and imaging. The ratio of acoustic output power to electrical input power is often termed **transducer efficiency** [4]. Transducer efficiency is mainly a concern in HIFU ablation therapy, where transducers must be capable of generating long duration, high power pulses without overheating.

The most common piezo formulation for ultrasonics is lead zirconate titanate (PZT). For many years the primary implementation of PZT transducers were piezoceramics, which are single, continuous bulk crystal masses. Piezoceramics are fabricated via conglomeration of ferroelectric crystallites that undergo chemical reaction when fired in a high-temperature kiln, producing a bulk solid with domains of randomly oriented electric dipoles. A large external electric field (the polling field) is applied to align and freeze the dipoles in the direction of desired longitudinal wave emission [93]. Piezoceramic transducers with air-backing are still quite common in focused ultrasound, but they have over time been replaced due to several disadvantages in acoustic performance. For one, multiple vibration modes occur across the bulk crystal mass, and a portion of the energy is converted to lateral waves along the surface, reducing longitudinal wave output [94]. Additionally, bulk piezoceramics have high acoustic impedance (tens of MRayl), causing pressure waves to be internally reflected. They are also difficult to fabricate into arbitrarily shaped transducer elements [93], [95].

An enabling innovation was 1-3 piezocomposite materials, in which small rods of piezoceramic are bound in a polymer epoxy matrix. Alignment of these rods ensures that the dominant vibrational mode is the thickness mode responsible for longitudinal pressure waves, making acoustic output easier to accurately simulate [95]. Piezocomposites incur greater internal thermal losses than bulk ceramics, but this is compensated by other features. The admixture of rods and epoxy reduces overall acoustic impedance, reducing reflected power and resulting in better output coupling. Their design also permits binding an impedance matching layer to the transducer face that further improves acoustic coupling – not possible with bulk ceramic. Internal mechanical losses increase the bandwidth of the transducer, allowing transmission of broadband pulses. Finally the composite matrix is flexible, lightweight, and can be somewhat arbitrarily shaped, enabling relatively inexpensive fabrication of custom transducer geometries [95]–[97].

2.2 Phased-array Transducer Design

Piezocomposites have become the standard material for focused ultrasound array transducers. Versatile construction has led to a sub-field of acoustic array design optimized for specific applications. This section presents a foundational overview of FUS array design, which are outlined in **Figure 2.1**. In Chapter 5, an original design of a randomized phased-array optimized for non-human primates is presented.

2.2.1 Imaging vs. Therapeutic Arrays

Much of the work on ultrasound 2D array design has come from the volumetric imaging community, where large-aperture 2D arrays are needed for quality image resolution at depth. To achieve 1˚ or better angular resolution, a 60λ aperture is needed, but to avoid large grating lobes element spacing must be less than λ/2, necessitating a prohibitively large number (~10^4) of elements to fill the aperture [98]. Subsequent research into sparse 2D array configurations that minimize grating lobes has led to a variety of fruitful results, such as Vernier arrays that use two different sets of elements for transmit and receive that are spatially periodic and offset, Fermat spirals, and randomized arrays [98], [99]. These studies focus on factors affecting image quality such as side lobe and grating lobe levels, and azimuthal beam symmetry. Generally spirals have lower grating lobe artifacts in image reconstruction, followed by Vernier and randomized, though the differences are small and the results seem to depend on aperture shape and the apodization function used. The ideal design for reducing grating lobes is a dense array with near 100% coverage over the aperture and center-to-center element spacing below λ/2, but the cost is prohibitive with current fabrication techniques.

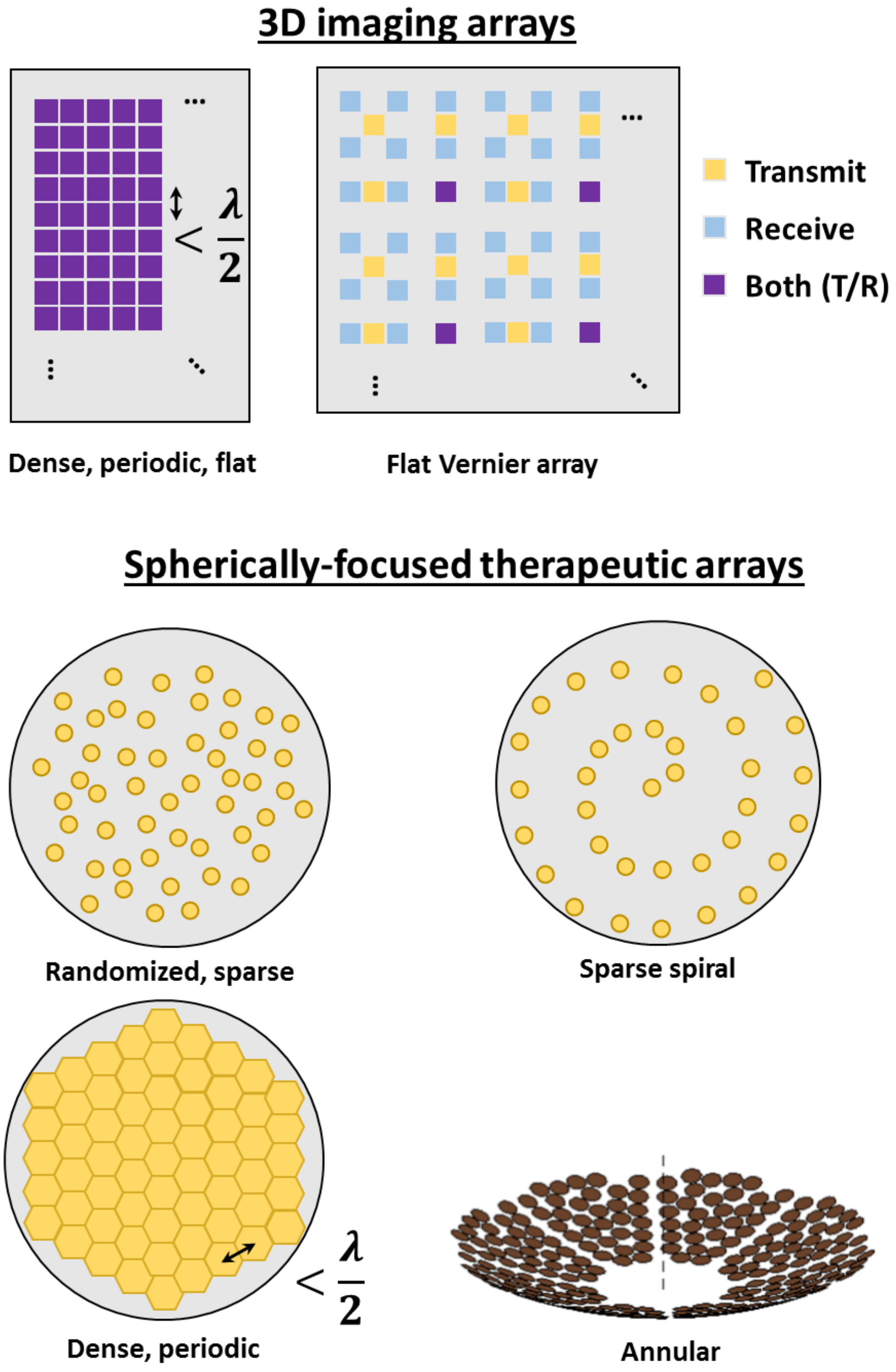

***Figure* 2.1** *Overview of ultrasound array designs used in 3D imaging (top row) and therapy (bottom two rows). Geometry, element distribution, and packing density influence acoustic output and steering capabilities as described in the text. Periodic arrays require dense aperture packing to avoid large grating lobes, though Vernier arrays sparsely packed at two spatial frequencies offer some benefit. For sparse arrays, random and spiral element placement reduce secondary maxima.*

In the case of focused therapeutic arrays, the acoustic design problem is simpler since it is restricted to the one-way (transmit) radiation pattern, rather than the convolution of transmit and receive patterns encountered in acoustic imaging. However, larger transmit power and integration with image-guidance pose unique hardware challenges. Image-guidance is important for accurate spatial targeting and typically requires MR-compatible hardware, integration with co-registered ultrasound probes, registration-based tracking in CT or MRI volumes, or some combination of these methods [100]–[103]. Secondary maxima in the transmit field (often synonymous with grating lobes in focused ultrasound literature) can cause heating in non-targeted regions in hyperthermia. FUS array design has therefore been concerned with maximizing power deposition and steering capabilities while minimizing off-target heating, using acoustic simulations coupled with thermal models [20], [104]–[108].

Imaging arrays utilize a range of short, broadband pulses typically centered in the 3-5 MHz range. Therapeutic arrays use comparatively narrow-band acoustic pulses at lower frequencies (0.2 – 1.2 MHz), thus transducer element thickness and dampening considerations are different. Therapeutic arrays have larger elements that must be driven with greater electric power, between 100 – 3000 W, to reach therapeutic pressure. When driven at maximum power therapeutic devices typically have a de-rated positive pressure in the range 10-100 MPa, and imaging devices in the 0.1 – 0.4 MPa range [109].

2.2.2 Spherically-focused arrays

Geometrically focused ultrasound with a small number of elements for therapeutic purposes dates to the mid-20th century with the experiments of Lynn, Putnam, Fry, and others [23], [24]. Of particular importance is the advent of placing transducer elements on a spherical cap (a.k.a., spherical shell, spherical section) [108]. Irrespective of element configuration, constraining elements to a spherical surface reduces the amplitudes of secondary maxima relative to the focus, but limits off-axis focusing.

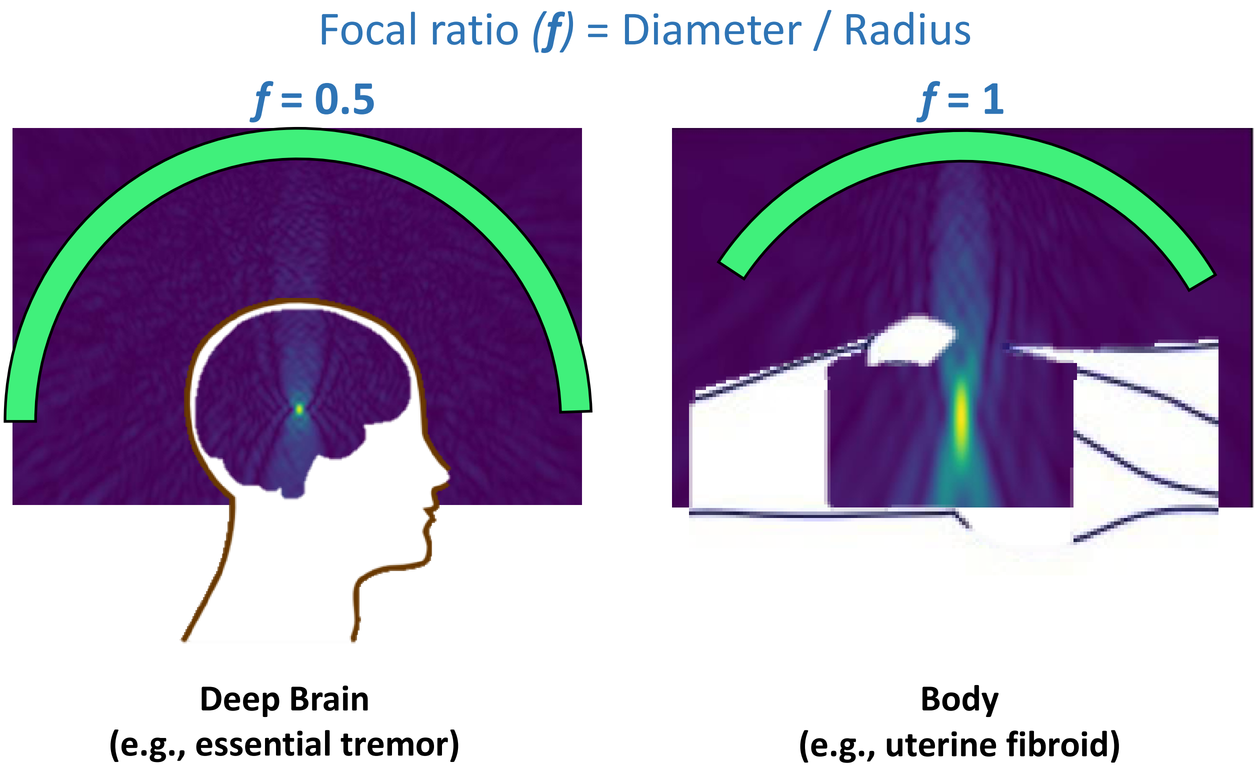

***Figure* 2.2** *Example of application-specific transducer design. In deep brain targeting, an f=0.5 transducer creates a very small focus and roughly conforms to head convexity. Reduced steering capability is mitigated by mechanically positioning the transducer until the spherical focus aligns with the target. Body applications generally use a larger f number that allows more steering, and are less restrictive about focus size.*

Spherically-focused arrays have seen widespread development among FUS research groups and commercial ventures. Requirements such as large acoustic power output and lower frequencies generally necessitate larger element sizes than encountered in imaging. The simultaneous constraints of a large radius of curvature for non-invasive deep tissue sonication, and a focal ratio between 0.5 – 1.0 for effective focal gain without grating lobes lead to large-area transducers (Figure 2.2). In 1999 Daum and Hynynen presented a 256-element spherical cap array for ablation, with a 10 cm radius of curvature and focal ratio 0.83. The surface area was near 100%-covered with equal-area elements, element spacing was nearly periodic and selected to allow safe electronic steering within a 1x1 cm^2 area around the natural focus while maintaining grating lobes < 10% of the focal pressure [106]. In 2004 a similar but larger, 500-element dense spherical array was presented for the purpose of human transcranial ablation of deep-brain targets [29]. It had a similar focal ratio but larger radius of curvature (15 cm) to reduce incident energy density across the skull bone, and a large number of elements to maximize correction of phase aberrations, inferred from trans-cranial simulations [105].

2.2.3 Sparse arrays

Sparse spherical arrays have also received significant attention as a way to achieve large-aperture capabilities with a cost-effective number of elements. In 1996 Goss et *al.* presented an early sparse array for focused ultrasound surgery, examining how array packing may effect performance as the beam is steered off-axis [110], [111]. Since then studies have been conducted for a range of therapeutic array designs considering both element arrangement and size. Gavrilov and Hand used simulations to demonstrate that randomized arrays have lower grating lobes than regularly ordered arrays, and that larger elements decrease array steering performance [112]. A similar result was shown by Ellens *et al.* in a simulation study coupled to Pennes' bio-heat equation, where they demonstrated that grating lobe heating increases for arrays with more sparsity (i.e., less coverage) [20]. Stephens *et al*. presented a comprehensive simulation study comparing spherical and annular arrays having randomized, periodic, and spiral element arrangements similar to those depicted in Figure 2.1 [104]. Among the conclusions are that spherical arrays reduce grating lobes when elements are randomized, instead of using a periodic arrangement. Furthermore, if the same active area is divided among a small number of large elements, vs. a large number of small elements, the transducer has a natural focus that is smaller and closer to the geometric radius, at the cost of off-axis steering performance. Such an array is said to have greater directivity.

Sparse annular arrays have also been designed, typically to hold a second device in the central void space, such as a focused transducer that enables multi-frequency sonications, or an imaging probe for co-registered FUS and ultrasound imaging [30], [100], [113]. These arrays have similar properties to full spherical caps but can have slightly elevated axial and side lobes, increasing risk for off-target heating in thermal therapy [104]. This problem has been recently addressed by using a spiral element configuration rather than a randomized one. Ramaekers et *al.* explored various Fermat-spiral designs and tested one using the golden angle relation (the "sunflower pattern") on a spherical cap [114]. While there was no direct comparison to a randomized array presented, the performance was qualitatively good and may offer advantages in a tighter focus and larger output than a random array owing to its high area coverage. Overall, spherical sparse arrays are good candidates for therapeutic transducer design, but array size, sparsity, element count, and element arrangement offer tradeoffs between cost, grating lobes, focus size, and steering performance that should be considered per application.

As a final note on array design, the general problem of packing equally-sized circular elements on a sphere without overlap – as required for randomized arrays – is well-studied. The key result is that maximal packing density is a function of the number of circles (arbitrarily sized to fit on a unit sphere), with 90.6% being the theoretical limit (an infinite number of elements). Exact packing solutions have been discovered for N=2, 12, and 24 elements, but in practice numerically optimized solutions are used for arbitrary numbers that result in typical densities ~85% [115]. However, these are highly ordered configurations and thus if used as the basis for an array design would be subject to the λ/2 spacing constraint to avoid grating lobes. If array density above 90% is desired, non-circular elements must be used, of which there are several examples [29], [114].

New contributions: In Chapter 5 the design and characterization of a new spherically focused, sparse random array is presented. While the general idea is not new, such an array has not been used for cortical brain targets or designed with the necessary specifications for our application in macaque monkeys. A rational method for selecting array parameters, and the technical tools to execute it, are presented. This breaks from many published research arrays where little to no rationale is explained and seemingly little attempt is made to optimize transducer parameters. Our procedure and open-source tools are guidance for future transducer designs. And while further optimizations are possible, we show that the fabricated transducer meets constraints and has transcranial focusing capability by means of a novel measurement technique in the cortical volume.

2.3 Image Guidance

Development of MR guidance and compatible transducers has helped increase clinical feasibility of FUS therapies. MR guidance enables tissue-selective targeting, feedback via real-time thermometry, and immediate post-treatment assessment with contrast enhanced imaging [25]–[31]. While previous work in image-guided transcranial targeting exists, the methods outlined below are not sufficient for our purposes. In one broad family of approaches that uses purely MR-based targeting, transducer targeting requires an accurate and repeatable positioning system that can be calibrated ahead of time and used reliably at later times. Our current application – navigation of a single element transducer along a small macaque head with 5 degrees-of-freedom – would require a considerably complex, MR compatible positioning system, an interesting endeavor that has recently been successfully implemented after years of work by one group, but which was beyond the scope of the present work [116]. This sections presents a brief review of previous work on MR-guided FUS targeting and calibration.

2.3.1 Selective Targeting with Focused Ultrasound

Accurate targeting is an essential step in FUS experiments. Several techniques exist to predict where a transducer is geometrically focused and navigate it to the desired target in a planning image. One scheme is to use an MR-compatible positioning system that is rigidly attached to the MR table.

Establishing the mapping between motor coordinates and MR coordinates of the focus is the calibration step. Calibration can be done by measuring mild heating in phantoms with MR thermometry, by imaging displacement caused by acoustic radiation force, or by marking the location of an acoustic fountain with an MR-visible marker [10], [51]. Another scheme uses rigidly attached MR tracking coils that can be localized in MR coordinates, and calibrated FUS/tracker coordinates using pilot thermal sonications [117]. Simulation-based time-reversal targeting is also a feasible approach [118], [119]. A fourth (and simpler) method requires visualizing the transducer in a survey image and manually estimating the focus by measuring distances in image space.

The targeting accuracy of these MR-based calibrations has been assessed in several ways. In thermal treatments the spatial centroid of temperature rise is compared to the desired focal target(s). For example, Partanen et al. performed volumetric mild hyperthermia in rabbits using electronically steered trajectories with the Sonalleve, a phased-array with a 5 degree-of-freedom (DOF) in-bore positioning system. They showed that *in vivo* the distance between the aiming centroid and the temperature centroid ranged from 0.6-4.8 mm (average 1.9 mm) and error values increased when trajectories were steered further off-axis [120]. Svedin et al. got similar results in breast-mimicking phantoms with a custom phased-array designed for ablation of breast tumors. Their system used 16 MR-localized tracking coils rigidly attached to the transducer with a 5 DOF in-bore positioning system, and after calibration with pilot heating scans had an average targeting accuracy of 2.1 mm [117]. Alternatively, Illing et al. measured the locations in a T2 image of MR-visible lesions created by thermal ablation, showing a maximum deviation of 2 mm from the target tumor [121].

A different technique was used by Ellens et al. to calibrate mechanical positioning of a single-element FUS transducer. They measured the location of an acoustic fountain created by the focus at several motor positions, and marked these locations within MR coordinates using an MR-visible mechanical transfer plate, providing a registration between motor position and the focus in MR coordinates. Retrospective analysis of blood-brain barrier disruption in rats used contrast-enhanced T2 images to estimate the true focus locations in a coronal plane, which had an average error 1.02 mm comparing to targets with the calibrated positioning system [10].

Recently, Price et al. published an MR-compatible 5-DOF robotic system to navigate a 5 kg transducer for transcranial sonications [116]. A clever accuracy experiment using a felt-tipped pin with the approximate focal length of the transducer was used to put a dot at 18 pre-defined locations on a fixed piece of paper. The trial was repeated many times and the distribution of ink points from the theoretical centroid was used as the accuracy measurement, yielding an average 2D accuracy of 0.58 mm. 3D accuracy values were not reported, but comparing temperature hotspots to target points during phantom sonications suggests 3D error was of a similar scale.

Simulation-based targeting with phased-arrays has also been demonstrated using a time-reversal method [122]. A CT scan provides estimates of scalar acoustic parameters and a simulated source is placed at the desired focus. Transducer elements are localized in the image volume via registration of the transducer frame, and the signal incident on each element due to the simulated source is recorded using a time-resolved acoustic simulator (e.g., k-space or finite-difference time domain). MR thermometry has been used to validate this approach in human heads, yielding average targeting error of 0.95 mm [9]. This technique provides accurate, patient-specific targeting, but requires registration transducer elements with the CT-derived simulation, image-to-image registration if an MR scan is used for targeting, and 4D acoustic simulations.

In summary, a variety of image-based calibration and targeting methods are available for FUS. MR-based calibration and validation experiments have shown average spatial targeting accuracy at or under 2 mm.

2.4 Passive Optical Tracking

2.4.1 Background

Optical tracking is a well-established technique in image-guided surgery that enables projection of tips and surfaces of surgical probes into volumetric imaging data [123]–[125]. In passive optical tracking, surgical tools are rigidly attached to a set of reflective spheres that have a pre-defined geometric configuration. Near-infrared stereoscopic cameras record marker positions as the tool is manipulated, and using the known camera-camera distance and distances between reflective spheres, 3D position and rotational attitude of the tracked body can be deduced. The tip of a tracked surgical probe is localized, or *calibrated*, by fixing it in a divot and pivoting the tool in a circular arc, resulting in an offset vector that is applied in software. Well-designed and calibrated tools can be localized to within 0.1 mm accuracy by most tracking systems, though error between 0.2-0.4 mm is common [126], [127].

Real-time projection of the tool into medical image volumes requires registration between images and tracked physical space. A common method for registration is point-based rigid registration, in which fiducial points are visible in the MR or CT volume, and localized in physical space by placing a calibrated pointer tip on each fiducial and measuring its position with the tracking system. An affine transform between the two coordinate systems is then computed, and is often termed the *physical-to-image* registration.

Registration-based tracking incurs error from compounding uncertainties in fiducial localization, physical non-rigidity or movement of the subject, and non-linear distortions in the target image volume [128]–[130]. The error of primary concern is the *target registration error* (TRE), which is the difference between the projected location of a tracked point in image space and its actual location in the physical space of the patient. Fitzpatrick and others have conclusively shown with theory and empirical data that TRE is primarily dependent on fiducial localization error (FLE) and the spatial configuration of fiducials, and is nearly independent of fiducial registration error (FRE) [128], [131], [132]. Large FRE likely results in large TRE, but below some FRE threshold (dependent on specific configuration), TRE becomes decoupled from FRE. Under the assumption of normally distributed FLE, TRE will be distributed such that, in any set of three orthogonal axes, its vector components are zero-mean and normally distributed, and its RMS magnitude is chi-square distributed [133].

These theoretical predictions have been validated in multiple studies. Labadie et al. evaluated several commercial guidance systems in a uniform manner, using common tracked surgical tools and skin-affixed fiducial markers, and showed average TREs between 1.3 – 2.8 mm [134]. Another study using fiducial imaging phantoms and several commercial tracking systems showed average TREs between 1.6 – 3.9 mm [131].

2.4.2 Optically Tracked Focused Ultrasound

Passive optical tracking was recently implemented to guide placement of single-element transducers outside a magnet for targeted neuromodulation [103], [135]. Kim et al. developed both an MR-independent and an MR-based calibration for tracking a spherically focused transducer [103]. For MR-independent calibration they attached a tracked body to a copper rod, length equal the transducer's radius of curvature (ROC), and performed a pivot test to determine the approximate offset of the focal point. The tracker was then mounted to the back of the transducer so the offset vector could be applied to predict the focus. MR-based calibration was performed with the transducer aimed into an acryl phantom, MR-visible fiducial markers placed around the setup. Fiducial positions in physical space were measured with optical tracking system, and in the magnet structural scans were acquired to establish MR-to-physical registration, followed by heat-inducing sonications. Single-slice, temperature sensitive MR scans acquired alternating orthogonal planes until the hotspot was maximized at the slice intersection, providing a "ground truth" position of the focus. The experiment was repeated three times.

The distance between MR hotspot and predicted focus based on mechanical calibration was 4.4 +/- 0.9 mm (N=3), and the three predicted focal points appeared offset in a biased way (not zero-mean). Cross-comparison of the trials was used to derive an offset vector between prediction and ground-truth, reducing reported accuracy to 1.9 +/- 0.8 mm, though statistical significance and validation of this offset with independent tracking data were not reported.

New contributions: Chapter 4 describes innovation and improvement on the above method for optically-tracked system for FUS. The previous method was not robustly validated and used a statistically unsupported bias correction that was examined in further tests. Moreover, it assumes a focal length equal to the radius reported by the manufacturer. We know from experience with coupling media and cones that the geometric focal point and actual pressure maximum can differ by several millimeters. Therefore, we developed a novel, MR-independent method for calibration of the tracked transducer using an optically-tracked hydrophone and transducer, and projection of the free-field beam for image-based targeting in 3D Slicer. Accuracy (TRE) of the method was assessed with multi-slice MR thermometry in phantoms and shown to be in the range of conventional optically-guided surgeries. The calibrated system was used in subsequent *in vivo* sonications with MR ARFI in a rhesus macaque monkey.

CHAPTER 3
REDUCTION OF CAVITATION IN MULTI-FOCAL MILD HYPERTHERMIA

3.1 Introduction

Mechanical damage and loss of cell viability associated with HIFU-induced acoustic cavitation may pose a risk or may hinder the success of mild-hyperthermia treatments. This chapter presents a method that achieves mild heating and reduces cavitation by using a multi-focused HIFU beam.

Phased-array transducers are designed to enable specialized array encoding (apodization) in which individual transducer elements are independently driven. For narrow-band acoustic transmissions, apodization equates to setting an amplitude and phase delay for each element in the array. Phased-arrays allow generation of a pattern of multiple simultaneous foci to distribute acoustic energy over a larger volume than with a single focus. Initial work with the Sonalleve MR+HIFU system suggested that mild hyperthermia applications might benefit from a multi-focal distribution because of the lower peak pressures experienced at each focal point. Lower pressure results in decreased occurrences of acoustic cavitation that can be detrimental in some therapeutic cases. This chapter presents implementation of multifocal sonications with the Sonalleve and measurement of cavitation using passive acoustic mapping.

3.2 Summary

Methods: Continuous wave sonications were performed with the Sonalleve V2 transducer in gel phantoms and pork at 5, 10, 20, 40, 60, 80 acoustic watts for 30 seconds. Cavitation activity was measured with two ultrasound (US) imaging probes, both by computing the raw channel variance and using passive acoustic mapping (PAM). Temperature rise was measured with MR thermometry at 3T. Cavitation and heating were compared for single- and multi-focal sonication geometries. Multi-focal sonications used four points equally spaced on a ring of either 4 mm or 8 mm diameter. Single-focus sonications were not steered.

Results: Multi-focal sonication generated distinct foci that were visible in MRI thermal maps in both phantoms and pork, and visible in PAM images in phantoms only. Cavitation activity (measured by channel variance) and mean PAM image value were highly correlated (r>0.9). In phantoms, cavitation exponentially decreased over the 30-second sonication, consistent with depletion of cavitation nuclei. In pork, sporadic spikes signaling cavitation were observed with single focusing only. In both materials, the widest beam reduced average and peak cavitation level by a factor of two or more at each power tested when compared to a single focus. The widest beam reduced peak temperature by at least 10˚C at powers above 5W, and created heating that was more spatially diffuse than single focus, resulting in more voxels in the mild heating (3-8˚C) range.

3.3 Background: Cavitation in Thermal HIFU

Much prior work examining cavitation and ablation therapy has sought to enhance treatment through cavitation [67], [86], [136]. Several groups have implemented feedback control to sustain cavitation activity and further enhance temperature rise or induce mechanical damage [88], [137], [138]. However, cavitation is ideally avoided in mild-hyperthermia therapies (40-45°C) where the goal is for targeted cells to maintain viability for subsequent treatment (e.g., chemotherapy), or to evoke specific biological process such as apoptosis or anti-inflammation signaling [44], [120], [139]. Mechanical damage or thermal necrosis--both of which may result from spontaneous cavitation--would likely interfere with these processes. Additionally, a number of heat-sensitive drugs and drug-delivery vehicles that can be activated *in situ* with targeted heating are under investigation [70]–[73], [140]. These require sustaining mild temperature rise within a tissue volume for several minutes, typically at low acoustic pressures that limit risk of mechanical effects [141]. Researchers have demonstrated increased metastatic burden in a mouse model of melanoma using high power acoustic pulses (1MHz, PNP>8 MPa, 50 msec duration) in conjunction with microbubbles that act as cavitation nuclei [142]. Molecular dynamic simulations have suggested that protein structures can be significantly modified by acoustic shockwaves and nanometer scale jets, and cavitation-produced free radicals may also alter the efficacy and toxicity of therapeutic molecules [143], [144]. The multi-focal methods used in our study can deliver mild hyperthermia in the absence of cavitation and may be preferable in instances where mechanical cavitation could hinder dose delivery. These bioeffects likely depend on cavitation dosage, since others have achieved cavitation-aided drug delivery without negative bioeffects using similar acoustic pulses in the absence of microbubbles [145].

A system capable of applying mild-hyperthermia with limited risk of cavitation is therefore desirable. We investigated whether this can be achieved by broadening the therapeutic beam by use of multiple foci. In 2013 Partanen *et al*. presented work with a clinical MR+HIFU system showing a multi-focal, volumetric mild hyperthermia treatment for several minutes [17]. They compared focus switching via electronic steering with sonicating all points simultaneously and demonstrated that multi-focal sonication reduces peak negative pressure and peak temperature, while still maintaining sufficient focal energy deposition for therapeutic temperatures.

This chapter compares the effect of single- and multi-focal continuous wave (CW) HIFU on heating while quantifying cavitation activity. Three focusing scenarios at six acoustic powers were examined in

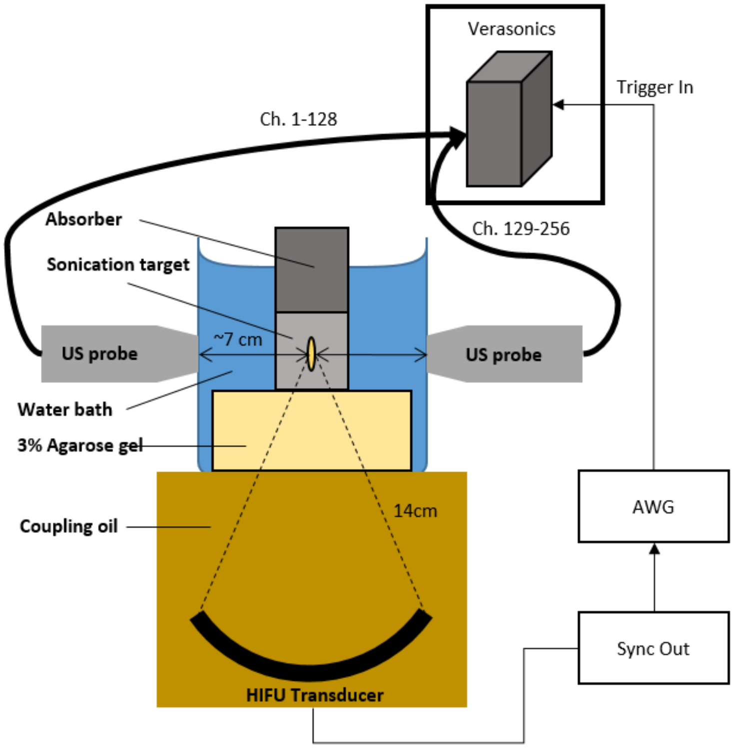

Figure 3.1 Experiment setup to monitor HIFU-induced cavitation

tissue-mimicking phantoms, and two scenarios were examined in pork. During sonications, cavitation activity was monitored with US imaging probes outside the MRI environment, and temperature was measured using MR thermometry. Broad beams produced from multiple foci reduced cavitation and spread heating over a wide spatial region suitable for mild hyperthermia applications.

3.4 Methods

3.4.1 Multi-focal sonication

We evaluated single and multi-focal sonication with the Philips Sonalleve MR+HIFU system. Sonications were performed with the Sonalleve V2 R3.2 system, a 256-element randomized sparse array transducer (element diameter 6.6mm), spherically focused with a focal length of 14cm and diameter approximately 14cm at the opening face (Philips Medical Systems, Vantaa, Finland). Multi-focal beam patterns were generated in a manner similar to Partanen et al., which uses the method of Ebbini and Cain to compute array encodings [17], [146]. The Partanen study used an 8-mm ring pattern with 16 equally spaced foci in the transducer focal plane and sonicated for several minutes under temperature feedback control, based on the 8-mm treatment cell trajectory used by the Sonalleve in volumetric HIFU treatments [147]. Our multi-focal beam geometries were an 8-mm ring pattern and a 4-mm ring pattern, but in our case only four focal points were used, without feedback control. This pattern achieved more focused energy deposition than Partanen et al., resulting in heating within 30 seconds at low powers. The experimental setup is shown in **Figure 3.1**, and multi-focal beams are shown in **Figure 3.2**.

3.4.2 Passive Acoustic Mapping (PAM)

To measure the spatial distribution of cavitation activity we used a common ultrasonic imaging technique. PAM closely resembles delay-and-sum image reconstruction, except that it uses one-way, receive-only delays. The equation used for image formation is given below.

$$\mathrm{Image}(\mathbf{x}) \propto \int \left[\sum_{i=1}^{N} 4\,\pi |\mathbf{x} - \mathbf{u}_i|\, v_i \left(t + \frac{|\mathbf{x} - \mathbf{u}_i|}{c} \right) \right]^2 dt \quad (1)$$

Here, **x** is the reconstructed pixel location, $\mathbf{u}_i$ is the position and v_i the raw channel data of element *i.* The time argument in v_i represents the one-way delay from a coherent source at pixel **x** to element *i,* and the distance multiplier compensates for solid-angle spreading of a spherical wave. Time integration averages multiple image acquisitions together. This form of the reconstruction was referred to as “Time-Exposure Acoustics” (TEA-PAM) in Coviello et al. to delineate it from more advanced beamforming, but for simplicity we refer to it simply as PAM [148]. The equation for image pixel **x** is expressed as a proportionality because, although theoretically feasible, quantitative imaging would require a calibrated probe, accounting for the image point-spread function from measured data, and additional system transfer functions (digital filters, probe frequency response, etc.).

An open-top water tank with an agarose standoff held the sonication target such that its center was roughly at the HIFU geometric focus (14cm). Acoustic windows were cut into opposite sides of the tank, covered and sealed with a thin plastic membrane to allow coupling of the US probes (**Figure 3.1**). By using an imaging array PAM provided a broader spatial response over single-element cavitation monitoring due to the limited focal response of single-element transducers. We used two probes to ensure that “tail artifacts” inherent in PAM images that extend distally from the transducer face would not obscure cavitation sources in multi-focal sonications. Cavitation signals were acquired during continuous HIFU exposure using two ATL L7-4 128-channel ultrasound imaging probes connected to a 256-channel Verasonics imaging system. The Sonalleve HIFU generator provides a Sync Out for external triggering at the start of sonication, and this was used to trigger start of PAM acquisition. Due to the large amount of data generated by collecting cavitation images at a high frame rate, we limited HIFU sonications to 30 seconds, shorter than a typical hyperthermia treatment. After the initial trigger, acquisitions were made every 50 ms (20 per second) from both probes simultaneously. 2048 digital samples were recorded per acquisition, at a sampling rate of 20.8 MHz, resulting in 98.46 microseconds (2048 / 20.8) of data per each acquisition and an image reconstruction depth greater than 9cm. Thus about 2 ms (20 * .09846 ms) of receive data was recorded for every second of CW HIFU, a receive duty factor of 0.2%. 600 frames were recorded in total, spanning a total of 30 seconds.

3.4.3 Probe alignment and registration

The US imaging plane was approximately aligned to the HIFU focal plane in the following way. With the agarose standoff and a small amount of water, a low-power (1W) continuous sonication was started, and the water level slowly increased. As the water surface height approached the focal plane, a slight fountain formed. Water was added and removed during this sonication via a siphon tube until the fountain intensity—indicated by the height of ejected water—was roughly maximized. This qualitative procedure was sufficient since the full-width half-max (FWHM) of the focus in the axial direction is long (~1cm). The two imaging probes were then attached to optical table rails and slid towards the coupling window. The center line of each probe face was aligned with the tank water level, coupled, and secured against further motion. The remainder of the tank was then filled with water. On completion of this procedure, the HIFU focal plane was approximately centered within the elevational focus of the L7-4 transducer (FWHM of 6 mm at the optimal focusing depth).

Image registration was required to construct PAM images from received echoes on both probes. To compute the registration, several fiducial measurements were conducted. First, the two probes were operated in pulse-echo mode while a point source (steel rod with diameter of 2 mm) was positioned at several locations in the image field. Second, the therapeutic transducer at high power (60W acoustic) briefly sonicated (5 seconds) an agarose phantom with the beam steered to several positions, which served as cavitation point sources in the resultant PAM images. These calibration methods provided two consistent sets of common fiducial points in the image space of probes 1 and 2. Probe 2 was then registered to the probe 1 space using a rigid transform. Jointly reconstructed images are reported relative to probe 1. Registration yielded a probe separation of roughly 13.6 cm, which agreed with the measured tank width.

3.4.4 MR Temperature Mapping

Thermal maps were generated with a 3T Philips Achieva using the proton-resonance frequency shift method (PRFS), where the phase change between two acquisitions is proportional to temperature change [149]. The sequence was a multi-slice gradient echo planar imaging sequence (FEEPI with TE=16ms, TR=24ms, EPI factor 11, voxel size 1.8x1.8 mm and 3mm slice thickness**,** with field-of-view (FOV) of 222 x 170 x 18 mm). Coronal slices were used to verify multi-focal heating, and sagittal slices aligned with the HIFU focus in the center slice were used for thermal measurements. A 3D stack of images was acquired with a dynamic scan time of approximately 1.3 seconds per volume. Temperature distributions were examined in a region-of-interest (ROI) with approximate dimensions of 16x12x12 mm, with the long dimension along the HIFU direction. ROI size was chosen to fully encapsulate the focal zone and allow a small margin to account for heat diffusion. Phase-drift was not corrected due to the short duration of scans (40 seconds). For visualization, thermal maps are overlaid on grayscale magnitude images.

3.4.5 Sample Preparation

Tissue-mimicking gel phantom was prepared by mixing agar powder (Now Foods, Bloomington, IL) and 400 grit silicon carbide powder (Beta Diamond Products, Anaheim, CA) into de-gassed water. Agar concentration was 3% and graphite concentration was 1% (weight [g] /volume percent [ml]). The liquid solution was heated to 90˚C then allowed to cool for several minutes while stirring, then poured into a 5-cm diameter glass cylindrical phantom mold placed in a cool water bath to decrease cooling time. After hardening, the cylinder gel was removed and cut lengthwise into sections approximately 3.5cm long. This allowed creation of a large batch of phantoms at once. Pork chops were purchased from a local grocery and samples prepared by removing fatty tissue pieces and cutting into cubic sections approximately 3 cm thick.

3.4.6 Phantom and pork sonications

A total of 72 phantom sonications and 24 pork sonications were performed. Half of the sonications were performed with US imaging to assess cavitation and half within the MRI system to measure temperature. Phantoms or tissue samples were always replaced between sonications to ensure that heating or depletion of cavitation nuclei did not affect subsequent measurements. Cavitation imaging trials were first performed with the transducer bed outside of the magnet room. Using the MatHIFU interface, applied power was 5, 10, 20, 40, 60, or 80 acoustic watts for single focus and two multi-focal patterns (diameters of 4 and 8 mm). Temperature mapping experiments were done within the magnet: the US imaging probes were removed, the bed was rolled into the magnet, and the same protocol repeated. Cavitation and MR imaging of phantoms was repeated once, with fresh phantoms. Pork sonications followed the same procedure comparing single and 8-mm multi-focal geometry.

Lesion formation was observed after single-focus sonications in the pork samples at 40W and above. No lesions were observed in the multi-focal case. Since solid lesions accelerate heating, and likely change the probability of cavitation, 60W and 80W single-focus sonications of pork were not repeated in the MR scanner. PAM image data were collected for these cases.

3.4.7 Data Analysis

US and MR data were analyzed offline using custom Python scripts. Experimental data was grouped according to sonication power level, focus geometry, and target material. PAM images were reconstructed using the beamformer in equation (1) with pixel size of 0.2x0.2mm.

To measure cavitation source strength we computed the time-domain signal variance and broadband (non-harmonic) spectral noise observed in each acquisition. Variance was computed per channel using the raw channel data from each probe. The summed variance over all 256 channels was then used as a measure for cavitation (referred to as “Ch. Variance” in figure labels). Broadband noise was computed by first taking the Fast Fourier Transform of each channel. Harmonics and ultra-

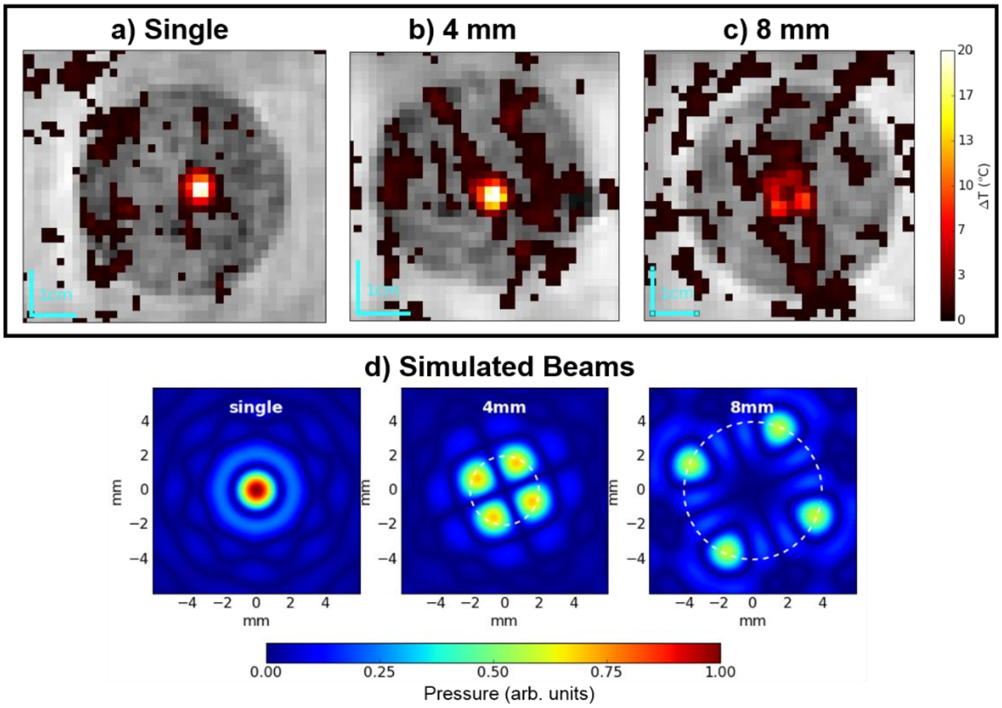

Figure 3.2 *Depiction of the three HIFU beam geometries used in this study. (a)-(c) Example coronal MR images showing heat deposition from single focusing and the two multi-focus patterns. (a) Single focus beam. (b) Four points placed on an imaginary ring of diameter 4 mm. Individual foci were not resolvable with the given scan parameters, and thus appears similar to a single-focus in the image. (c) The same four points on a ring of diameter 8mm. (d) Rayleigh-Sommerfeld simulated pressure field, normalized such that the single focus peak is unity, and the 4 and 8 mm foci are 0.7 and 0.6 respectively.*

harmonics were removed with a notch filter (-3dB passband width of 0.4 MHz) centered at multiples of 1, 1.5, 2, 2.5, etc. of the 1.2 MHz HIFU frequency. Broadband noise was calculated as the sum over the filtered spectrum. Both broadband noise and total variance were compared to a PAM-derived measure of cavitation, which we expressed as the mean pixel value of a reconstructed PAM image (i.e., the average of a reconstructed image).

3.5 Results

3.5.1 Multi-focal sonications generated distinct foci

The single focus and two multi-focal sonications generated expected heating patterns after a 10-second sonication at 40W in phantoms (**Figure 3.2**). Simulations suggest the multi-focal sonications are roughly

70% (4-mm) and 60% (8-mm) of the single focus peak negative pressure (PNP), and these were verified at low power (1W) with a needle hydrophone. During the 4-mm sonication, four foci were not

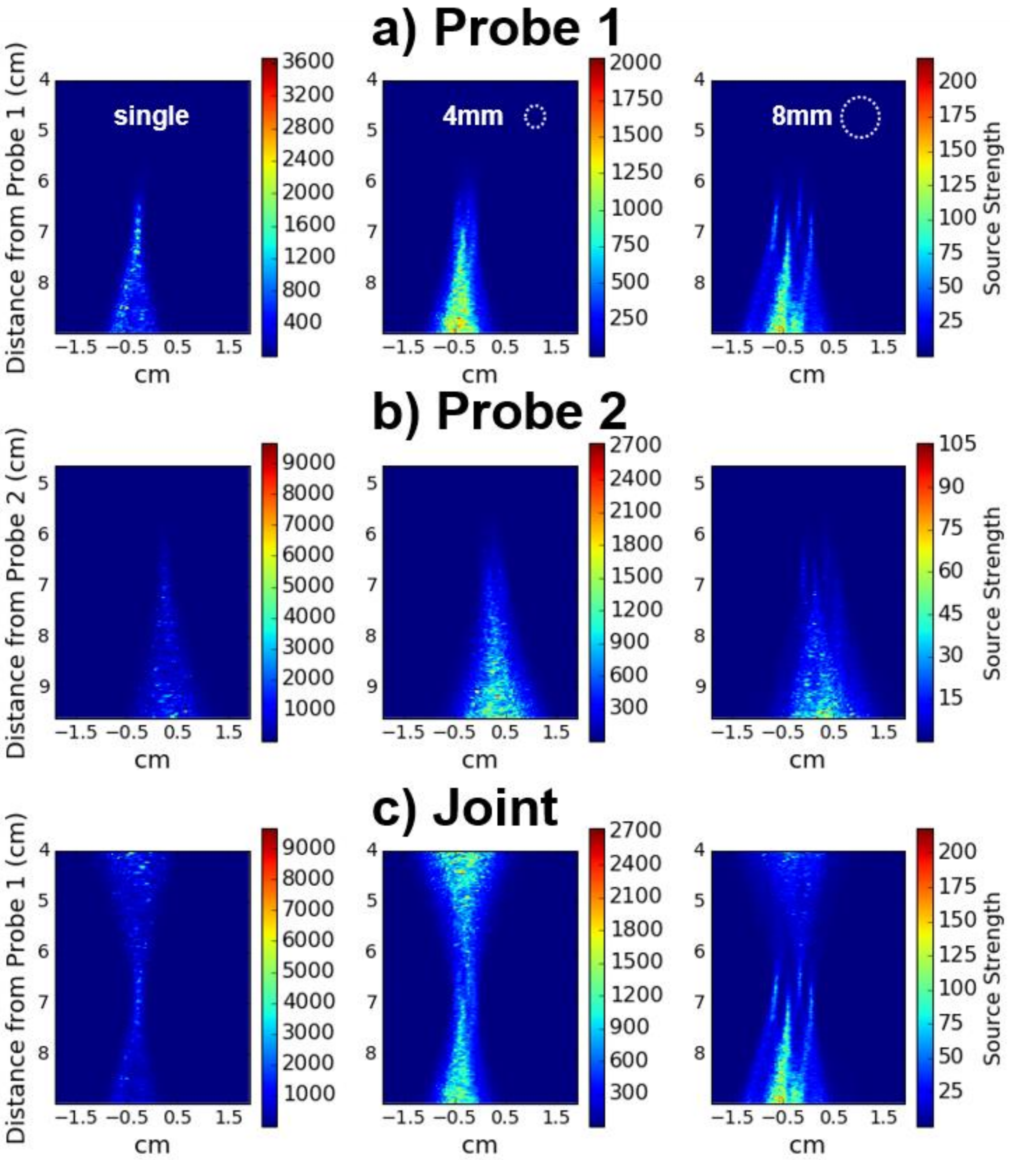

Figure 3.3 *PAM images for a set of 60W sonications in phantoms, time-integrated over all 30 seconds of HIFU+PAM acquisition. The columns are as follows--Left: single-focus. Middle: 4-mm multi-focus. Right: 8-mm multi-focus. Rows (a) and (b) show Probe 1 and Probe 2 reconstructed according to equation (1). In row (c) Probe 2 was registered to Probe 1 and both probes reconstructed in the co-registered pixel domain. In PAM images tail artifacts can be easily recognized. The ratio of apparent tail strength to magnitude of the foci is larger with multi-focus. It can also be seen that, in each multi-focus case, the focal point furthest from the probe has a larger tail effect. This is perhaps due to reverberation and backscattering of waves from cavitation at the closer foci.*

individually resolved most likely due to the scan having spatial resolution comparable to the distance between adjacent foci, although the hot spot produced was broader than a single focus. The 8-mm sonication produced individual foci that could be visualized with MR thermometry.

3.5.2 PAM imaged simultaneous cavitation nuclei

The PAM technique was capable of resolving foci in single and multi-focal sonications in the phantom. Individual foci can be clearly resolved in the 8-mm multi-focal case but are less distinct in the 4-mm case (**Figure 3.3**). Tail artifacts appeared in every PAM image, but when comparing the near-field of one probe to the far-field of the other, no additional cavitation sources were present other than the HIFU foci. In multi-focal sonications the farthest focal point from the perspective of each probe had the

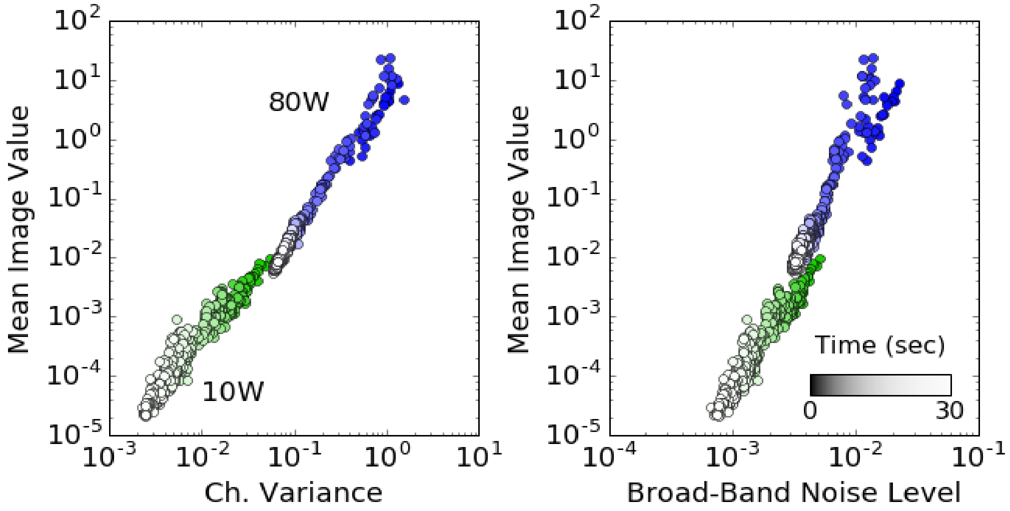

Figure 3.4 *Example of PAM image magnitude (mean of pixel values) vs. commonly reported measures of cavitation activity (arbitrary units) for a 10W and 80W, 30-second phantom sonication. The tight correlation suggests PAM image magnitude is equivalent to variance and broadband noise as a proxy for cavitation activity. Each point is computed from a single ultrasound acquisition, and the full set of 600 acquisitions is shown for 10W and 80W. Channel variance is the sum of raw channel variances (proportional to receive volts-squared). Broad-band noise level is the total amplitude of the frequency spectrum (proportional to volts), once harmonic and ultra-harmonics have been filtered out. In both plots the x-axis values were computed per channel and then summed. The color saturation gradient represents sonication time, as is shown in the color bar on the right. The most saturated color is at time 0, and the least saturated is at 30 seconds. Quantities remained correlated even after bubble depletion in the first several seconds.*

brightest tail artifact in all cases.

3.5.3 PAM correlated with standard cavitation metrics

Passive US monitoring produced results consistent with expectation. First, we observed a nearly one-to-one relationship between mean PAM value and channel variance, and between PAM value and broadband noise. The mean PAM image magnitude correlated strongly to the time series variance and

(a) Phantom

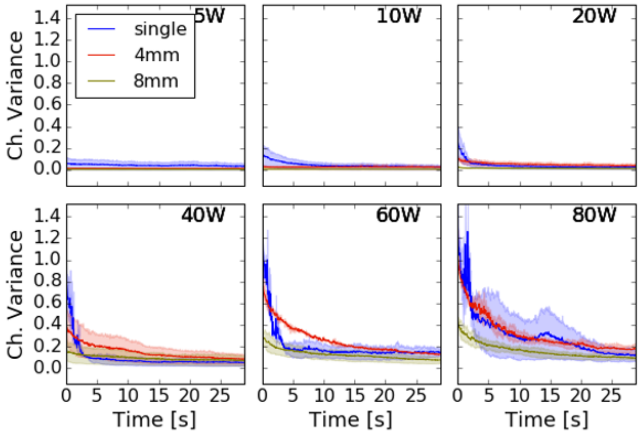

(b) Pork

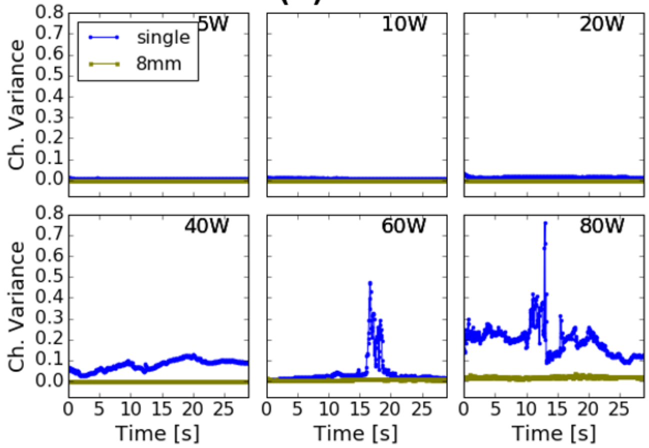

Figure 3.5 *Time history of total channel variance as a measure of cavitation activity for 30 seconds of HIFU. Each point represents one acquisition and is the sum of the 256 raw channel variances. (a) Averaged value from phantom trials, as well as the min and max values observed. The observed exponential decay is consistent with cavitation depletion and transient, noisy signals are indicative of cavitation bubble collapse. (b) Result of pork trials. In pork, a thermal lesion was observed after the 40W single focus sonication.*

to the square of the broadband noise level (Pearson’s r > 0.9 in all cases). **Figure 3.4** illustrates this correlation for 10W and 80W single-focus sonications in phantoms.

3.5.4 Multi-focal sonication reduced cavitation

At all powers examined, cavitation activity (as measured by channel variance) had an initial high amplitude onset followed by an exponential decay towards zero as sonication progressed. In phantoms, a majority of cavitation occurred within the first 4 seconds of sonication with the longest decay times occurring in multi-focal cases (**Figure 3.5**). Cavitation in pork was less consistent, with the 40W case giving a consistent low amplitude channel variance while the 60W and 80W cases showed high amplitude peaks with fast decay multiple seconds into the sonication. Within the first second, the mean

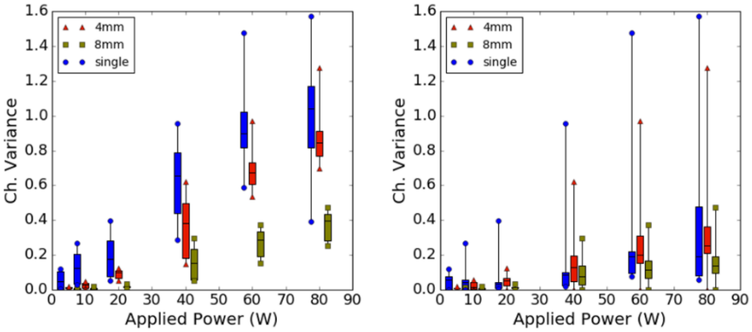
(a) Phantom, 1s

(b) Phantom, 30s

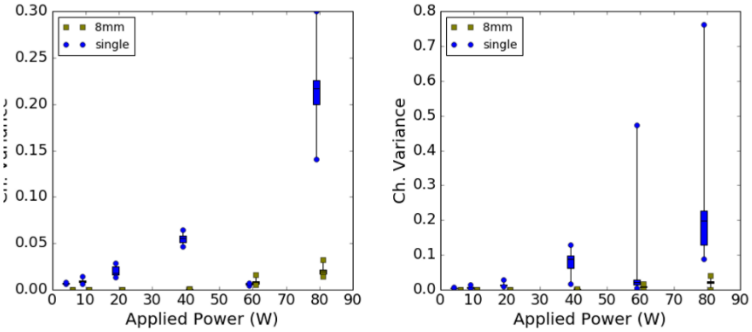
(c) Pork, 1s

(d) Pork, 30s

__Figure 3.6__ Distribution of measured cavitation activity (summed channel variance), vs. total power applied to the array for one set of sonications at 5, 10, 20, 40, 60, 80W. Box locations are offset along the x-axis to allow side-by-side comparison. Each box represents the distribution (min-max, and 25, 50, 75th percentiles) of cavitation activity. (a) and (c), distribution within the first second. (b) and (d), distribution over the full 30-seconds.

channel variance during single focus sonication was higher than multi-focal in both the phantom and pork preparations (**Figure 3.6a,c**). Though cavitation activity was always initially highest using the single-focus beam, the 4-mm multi-focal beam had similar average variance to the single focus when measuring cavitation over the entire 30 s sonication, most likely due to a rapid depletion of cavitation bubbles at the single focus. We observed reduced cavitation in the 8-mm case at all powers.

3.5.5 Multi-focal sonications reduce peak heat

In all cases examined, single-focusing resulted in higher peak temperature and more focused heating at a given input power. At 20W and 40W the single focus heating was 21˚C and 24 ˚C greater than the 8-mm multi-focal case, respectively, and the temperature distribution across the ROI was more uniform in

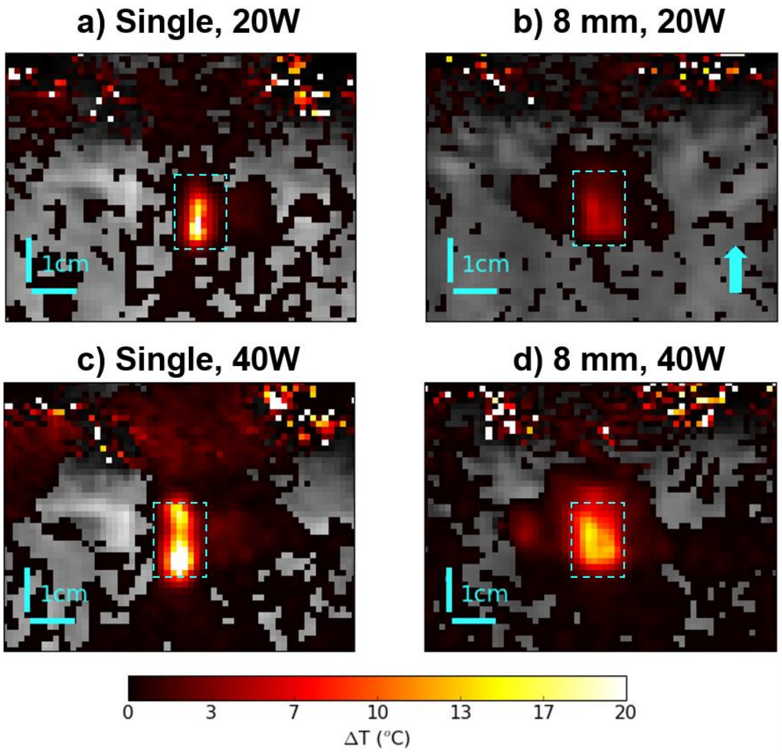

Figure 3.7 *Zoomed view of the center slice (sagittal) of MR mapping volumes for 20W and 40W sonications in pork after 30 seconds of HIFU. The arrow indicates direction of HIFU propagation. The dotted line represents ROI cross-section. Note: after sonicating at 40W a surface lesion was observed at the pork interface (bottom of the ROI in (c)). Note: the color scale has been windowed to 0-20°C to emphasize contrast in multi-focal sonications.*

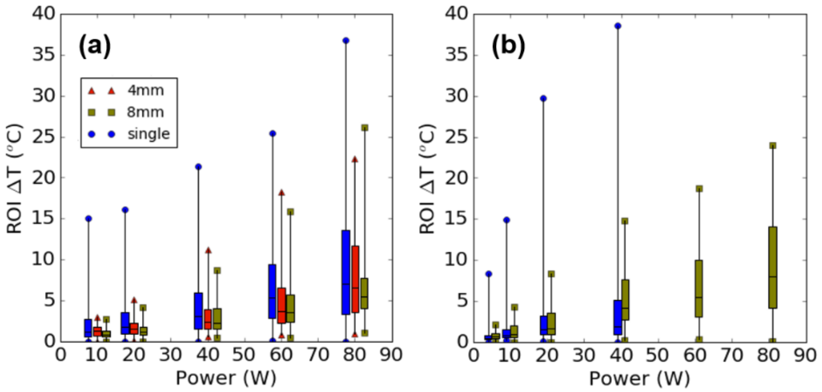

Figure 3.8 Distribution of voxel temperatures in the focus ROI in (a) phantom, and (b) pork after a 30 second sonication. Min/max and percentiles levels corresponding to 25, 50, 75% of voxels are plotted. Multi-focusing has lower peak temperature more voxels in the mild hyperthermia range. 5W sonication data is omitted from (a) to prevent crowding. 60W and 80W single-focus sonications were not repeated in the scanner with pork due to formation of thermal lesions at 40W.

the multi-focal case (**Figure 3.7**). **Figure 3.8** displays the distributions as a box-and-whisker plot for each focusing case, at 10, 20, 40, 60 and 80W acoustic power. A larger max-min spread of temperature values was observed with single-focused beams, while multi-focusing resulted in narrower voxel distributions with more voxels clustered in the mild hyperthermia range. For example, at 40W in pork, the peak temperature rise was +39˚C in single-focus and +15˚C in multi-focal, but the median was +2˚C vs +4.5˚C, respectively. Broadening the beam made heating more diffuse and reduced total cavitation (**Figure 3.8)**.

3.6 Discussion

3.6.1 Summary of results

In this study, we have demonstrated that by broadening the therapeutic HIFU beam with multiple foci, a large reduction in cavitation activity can be achieved while still maintaining temperature increases in the range of mild hyperthermia. Similar multi-focal approaches to reduce peak pressure have been previously demonstrated to be effective for mild hyperthermia, and our study is the first to measure

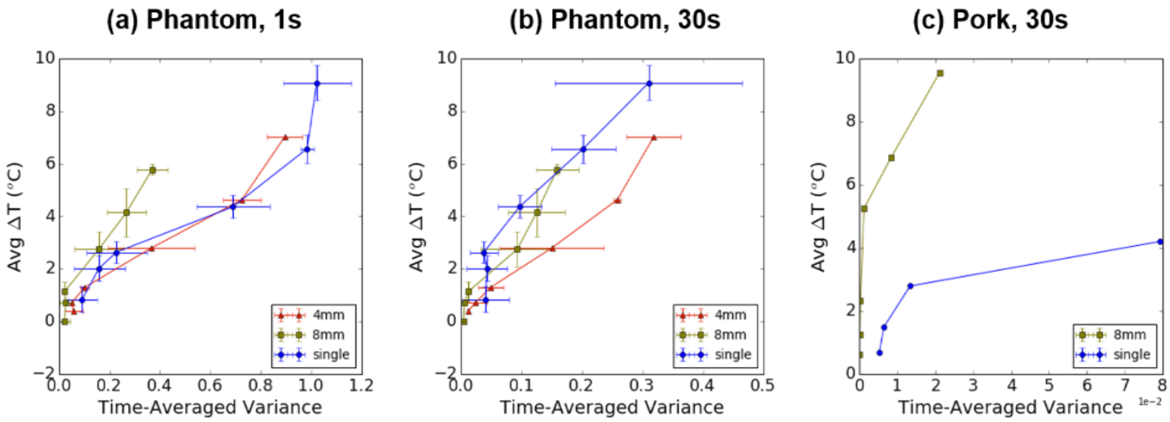

Figure 3.9 *Final temperature rise after 30 seconds of HIFU (averaged over the ROI) vs. cavitation activity. Points correspond to 5, 10, 20, 40, 60, and 80 acoustic watts (in pork, single-focus MR data wasn't collected above 40W due to lesion formation). (a) Averaging over 1-second in phantoms (prior to bubble depletion) shows less cavitation at a given input power in both 4mm and 8mm cases. (b) Averaging over the full 30 second sonication, 8mm multi-focusing achieves an average rise in the mild heating range (+3-8˚C) above 20W with generally less cavitation at each input power level. At 40W total cavitation activity is comparable between the two, but this is likely due to initial rapid depletion of bubbles in single focus (see Discussion). (c) Negligible cavitation activity was observed with multi-focusing in pork. The large jump in channel variance at 40W, pork, single-focus may be a result of lesion formation, cavitation, or both.*

cavitation activity during multi-focal heating [17]. We used diagnostic imaging arrays to receive cavitation signals over the broad multi-focal area, and implemented PAM to image the spatial location of cavitation foci in phantoms. Standard metrics of cavitation (broadband noise level and channel variance) linearly correlated to the mean PAM image values, and multi-focal sonications generated less cavitation activity and more diffuse heating. These characteristics make the proposed sonication method ideal for therapeutic applications where heating in the absence of cavitation is desired.

3.6.2 PAM imaging of multi-focal cavitation

We spatially mapped simultaneous cavitation foci during multi-focal sonication using PAM to generate images with cavitation foci geometrically arranged in the expected focal pattern. The US probes demonstrated the probe tail artifact distal to the transducer often reported in PAM literature (**Figure 3.3**). Multi-focal cases in pork did not result in clear images corresponding to the HIFU foci (data not shown), and single-focus images in pork were blurred compared to corresponding images of phantoms.

PAM magnitude was also significantly lower when sonicating pork. Although standard PAM has been performed in the presence of microbubbles in heterogeneous media [150], we did not use any exogenous agents to act as cavitation nuclei. Our experiments instead relied on spontaneous cavitation of endogenous gas bodies, which generally provide much lower cavitation SNR than microbubbles. PAM has not been used (to our knowledge) to detect endogenous cavitation in heterogeneous media. We hypothesize that lower SNR, increased attenuation and tissue interfaces hindered the algorithm's performance in pork, and that PAM reconstruction could potentially be improved using more robust beamforming, such as the minimum covariance method used by Coviello [148]. However, multi-focal sonications in pork were evident from MR thermal imaging, despite the lack of clear PAM reconstruction.

3.6.3 Temporal evolution of cavitation

One goal of this study was to examine the temporal evolution of cavitation activity during different sonication geometries. In phantoms, the channel variance was predictable with cavitation activity occurring at the onset of sonication. Cavitation was highest during single focus sonication and depleted rapidly, while multi-focal sonication resulted in cavitation that was initially lower and decayed more slowly. The exponential decay seen in **Figure 3.5a** is consistent with a gradual depletion of cavitation bubbles through inertial cavitation, similar to observations that have been previously reported [138], [151]. In **Figure 3.5a**, transient bursts on top of exponential decay can be seen in the single-focus channel variance curves, but not to the same extent in the multi-focal curves. Similar transient signals have been reported in the past, and are likely caused by the spontaneous nucleation and subsequent collapse of a new endogenous bubble, or by movement of a bubble into/out of the probe focus [138], [152].

During the first second of ultrasound acquisition from phantoms (**Figure 3.6a**), the median and max channel variance in the 4-mm and 8-mm cases were below single-focus values at every power level. However, when considering the entire 30-sec sonication, the difference between single- and multi-focal channel variance decreased substantially, with the 4-mm case having slightly greater median and average channel variance compared to the single focus above 40W (Figure **3.6b**). We hypothesize that cavitation nuclei depleted rapidly in single-focus sonications, resulting in similar channel variance to the 4-mm case when averaged over 30 seconds. In the broadest beam (8-mm) average cavitation was lower at all powers (**Figure 3.9b**).

In pork samples, multi-focusing produced lower channel variance than single-focusing at all power levels. Channel variance remained at a low level in sonications below 40W. At 60W and 80W, short-lived spikes were present, potentially signaling spontaneous nucleation and collapse of cavitation bubbles at the focus. Solid lesions appeared at 40W and above in pork. The presence of both lesion and sporadic acoustic bursts is consistent with a previously reported association between lesion formation and the acoustic signature of cavitation [153]. There were no acoustic spikes observed in multi-focal sonications of pork samples, nor were visible lesions formed.

3.6.4 Diffuse heating with multi-focal ultrasound

In phantoms and pork, both multi-focal patterns had lower peak temperature and generated mild heating (ΔT=3-8°C) more consistently spread over a volume of interest than the single focus. In phantoms, most cavitation was observed soon after the sonication and prior to significant heating. This suggests the reduction in cavitation activity was primarily due to smaller acoustic pressures when using multiple foci. Therefore, these data confirm the hypothesis that, in mild hyperthermia applications where cavitation is undesirable, multi-focusing is a potential option to achieve the desired temperature elevation at reduced pressure.

3.6.5 Study limitations

It should be noted that the sonication protocols used do not reflect a practical hyperthermia treatment protocol. For example, voxel temperatures were allowed to exceed the mild range since feedback control was not used. Our group has experience with mild hyperthermia feedback (e.g. Poorman *et al.* 2016, [154]) but the present study was instead designed to observe the onset of cavitation at matched powers, and we showed that it is less likely to occur in multi-focusing at a given input power.

Temperature rise and cavitation threshold were dramatically different between phantoms and pork. In our study, mild-hyperthermic heating was achieved in pork below the cavitation threshold. Pork samples had a higher thermal absorption and higher cavitation threshold than phantoms. Thus the multi-focal approach may be most advantageous when sonicating tissues with low cavitation threshold, such as adipose tissues [39], [152].

We also traded temporal resolution for spatial coverage by using a low receive duty factor (0.2%) in our study, similar to what has been used previously in cavitation monitoring [151]. With this duty factor, PAM yielded ~1MB per image frame (600MB per sonication). Echoes from repeated cavitation events (<50 ms) could be missed in our acquisitions, though results from other studies of transient cavitation with better temporal resolution suggest many cavitation bursts are longer than 50 ms when applying CW or long HIFU pulses [137], [138]. A systematic study of cavitation burst duration in continuous wave HIFU with 100% receive coverage was not found in the literature, however the work of Li *et al.* is informative. That study used a series of 60, 1ms HIFU pulses to measure the threshold, probability, and persistence of cavitation in different materials. They found a rapid transition to 100% cavitation probability above the cavitation threshold of 3MPa in agarose [39]. Since we were likely above the cavitation threshold in most phantom experiments (based on exponential decay of variance), this suggests that even at the 20 Hz frame rate cavitation events could be detected. In pork it is less clear what events may have been missed, since there are clearly short transients that were detected lasting just 1-2 acquisitions at 40W and above (small ‘blips’ in **Figure 3.5b**).

Finally, our study would benefit from robust quantification and mapping of the acoustic field produced by the Sonalleve at all power levels tested, since at higher powers, increasing acoustic non-linearity would change the ratio of PNP. Ideally, an optical hydrophone would be used to measure peak negative pressure in each sonication scenario, but this was not available. Recasting the results from acoustic watts to free-field acoustic pressures at the foci would help define PNP thresholds for cavitation.

3.6.6 Potential applications

The general conclusion from this study is that diffusing the beam of a spherically-focused HIFU transducer may be advantageous when performing mild-hyperthermia, because the risk of cavitation can be reduced. A simple way to achieve beam diffusion is by using multi-focal sonications with an array transducer or alternatively, single-element transducers could be diffused via an acoustic lens [155]. Increasing the number and spacing of foci diffuses the beam and decreases peak negative pressures. We have demonstrated this trend in two specific patterns. However, if the beam becomes too diffuse then it may be difficult to achieve therapeutic temperatures or to target specific tissues. Also there is a risk of axial grating lobes reaching therapeutic intensities, so simulations and hydrophone measurement should be used to understand beam shape relative to the therapeutic application. In all cases, beam diffusion can reduce cavitation, but depends on the specific transducer (curvature, aperture, focal gain, sonication frequency, etc.), as well as the morphology of the targeted tissue. Other possible advantages of multi-focal sonication such as shaping of the heated region are discussed in Partanen et al. [17]

The simultaneous broadening of the heated zone and reduction in cavitation level may be advantageous in a number of ultrasonic therapies where heating in the absence of cavitation is desirable. Studies using mild hyperthermia to activate biological pathways such as apoptosis or immune responses might use this technique to avoid confounding effects from mechanically-induced cell damage, which has been shown to directly correlate with inertial cavitation dose [69]**.** Many researchers are currently studying temperature-sensitive drug carriers loaded with chemotherapeutics. Thermally sensitive liposomal carriers loaded with doxorubicin have been used pre-clinically with ultrasound-induced hyperthermia to effectively treat several cancer models [70]–[74]. Molecular dynamic simulations have suggested that protein structures can be significantly modified by acoustic shockwaves and nanometer scale jets, and cavitation-produced free radicals may also alter the efficacy and toxicity of therapeutic molecules [143], [144]. The multi-focal methods used in our study can deliver mild hyperthermia in the absence of cavitation and may be preferable in instances where mechanical cavitation could hinder dose delivery.

3.7 Conclusion

Multi-focal HIFU was used to achieve mild temperature elevation with reduced cavitation activity. Cavitation activity was monitored using the variance and PAM on two transducers. PAM was able to resolve multiple foci in the phantoms and image magnitude was highly correlated with channel variance in both pork and phantoms. Multi-focal HIFU can be used in the future in conjunction with feedback control to perform mild hyperthermia treatments with less probability of cavitation.

CHAPTER 4
OPTICALLY-TRACKED FUS IN TRANSCRANIAL NEUROMODULATION

4.1 Introduction

Transcranial FUS is a method for non-invasively modulating neurons of the central nervous system with a focused acoustic beam. As was emphasized in Chapters 1-2, spatially selective neural modulation with FUS requires accurate targeting of the focus to the brain region(s) of interest. While MR-based guidance with calibrated positioning systems were shown to have 1-2 mm targeting accuracy in Chapter 2, the 5 degree-of-freedom (DOF) manual positioning system used in our neuromodulation experiments requires a different approach to guidance. This is in mainly due to the complexity of designing an accurate 5 DOF stage that can move with requisite accuracy and repeatability while also maintaining good transducer coupling with the animal head. In addition, many of the systems cited in Chapter 2 used phased-arrays that allow steering and adaptive re-focusing, and the applications allowed pilot thermal sonications for target verification. Our needs are distinct in that we manually position and couple a single-element transducer, and have no ability to verify targeting during *in vivo* experiments via thermometry, since heating would be potentially harmful to the animal or confound the experimental test for direct acoustic neuromodulation. Alternative target verification using MR ARFI is a possibility, but low sonication pressures and corresponding small displacements make detection difficult. This chapter presents our solution to these problems using a novel method for calibration and real-time optical-guidance in co-registered magnetic resonance (MR) images. The calibrated system is used for targeting the sensorimotor cortex (S1) in live rhesus macaques.

The calibration method developed here uses a brass hydrophone facsimile designed to reflect the real hydrophone dimensions, and is attached to an optically tracked body for a standard pivot calibration. A second tracked body is mounted to the transducer. Replacing the brass copy with the real hydrophone, tip locations can be measured by the optical positioning system during acoustic data acquisition, allowing localization of acoustic data voxels relative to the transducer. Accuracy (TRE) of the method was assessed with multi-slice MR thermometry in phantoms and shown to be in the range of conventional optically-guided surgeries. Beam mapping results from an interior cavity skull of the skull are presented in Chapter 5, but the hydrophone tracking presented in this chapter is relevant to those results.

The new approach enabled two unprecedented experimental techniques: real-time projection of the approximate FUS beam shape during targeting, and beam mapping along the interior surface of an *ex vivo* skull. Real-time beam projection further allowed direction estimates of displacement from acoustic radiation force, yielding motion encode gradient vectors with near maximum sensitivity for MR ARFI. The calibrated system was used in *in vivo* sonications with MR ARFI in a rhesus macaque monkey, and – to our knowledge – the displacement maps presented in this chapter represent the first of their kind from transcranial FUS in a large (non-rodent) live mammalian head.

4.2 Summary

Methods: An optically-tracked hydrophone was used to acquire free-field beam maps of the transducer in a 3D printed coupling cone, at 802 and 250 kHz. Data were stored in a volume/affine representation, and projected with 3D Slicer during targeting. The transducer was positioned until the projected focus aligned with the desired target in a pre-acquired, co-registered MR scan. Several rounds of phantom trials established targeting accuracy, using MR thermometry as the ground truth. Following validation, sonications in live animals targeting S1 were performed. *In vivo* displacement induced by acoustic radiation force was measured using MR ARFI (acoustic radiation force imaging). The projected focus

length provided an estimate of peak displacement direction, and motion encode gradients were aligned to maximize ARFI sensitivity.

Results: Initial calibration resulted in an average error of 3.26 mm (min – max: 2.80 – 4.53) between the projected beam and thermal hotspot. Redesigning tracked rigid bodies resulted in an improved calibration with error 2.43 mm (0.79 – 3.88). Real-time projection of the beam provided estimates of the focus extent and direction. *In vivo* ARFI showed low-level diffuse displacement peaking at 1 μm, with qualitatively similar shape and extent as projected beam profiles, but shifted due to tracking error and refraction through the skull. Average error in gradient alignment deduced from phantom experiments was 1.4˚. To our knowledge, this is the first reported measurement of acoustic displacement in a large mammalian skull.

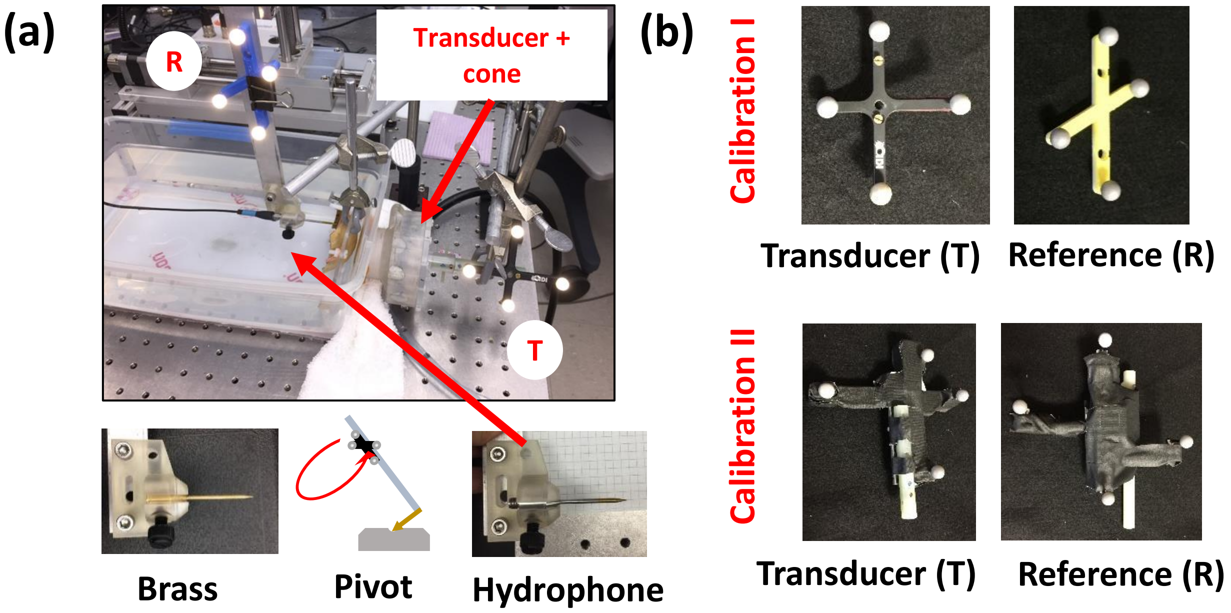

Figure 4.1 ***(a)*** *Setup used for optically-tracked calibration. The brass tip offset from rigid-body tracker* ***R*** *is measured using a standard pivot test, then replaced with the real hydrophone. Beam mapping is performed with tracker* ***T*** *mounted to the transducer cone, and the hydrophone tip localized in the* ***T*** *coordinate frame. A skull piece appears in the image, but calibration beam maps were collected without the skull.* ***(b) Calibration I*** *used the top set of trackers, and* ***Calibration II*** *used the bottom set, which are larger and MR safe. During MR targeting, the* ***R*** *tracker is used as a global reference. The bottom set were wrapped in black tape to reduce optical reflections.*

4.3 Methods

Detailed technical development of the calibration and tracking experiments that were performed is given in the following sections.

4.3.1 Materials

A spherically focused, piezoceramic single-element transducer used for all experiments (H115, Sonic Concepts). It has geometric focus of 64mm and opening diameter of 63.5 mm, and sonications were performed at resonance peaks of 250kHz and 802kHz. A custom 3D printed coupling cone with 3-cm

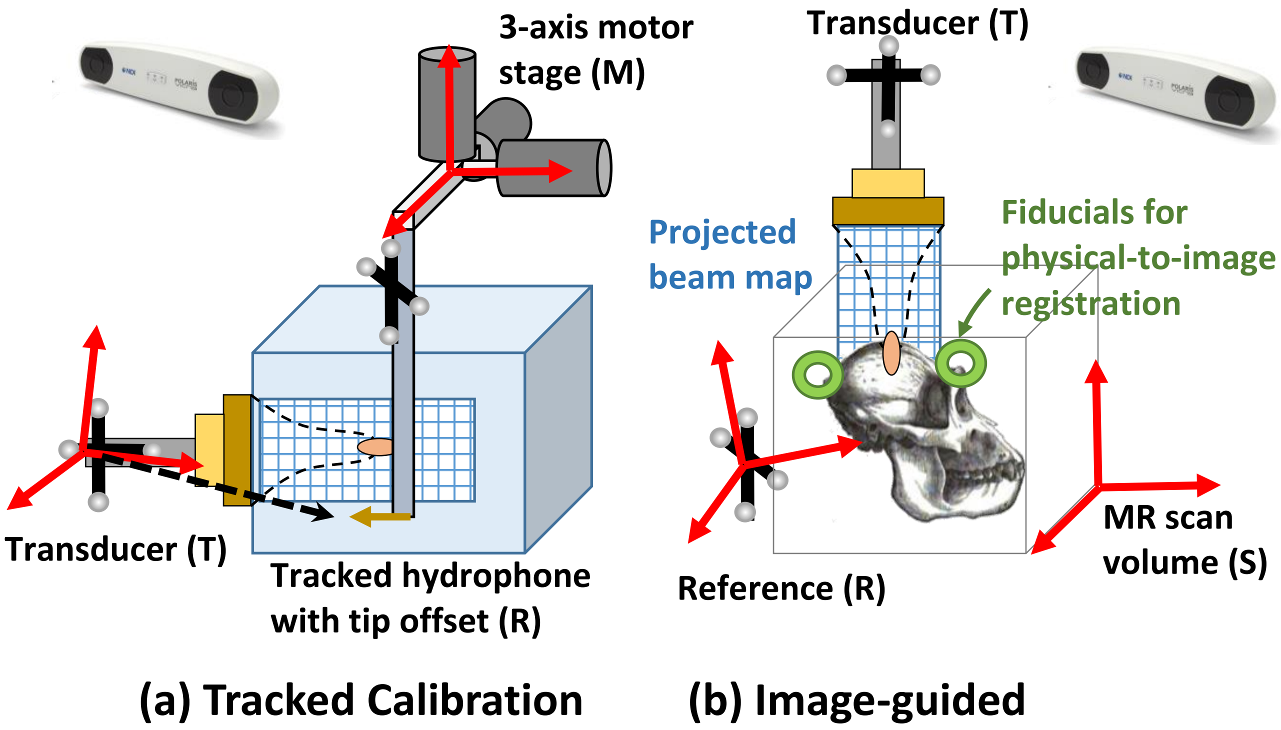

Figure 4.2 *Coordinate systems involved in projecting beam voxels into MR image space. Acoustic voxels are defined by the motor stage (M), registered to the tracked position of the hydrophone tip, and converted to transducer coordinates (T). At the scanner these acoustic voxels are projected into MR scan volume (S) after fiducial registration. The reference (R) is used when localizing fiducials in physical space and tracking the transducer.*

opening aperture held the transducer. Acoustic data were collected with a needle hydrophone (HNC 0400, Onda Corp., Sunnyvale CA). A 3D printed housing adapted the hydrophone for secure mounting to the motion stage **(Figure 4.1a)**. An NDI Polaris Vicra tracking system was used for all optical guidance (Northern Digital Inc., Waterloo, Ontario CA), with two sets of rigid body trackers. In the first two rounds of calibration experiments, a small 3D-printed tracker and a metal tracker from NDI (removed before each scan) were used as the reference and target tracker, respectively (**Figure 4.1b**). In the final experiment, two custom trackers were built with LEGO© parts to have larger intra-sphere distances and be MR-safe (**Figure 4.1b**). Rigid body files were created with the NDI 6D Architect software. Donut-shaped MR-visible fiducial markers were used for image registration (MM3003, IZI Medical Products). All MR scans were in a Philips 7T, using a custom single-channel surface coil and threaded housing that attached to the transducer cone at the aperture. All phantom sonications were in tissue mimicking gel

(1% agarose, 4% graphite powder, attenuation ~0.5 db/cm).

4.3.2 Calibration and Optically Tracked Beam Mapping

Beam maps were collected in water at both 250kHz and 802kHz, using a low duty cycle, low amplitude pulse (100 cycles every 50 ms, peak focal pressure ~400kPa), and a 3D step resolution of 0.4mm. Pressures were measured with the needle hydrophone attached to a three-axis motion stage. Hydrophone signals were digitized and recorded using a PicoScope (model 5242B), programmed via the open source *pico-python* interface available on GitHub (github.com/colinoflynn/pico-python). Signals were pass-band filtered (4th order Butterworth, 3dB band 50kHz – 1600kHz), and the voltage envelope averaged over 15 cycles to compute the field value at that motor position. The result is a voxelized map of the free-field max pressure that can be projected into volumetric image data during tracking. An affine transformation matrix with motor step sizes along the diagonal was used to convert acoustic voxel index to the motor spatial coordinates.

The scheme depicted in **Figure 4.2** was used to register acoustic voxel data into optically-tracked coordinates. Prior to beam mapping, a rigid body (tracker **T**) was firmly mounted to the back of the transducer cone, and used as the global reference during beam mapping. A second tracker **R** was attached to the hydrophone mounting rod and a standard pivot-calibration localized the needle tip. Since needle hydrophones are sensitive to damage to forces applied at the tip, a brass facsimile was fabricated and mounted in place of the real hydrophone, and the pivot calibration performed. This yielded the tip offset relative to tracker **R** with RMSE=0.31mm. The hydrophone was inserted and the tracked mounting rod attached to the motion stage. The transducer+cone+tracker assemblage was then coupled to the side of the water tank.

Before and after each 3D beam map, a co-registration grid to convert motor axis positions to tracked coordinates was collected by moving the tracked hydrophone in 10mm steps over a 3D volume, recording both the tracked hydrophone positions and the step position along each motor axis. Rigid point-based registration was used to solve for the motor-to-transducer transform to convert between motor xyz, acoustic voxel index, and tracked transducer coordinates. Collection of this grid was repeated several times at various camera angles and positions, yielding an average motor-to-transducer registration (all FRE under 0.2 mm). Applying the tip offset derived from the brass facsimile results in a series of transforms to localize acoustic beam voxels in the reference frame of the tracked transducer, enabling real-time projection of the beam. Acoustic voxels and the affine were stored in NIFTI format for loading into 3D Slicer.

The previous step required acquisition of a large number of data points from the tracking system, so acquisition and motor translation were automated. An interface module was built (Python/C++) to programmatically record position and quaternions from the tracking system, utilizing the TCP socket-based Open IGT Link (openigtlink.org) and Image Guided Surgery Toolkit (igstk.org) libraries. Within the beam-mapping program, an IGT link server was created, and tracking data broadcast to this socket address using a client program.

In total, two sets of trackers (the initial design and the re-design) were used to independently calibrate the H115 transducer. **Calibration I** was used in the initial two experiment rounds. **Calibration II** was used in the final round. **Calibration Ib** used below will refer to Calibration I with a prospective bias-correction applied during targeting.

4.3.3 MR-guided Experiment Setup

MR thermometry was used to measure the accuracy of the calibrated FUS probe. A removable plexiglass bed was created with a manual 5-DOF positioning system that situates the transducer on the target. The bed has a stereotactic frame meant for holding the head of a macaque monkey during FUS procedures. The calibrated tracker was mounted to the back of the transducer, and the second tracker fixed to the plexiglass bed to act as reference. The transducer was manually navigated and secured with thumb screws on the positioning system.

4.3.4 Registration and Targeting

In both phantom and animal experiments, six fiducials (Multi-modal Fiducials, IZI Medical Products) were placed around the target volume, in a spatially distributed (non-clustered) manner similar to [131]. The stereotactic bed held the reference tracker, the transducer, and coil. The bed was placed in the magnet for an initial anatomical scan. A 3D T1-weighted TFE scan (Philips THRIVE), resolution 0.4 x 0.4 x 1mm with TR 4 ms and TE 1.9 ms, showed the fiducial locations in image space (MR patient coordinate convention "RAS+" – Right, Anterior, Superior—assuming a head-first supine patient orientation). The bed was removed, data downloaded to the tracking PC, and fiducials localized using 3D Slicer software (slicer.org) to navigate through image planes and select fiducial centroids.

Tracking was initiated with 3D Slicer and the OpenIGTLinkIF module. An NDI tracked probe, with a well-calibrated tip position, was inserted into each fiducial and its position recorded, relative to the reference tracker. Fiducial registration in Slicer solved for the physical-to-image transform. The transform was applied to the tracked transducer, causing a real-time overlay of the free-field beam to appear on the guidance image in Slicer. Finally the transducer was manually positioned until the projected focus aligned with the target. Random jitter was observed in the real-time overlay due to statistical localization error (same as FLE) of the tracking system. The location and orientation of the transducer at the targeted position were recorded for subsequent error analysis.

4.3.5 Sonication in Phantoms to Measure TRE

A total of three rounds of experiments were conducted to measure TRE in phantoms. Continuous wave FUS sonications were performed at 802kHz and 250kHz for 30 seconds. Input voltages corresponded to roughly 1 MPa free-field pressure. Thermometry scans were multi-slice volumes with 7 slices angulated to lie roughly parallel to the focal plane of the transducer. Scan voxels were 1.5 x 1.5 x 3 mm, with a dynamic scan time of 5 seconds for the full volume (EPI factor 3). Temperature maps were computed using the proton resonance-frequency shift (PRFS) method, in which temperature change is proportional to phase change from a baseline. Four initial dynamics without FUS were collected as a baseline.

In a first round of experiments (N=6) a large rectangular phantom was created with a regular grid of water columns to serve as guides for target selection. The phantom was held in a plastic holder, and fiducial markers placed around on the walls of the phantom holder, and the setup was initially placed in the magnet. After initial registration, the transducer was pointed directly down and positioned to target the center point of a grid square, moving to a different section in each trial. After each targeting session, the metal tracker was removed, the table returned to the magnet, THRIVE and thermometry scans collected.

From analysis of the initial round of experiments we observed an error distribution that was larger than expected and biased mainly in one direction by ~2 mm, results consistent with Kim et al. [103]. We derived a similar MR based calibration, yielding an approximate shift of (x,y,z) = (1,2,0) mm that could be prospectively applied in the local axes of the transducer to correct for bias. On a different day we performed a second round of trials (N=5). Trials 1-3 tested the MR-based bias-correction by prospectively applying it to the beam overlay during targeting. Trials 4-5 used the regular calibration. Positioning of the reference tracker and camera differed between the two days' experiments. The transducer, phantom, and image fiducials were in approximately the same place.

A third round of experiments (N=5) was performed, this time only at 802 kHz. Experience gained in the initial two experiments led to several changes in the setup in an attempt to isolate technical error (due to calibration, optical guidance, FLE) from intra-operative phantom motion, and reduce the overall error observed. Thus the third round used a phantom coupled directly to the cone in a rigidly attached cylinder, and fiducial markers attached to structures on the plexiglass table instead of the phantom holder. In each trial the transducer+phantom assemblage was translated and rotated to different angles to simulate targeting around the head. Tracked bodies were re-designed to be MR-compatible and have the following changes, based on the work of Fitzpatrick and West [127], [128]. First, the distance between reflective spheres was increased by several cm, which has the result of reducing TRE due to increased RMS distance of the spheres from each principal axis ($f_k$term in the denominator of equation (4) in [127]). Second, sphere mounting was improved to make the optical centroid agree more closely with the design value. These changes reduced possible mis-registration from movement of the phantom and fiducials, and error associated with tracker configuration. Configuration error is a possible source of error bias (see Discussion).

4.3.6 Sonications *in vivo*

The final calibration (II) was used to target the sensorimotor cortex (S1) of two macaques. Four imaging fiducials were placed on the stereotactic frame and two on the head, and the same THRIVE scan was used for localization and targeting of the S1 region. Sonications were performed at both 250 kHz and 802 kHz after rigorous safety validation. Beam projections were used to estimate the acoustic axis in MR coordinates and align MR gradient direction for optimal sensitivity.

4.3.7 Acoustic Radiation Force Imaging (ARFI)

Motion encode gradient (MEG) components were determined by projecting the focus and aligning a vector along its long axis. Displacement images were acquired using a spin echo 2D MR-ARFI sequence implemented with parameters: FOV/matrix/voxel size 120x120x2 mm^3/60x60x1/2 mm^3 isotropic; TE/TR 15/1000 ms; 27° flip angle; multishot EPI readout with 5 shots per TR (EPI factor 3). Repeated unipolar

MEGs were used for ARFI encoding, with gradient duration/strength 3 ms/40 mT•m^{-1}. The second MEG was synchronized with an ultrasound emission using TTL outputs sent to the transducer. Sonications were performed at a low duty cycle (4.5 ms every TR or 1000 ms). Displacement images were reconstructed by subtraction of four phase images (ϕ^{ON+}, ϕ^{OFF+}, ϕ^{ON-}, and ϕ^{OFF-}) using opposite MEG polarities with FUS turned on or off: $\Delta d = \frac{(\phi^{ON+} - \phi^{ON-}) - (\phi^{OFF+} - \phi^{OFF-})}{2\gamma G\tau}$

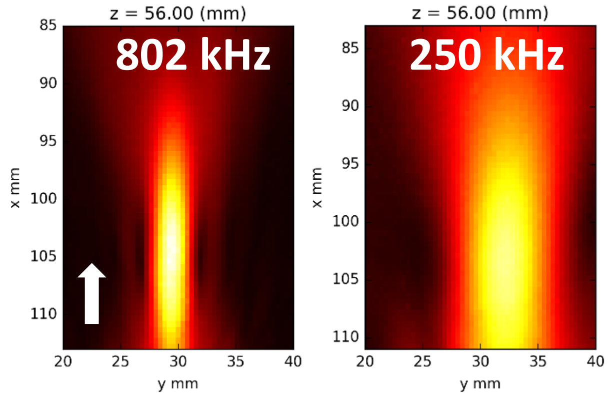

Figure 4.3 Axial slice through beam maps at each frequency showing peak receive voltage. The coupling cone opening is approximately 2mm from the bottom of each figure. The white arrow indicates sonication direction. Axes list the motor coordinates. The transducer and motors were not in exactly the same position in each case.

4.3.8 Data Analysis

Three independent sets of independent data were obtained from phantom error studies, with N=6, N=5, and N=5 trials, respectively. Each trial includes the predicted target, the quaternion/position of the transducer over the target, a physical-to-image fiducial transform, and the temperature maps. Data were loaded into an IPython notebook. To calculate TRE, temperature volumes were slightly smoothed with a Gaussian kernel (sigma equal to 0.5x the voxel size in each dimension) to account for spatial noise, and linearly interpolated to a resolution of 0.25mm. Next, acoustic voxel data were linearly interpolated into the subsampled image grid with the same the chain of transforms used during targeting. Finally, TRE was computed using 3D cross-correlation of the temperature map and the interpolated, projected acoustic data, which results in the offset between the two.

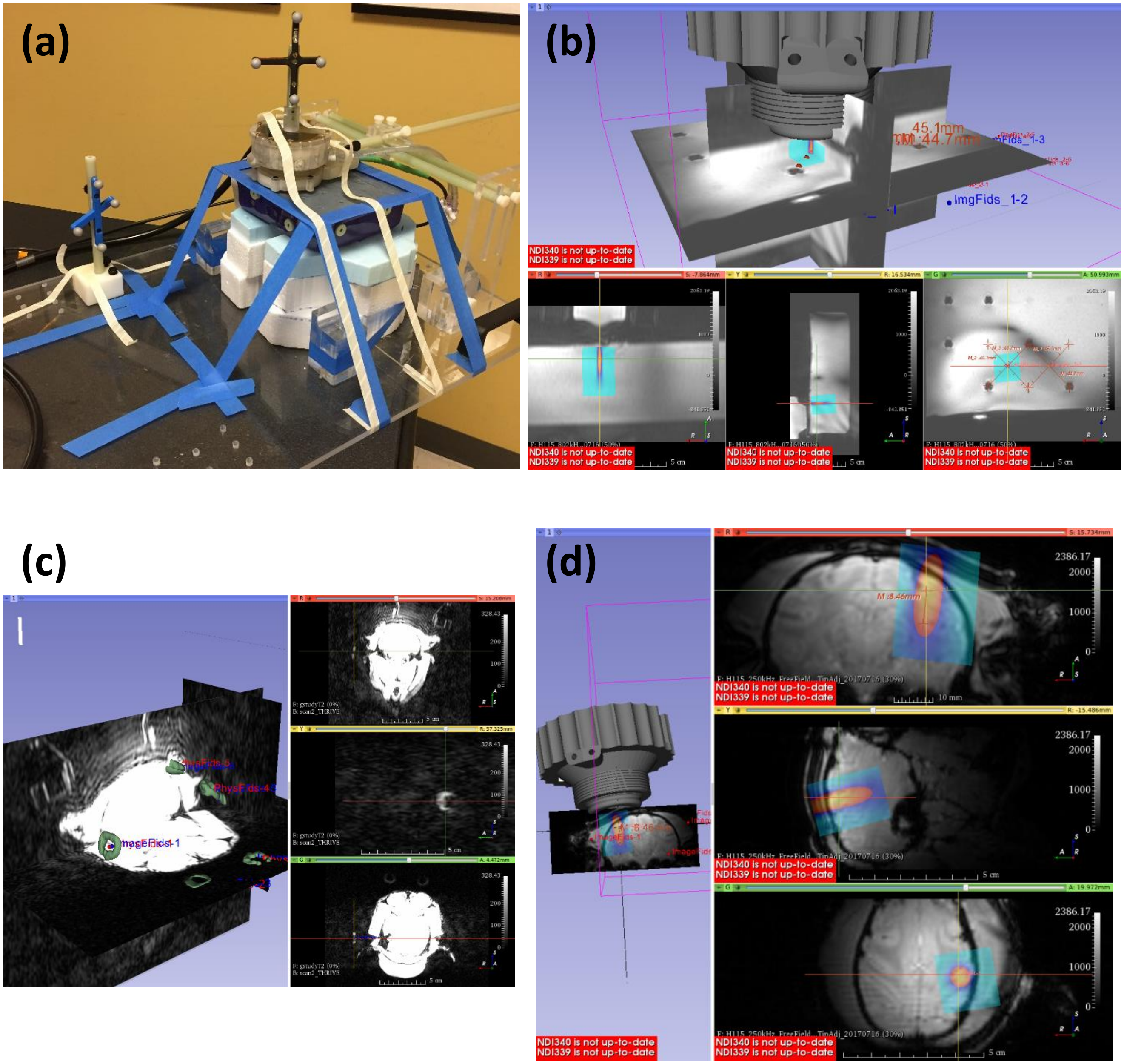

__Figure 4.4__ (a) Setup of transducer, reference, phantom and fiducials during accuracy tests. The approximate alignment of MR coordinate axes is drawn for reference. (b) Screenshot showing real-time beam overlay in 3D Slicer on the THRIVE guidance image. Targets were selected as the grid centers and the transducer moved until the beam projected was centered on each target. (c) Screenshot showing fiducial selection and registration in Slicer during an animal experiment. Image fiducials have been manually segmented and appear green. (d) Real-time beam overlay targeting the S1 cortex

4.4 Results

Beam maps (**Figure 4.3)** show that the H115 inside the coupling cone is focused roughly 1cm beyond the cone aperture. At 802 kHz the focus had a full-width at half-maximum (FWHM) of 2.31 mm in the transverse direction, and at 250 kHz transverse FWHM was 7.53 mm. Axial focal length was not determined in the same manner because the pre-focal half-maximum occurs behind the coupling membrane inside the cone. Distance from the peak to post-focal half max was 9.1 mm at 802 kHz and 31.5 mm at 250 kHz. Real-time targeting with 3D slicer projected beam maps onto desired targets (**Figure 4.4 b,d**). Fiducial selection and registration is shown in **Figure 4.3c**. Example temperature maps showing the hotspot and projected beam map contours are presented in **Figure 4.5**. These were created in post processing using the saved transducer position and physical-to-image transforms.

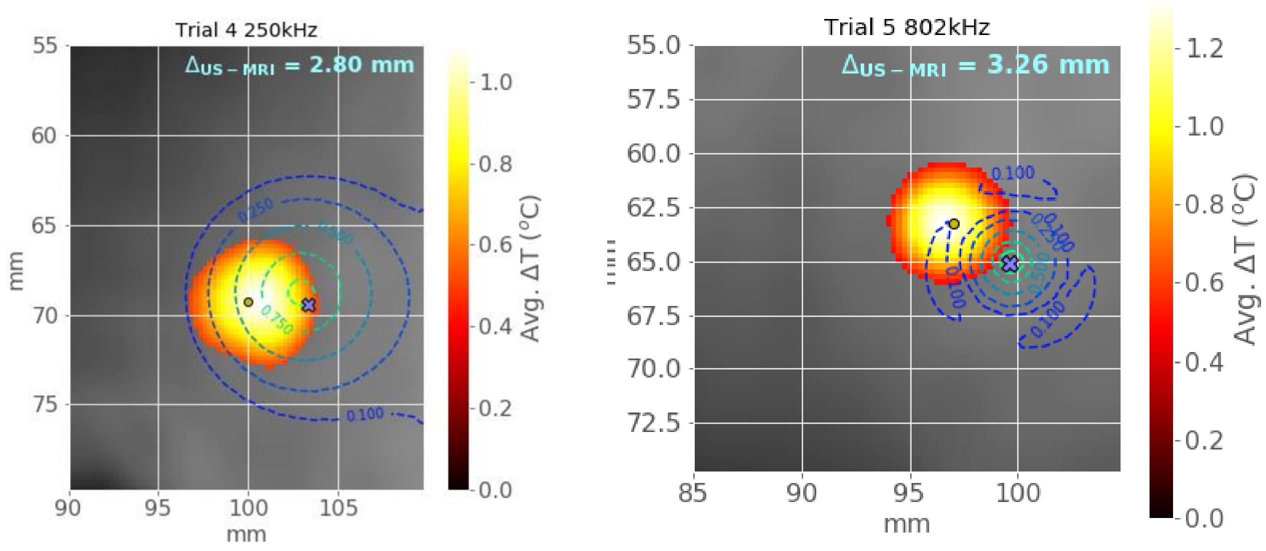

__Figure 4.5__ (LEFT) Setup of transducer, reference, phantom and fiducials during targeting. The approximate alignment of MR coordinate axes is drawn for reference. (RIGHT) Screenshot showing real-time beam overlay in 3D Slicer on the THRIVE guidance image. Targets were selected as the grid centers and the transducer moved until the beam projected was centered on each target.

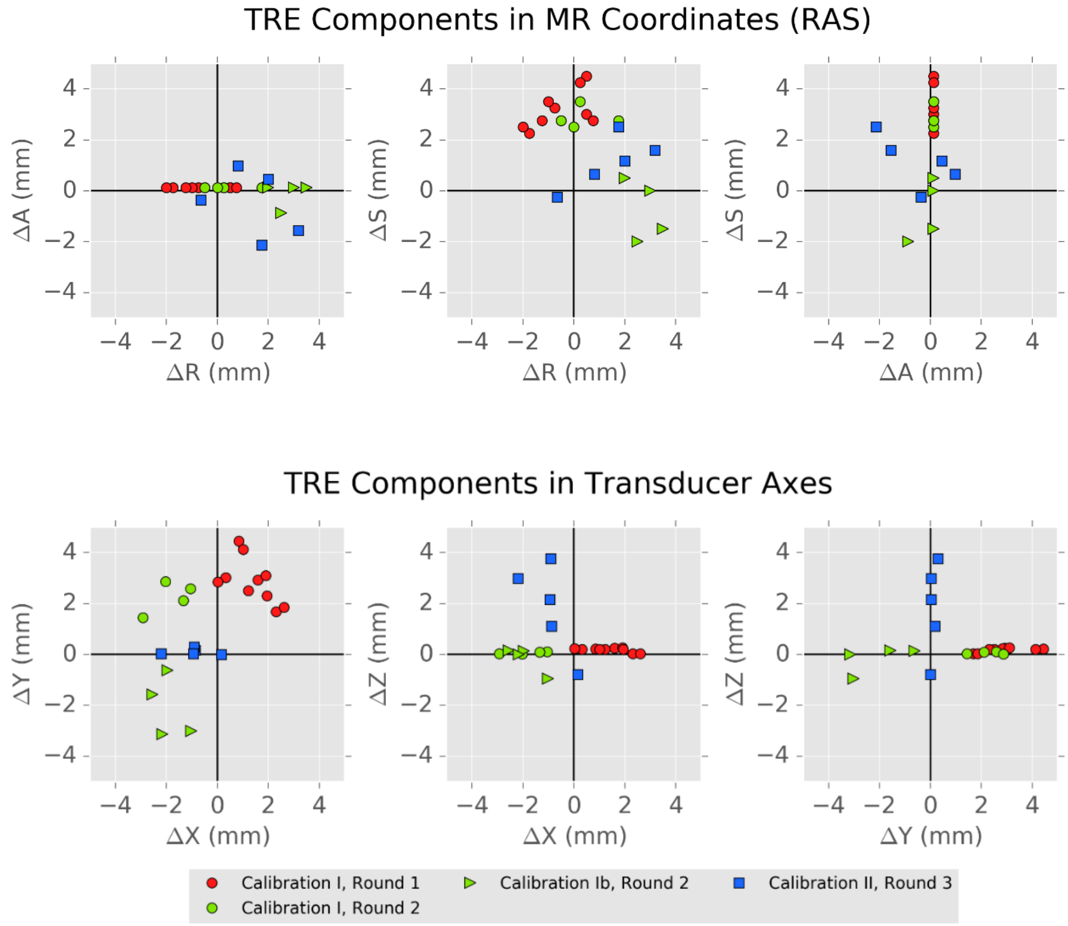

Figure 4.6 Vector components of targeting registration error (TRE), computed as measured – predicted (i.e., MR hotspot – overlaid beam). The top row shows errors in MR coordinates using the Right, Anterior, Superior (RAS+) coordinate convention. Bottom row shows the same errors with respect to the calibration axes of the transducer. If there were only statistical error in localizing fiducials, TRE components should be symmetrically distributed about (0,0) in each plot. Comparing Rounds 1 and 2, it is clear that applying an offset in the transducer coordinate frame does not correct bias observed in Round 1.

Figure 4.6 plots the computed error (TRE) from 3D cross-correlation in the three rounds of experiments. In the first round, Trial 1 was excluded from averaging because of poor coupling that caused surface heating, leaving Trials 2-6 (N=5) for analysis. The average error across the remaining five trials was 3.31 (2.80 – 4.53) mm at 250 kHz and 3.40 (2.85 – 4.26) mm at 802 kHz, where the values are given as "mean (min – max)". The predicted focus in the axial direction was consistent with the maximum temperature slice (within .25 mm) in the smoothed and interpolated data. An apparent bias in the components of TRE was observed in RAS coordinates (**Figure 4.6**). Using the recorded tracker orientation, this bias was converted to transducer axes to derive an offset correction to the calibration:

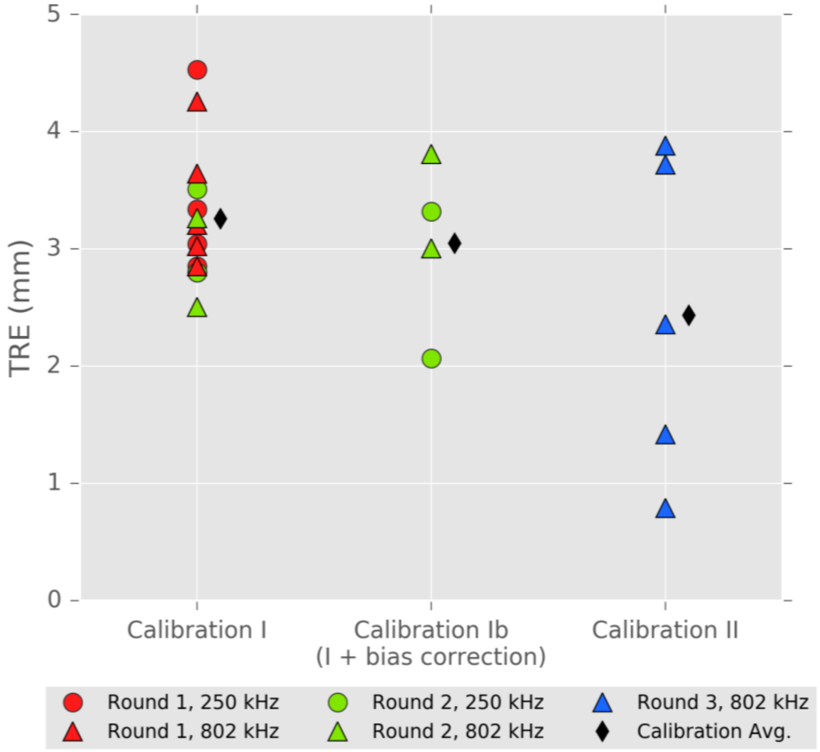

Figure 4.7 *Summary of targeting error magnitudes observed during phantom trials. Group averages were 3.26 mm (I), 3.05 mm (Ib), 2.43 mm (II). The small improvement between I and Ib was not statistically significant (p=0.55). Improvement between I and II was more significant (p=0.07). See Results and Discussion sessions for detailed analysis.*

(x,y,z) = (1,2,0) mm (magnitude 2.2 mm).

In the second round, the above correction was prospectively applied during tracking in Trials 1-3 ("Calibration Ib"). Surface heating resulted in exclusion of Trial 2. As can be seen in **Figure 4.6**, the bias correction did not appear to fully improve errors observed in Round 1, instead rotating the error to a different axis. Trials 4 and 5 did not use the bias and thus are included with Calibration I data. In the third round, error was reduced using the new trackers (Calibration II).

In summary, average error across Calibration I unbiased trials was 3.26 (2.80 – 4.53) mm, and the biased trials 3.05 (2.06 - 3.81) mm. Calibration II error was reduced to 2.43 (0.79 – 3.88) mm. Error magnitudes are plotted in **Figure 4.7.** Significance between calibrations was evaluated with an independent two-tailed T test. Average error from Calibration Ib (n=4) was not significantly different from Calibration I (n=14, *p*=0.55). Calibration II (n=5) had a more significant reduction vs. Calibration I (*p*=0.07).

In vivo sonications revealed focal displacement overlapping the predicted beam only at 802 kHz in both animals (**Figure 4.8**). Displacement was not visible at 250 kHz in either animal. In animal two, an initial sonication showed no evident displacement. After repositioning the transducer to have a smaller incidence angle on the skull bone, focal displacement was observed, suggesting critical angle reflections in the first trial. At 802 kHz diffuse focal displacement magnitude with spatial peak ~1 µm was observed in each animal. The distance between the predicted focus and displacement peak in lateral-plane ARFI was larger than in phantom thermometry (5.8 mm in animal one, and 6.3 mm in animal two).

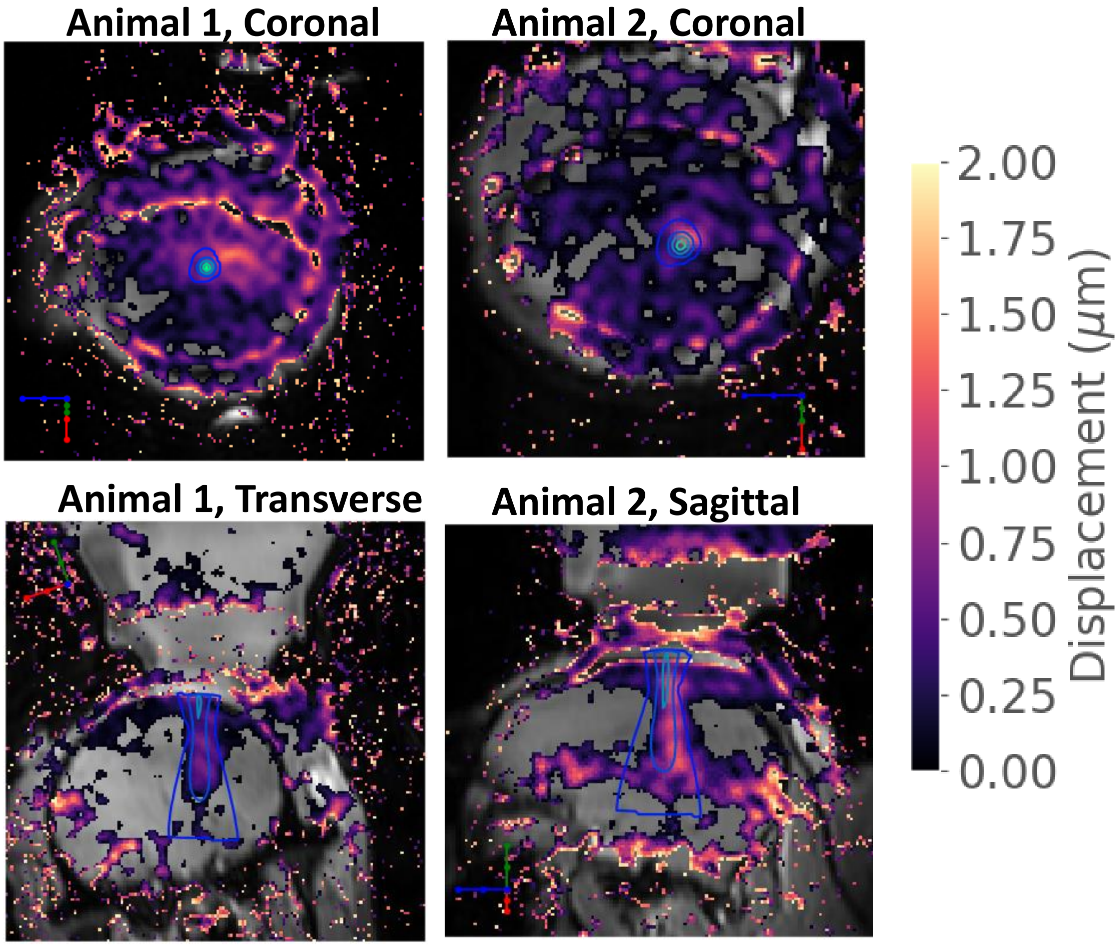

Figure 4.8 *Displacement maps (ARFI) acquired in several planes in two animals. Gradients were aligned by estimating the focal axis direction from projected beam maps. 802 kHz beam contours are overlaid. The background grayscale is a THRIVE scan taken after targeting and returning the animal to the magnet.*

4.5 Discussion

4.5.1 Tracking Accuracy and Error Sources

From the three independent experiment rounds, Calibration II had the smallest total error. It was performed with redesigned trackers that were MR-safe and required no-intra operative removal, reducing likelihood of post-registration motion errors. The trackers used in Calibration II also had a larger spatial baseline that is predicted to reduce statistical TRE. Calibration I yielded the largest errors observed, but was still within the characteristic range encountered in optically-tracked image-guided surgery (1.3 – 3.9 mm). However, errors were not distributed in a spatially symmetric manner, which goes against optical tracking literature that components of TRE along an arbitrary axis should be zero-mean and normally distributed [127], [128]. The presence of a bias during calibration, perhaps due to discrepancy between the brass and needle hydrophone tip, was hypothesized from the initial data set and prospectively applied to the calibration in a second round. Slightly reduced error was observed but appeared biased in a different direction and was not statistically significant.

The MR-inferred bias from Calibration I is not due to an offset that can be trivially corrected during targeting. Instead it is likely a result of error in localizing image fiducials, intra-operative motion, magnetic field in-homogeneity that distorts image volumes and temperature maps, or configuration

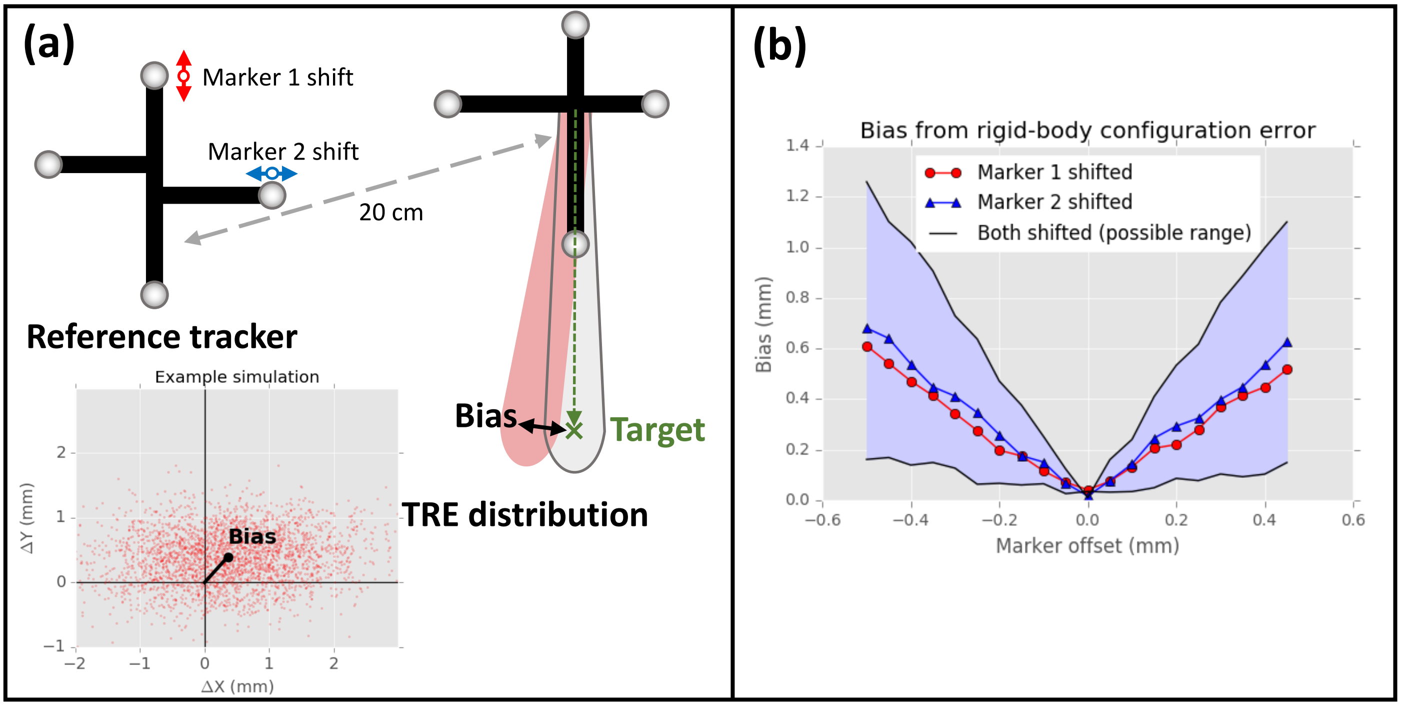

Figure 4.9 *Simulations of configuration error show it is a possible source of targeting error bias. (a) Overview of simulations and an example iteration showing the statistical distribution of TREs. (b) Range of possible bias error introduced by shifting markers 1 and 2.*

errors in the tracked rigid bodies, none of which can be readily corrected with present data. Observed bias using Calibration I lay mainly in the ‘S’ direction in RAS patient coordinates (**Figure 4.6**). This might suggest distortion in the image volume. Alternatively, bias error when localizing fiducials in physical space might explain TRE bias, since the transducer, phantom and fiducials were in similar locations in rounds 1-2. Several of the donut-shaped fiducials were difficult to access with the tracked probe, perhaps leading to repeated localization errors. In Calibration II, a small bias in ‘S’ and ‘R’ directions was observed, but was significantly less than with Calibration I.

Configuration error in one or both of the optically-tracked bodies may also have contributed to the observed bias. The theoretical prediction that TRE components have zero-mean assumes a zero-mean, symmetric distribution of FLE components [128], [156]. However, if one or more of the tracked passive spheres is physically offset from what the tracking software expects, the effect is a non-symmetrical FLE distribution that could lead to biased TRE components. To support this idea, simulations were performed with two virtual trackers placed 20 cm apart, with tracker *R* used as a reference for tracker *T* as in the experiments (**Figure 4.9**) [127]. Two of the reflective spheres on the reference tracker were arbitrarily shifted in 0.1mm steps, at first independently and then together, and tracking simulated by adding normally distributed FLE (σ = 0.35 mm isotropic) and registering designed tools to the generated coordinates. An arbitrary target was chosen for tracker A, and its variation with statistical FLE measured. As configuration error increased, a bias in the observed TRE distribution became apparent (**Figure 4.9**).

The custom tracker in Calibration I was 3D printed with a mechanical tolerance ~0.08 mm. However the snap-fit connectors typically used to mount the spheres are metal, so make-shift connectors were made for MR compatibility that resulted in a potentially larger tolerance. Using the NDI 6D Architect software, we estimated this error could be as large 0.3 mm for 1-2 spheres, which might partially explain observed bias. Calibration II trackers used LEGO parts which have tolerance 0.01-0.02 mm.

Finally, independent t-tests were used to conclude that the bias correction was statistically insignificant, and that Calibration II had a genuine reduction in TRE from Calibration I. This tested for the null hypothesis that two sets of observations are drawn from normal distributions with equal mean and variance. However, we know that TRE is not normally-distributed. For isotropic, normal FLE, Fitzpatrick showed the components of TRE are normally distributed along any arbitrary *x,y,z* axes, and $||\mathrm{TRE}||^2 \sim \sigma_x^2\chi_1^2 + \sigma_y^2\chi_1^2 + \sigma_z^2\chi_1^2$ (where ~ means 'distributed like', χ_1^2 is the chi-squared distribution with one degree of freedom, and σ^2 are normal variances of TRE along each axis) [133]. Performing a likelihood test with the accurate probability distribution thus requires knowing or estimating the σ^2 terms, which are position-dependent. In principle this could be done with simulations in future work.

4.5.2 In vivo ARFI

Optical tracking enabled alignment of MR gradients for maximal sensitivity in acoustic radiation force imaging (ARFI) scans. Detection of displacement with MR requires the motion-encode gradient be aligned with the principal displacement direction for peak sensitivity [157], [158]. Since displacement occurs mainly along the FUS sonication axis near the focus, ARFI gradient direction was determined by estimating the principal axis of the cigar-shaped focus in MR coordinates via the projected beam. We can estimate the error on this direction using TRE and the distance from the tracker center to the focus (~120mm). For a TRE of 3mm this gives an uncertainty annulus with half-angle $\theta = 3/120 \text{ rad} \approx 1.43^{\circ}$.

ARFI was able to approximately localize the acoustic focus *in vivo.* In the second animal, no displacement was observed until the transducer was repositioned to have a smaller incidence angle, providing a negative control. Distance to the predicted focus is difficult to estimate because of how diffuse the observed spot was and because ARFI scans are 2D (single-slice). Using peak from coronal slices, the distances were 5.8 and 6.3 mm, larger than the measured TRE in phantoms. The two main causes are likely aberration through the skull, and geometric scaling differences between THRIVE and ARFI scans. Scaling/distortion between overlaid THRIVE and ARFI scans was clearly visible based on the shape of the skull and head in the two scans. Acoustic aberration was almost certainly present, and has been shown to diffuse foci and shift the centroid by several mm [119], [159]. Future neuromodulation studies with phased-arrays will enable either simulation or ARFI-based correction of phase aberration [160], [161].

4.6 Conclusions

A novel method for calibration and real time image-guided targeting was presented, and its error assessed via MR thermometry. The initial method was shown to have an error of 3.26 mm with an asymmetric bias of 2.2 mm, similar to previous results. We provide evidence that the observed bias cannot be corrected by means of a simple vector offset and discuss several possibilities about its origin. Error was reduced to an average 2.43 mm by redesigning the rigid body optical trackers. The new calibration was used to prospectively estimate the primary acoustic propagation direction in MR coordinates to within 1.43˚ uncertainty, enabling alignment of gradient directions for MR ARFI. *In vivo* pulsed sonications at 802 kHz were performed in two separate macaques, and focal displacement of about 1 µm was observed. The system is being used in ongoing studies of central neuromodulation in macaques.

CHAPTER 5
DESIGN OF A NEW PHASED-ARRAY

5.1 Introduction

The previous chapter developed image-guided targeting of a single-element transducer to perform selective neuromodulation. This chapter presents a multi-element array system for transcranial sonications targeting the sensorimotor cortex (S1) of macaques. Although single-element systems have produced promising results in brain neuromodulation ([11], [79], [162]), arrays offer advantages such as electronic steering of the focus, and correction of phase aberrations [7], [29], [30], [163]–[167]. Array-based systems for transcranial ablation exist for human subjects, but thus far they have all been designed for deep-brain targets. Since our goal is cortical stimulation – which requires focusing close to the skull – a different transducer geometry is required. Previous work in FUS phased-array design is reviewed in Chapter 2.

5.2 Summary

Methods: Previous transducer designs reviewed in section 2.2 were used as a basis for the optimized design presented in this chapter. Simulations were used to optimize transducer geometry with respect to focus size, directivity, and secondary maxima (synonymous with grating lobes in FUS literature). Focus size and grating lobes during electronic steering were quantified using hydrophone measurements in water and a three-axis stage. A novel combination of optical tracking and acoustic mapping enabled measurement of the 3D pressure distribution in the cortical region of an ex vivo skull to within ~3.5 mm of the surface, and allowed accurate modelling of the experiment via non-homogeneous 3D acoustic

simulations.

Results: The new array is randomized with 128 elements 6.6 mm in diameter, radius of curvature 7.2 cm, opening diameter 10.3 cm (focal ratio 0.7), and 46% coverage, and center frequency 650 kHz. Hydrophone and simulation data demonstrate acoustic focusing beyond the skull bone, with the focus slightly broadened and shifted proximal to the skull, effects which could be compensated by phase aberration correction. The transducer design is an approximate midpoint among various tradeoffs in array directivity, size, acoustic power output, and cost.

5.3 Methods

The overall design objective was to develop an array capable of steering over the macaque somatosensory cortex (S1), with a focus small enough to modulate S1 in general, and possibly subregions associated with various neural circuits, such as face or hand stimulation. In adult macaques the S1 anatomical region is typically ~2 cm long, has a roughly 3 mm cross-section and is ~1 cm from the interior of the skull bone. Though the precise spatial relationship between the extent of an acoustic focus and regions of neural modulation is an open question, we used the S1 anatomical size to inform the desired focus size of our design, leading to design requirements that focus width should be less than 3 mm and length about 1 cm, to effectively target portions of S1 [159]. Beam shape, steering and grating lobes were evaluated with free-field Rayleigh-Sommerfeld simulations.

Given the success of recent spherical random arrays across in both transcranial and abdominal applications, and the established technique for their fabrication, we chose to pursue a sparse cap design to achieve our goal of selectively targeting the macaque S1 region. Our design problem was simplified by the choice of 650 kHz as the array center frequency, based on the frequency optimization work of

Clement, the success of 650 kHz in transcranial human studies, and that 650 kHz has been shown to modulate neurons [77], [105]. We fixed the element diameter to 6.6 mm to maintain a relatively low electrical impedance and high acoustic power output at 650 kHz.

5.3.1 Design Simulations

To optimize transducer geometry with respect to focus size and steering, we simulated a subset of the design variable space (radius of curvature, diameter, and coverage). The transducer shape used was a solid spherical cap with circular elements placed on the surface. Elements were randomly placed in each iteration, and were simulated using a superposition of 60 point sources per element conforming to the convexity of the spherical surface. Element sizes were fixed, and the number of elements was the largest number of 64, 96, 128, 160 that could fit onto the transducer in a given geometry without overlap and a minimum margin of 1 mm (i.e., an effective diameter of 7.6 mm). In addition to the transmit elements, four passive cavitation detectors (PCDs) 2.2 mm in diameter were inserted at fixed

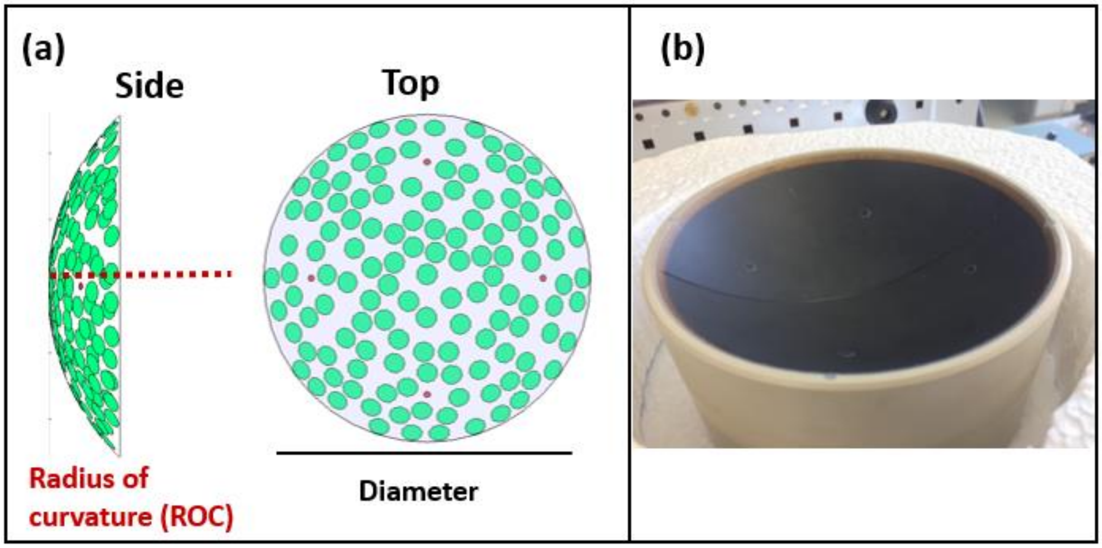

Figure 5.1 ***(a)*** *Setup of randomized spherical caps tested with simulations. ROC and diameter were varied with fixed element sizes. The green circles are the positions of the 128 transmit elements in their final arrangement. Red circles show the location of passive cavitation detectors.* ***(b)*** *Photo of the fabricated design.*

points, and random element placement was also constrained to avoid these. **Figure 5.1** shows the geometric setup used for simulations.

The effect of area coverage was evaluated independently to verify the general proposition that grating lobes decrease with increasing coverage. To study coverage, a specific geometry was chosen, the number of elements set to 128, and the element size was varied such that effective coverage ranged from 10% to 100%. The number of point sources approximating each element varied so that the density of point sources was roughly held constant, and element boundaries were allowed to overlap. This method, while not feasible to fabricate due to element overlap, allows evaluating coverage ratios above the packing limit, while also maintaining pseudo-randomization in point source placement. Without element overlap, for 128 randomly placed elements of 6.6 mm diameter 1 mm margin, the maximum coverage obtained was 49% in the geometries tested.

We implemented the Rayleigh-Sommerfeld integral in a GPU kernel using Nvidia's CUDA C++ API for all free field simulations. An Nvidia Quadro K620 with 384 cores and 2GB memory was used for all simulations. The homogenous-medium integral is an ideal use-case for massive parallelization, since there is no need for communication between threads, minimal conditional logic required, and each output voxel in the simulation grid can be computed independently of other voxels. One GPU thread was allocated for each voxel in the simulation grid. Within each thread, the contribution from all *N* point sources comprising the sub-sampled array elements (each point having an amplitude and phase represented as a complex number) was computed. Element positions, normal vectors, complex array amplitudes, and voxel positions were loaded into GPU constant memory, and one thread per output voxel was executed. Computation time was approximately 7 seconds per 280x280 slice, using 60 point sources per element.

The kernels were wrapped in a Python interface, and simulations were setup and run in Python, passing necessary parameters via NumPy arrays. Code and instructions to build the GPU library are available on Github (doi.org/10.5281/zenodo.1112442). The repository also contains functions to generate randomized arrays.

5.3.2 Fabrication

The chosen design was fabricated by Imasonic (Besancon, France) in two spherical sections with elements diced out of piezocomposite material. Image Guided Therapy (Pessac, France) built the electronic generators that power the transducer, and 650 kHz electrical impedance matching (Pi low-pass L-C network). The entire system is MR compatible. The transducer plus cable had an electrical impedance 170 + *j* 900 Ω (magnitude 916 Ω), and was matched to 50 Ω generator output (Ω = 1 ohm).

5.3.3 Output

A three-axis motion stage was used to translate a hydrophone for mapping acoustic output. Output at low power was measured using a needle hydrophone (HNC-400, Onda Corporation), and an optical hydrophone (Precision Acoustics Ltd, Dorchester, UK) at high power. With the needle hydrophone, beam maps and steering profiles were collected. The beam was electronically steered in 10 mm steps in both the transverse and axial directions in order to quantify grating lobe levels. Peak pressures at the focus were collected with the optical hydrophone as power was increased to 100% output. Hydrophone signals were digitized and recorded with a programmable oscilloscope controlled via Python.

5.3.4 Transcranial FUS

To evaluate a transcranial sonication, beam maps in a cortical region behind an *ex vivo* skull piece were collected using a novel approach. The method described below uses hydrophone tracking developed in Chapter 4, with the added complexity of co-registering a CT of the skull piece to the motor axes for path planning. Prior to measurement, the skull was placed in degassed water under a vacuum for 24 hours. Because of skull attenuation and the generally lower pressures used for neuromodulation, measuring acoustic fields behind the skull is best with the sensitivity of a needle hydrophone. However the needle tip is susceptible to damage, making it a challenge to safely navigate the hydrophone in close proximity to the skull (ie. the cortical region we wish to stimulate).

To solve this problem, we used a combination of optical tracking and image registration. First, a CT of the skull piece was collected (vivaCT 80 Scanco Medical, Switzerland). The skull piece was then rigidly mounted to a water tank several centimeters from the transducer face. An NDI Polaris optical tracking system was used with a tracked probe to collect fiducial points, based on landmarks visible on the skull and in the CT image. This yielded a physical-to-image transform with fiducial registration error (FRE) of 2.3 mm. A brass replica of the hydrophone was then mounted to a custom adapter with a rigid-body tracker. A standard pivot calibration was performed to measure the tip offset (RMSE=0.4 mm). Finally, the tracked hydrophone was mounted to the 3-axis stage and translated over a range of grid points, with the optical tracker recording the tip position at each point. A second rigid registration was performed yielding a transform between motor coordinates and optically tracked coordinates (FRE=0.3 mm). Combining this with the tip offset and the physical-to-image transform yielded a chain of transforms from the motor coordinates of the hydrophone tip into the CT image. This was then used to plan a 3D beam mapping trajectory in a cortical area of the skull piece. Combining the above errors yields a fiducial registration error of 2.4 mm. Though this is an underestimate of the true target registration error, it gives some sense of the error scale involved [127]. An additional safety margin from the skull interior was therefore applied to trajectory planning. The resulting trajectory had an apparent closest approach of about 3.5 mm to account for registration and tracking uncertainty.

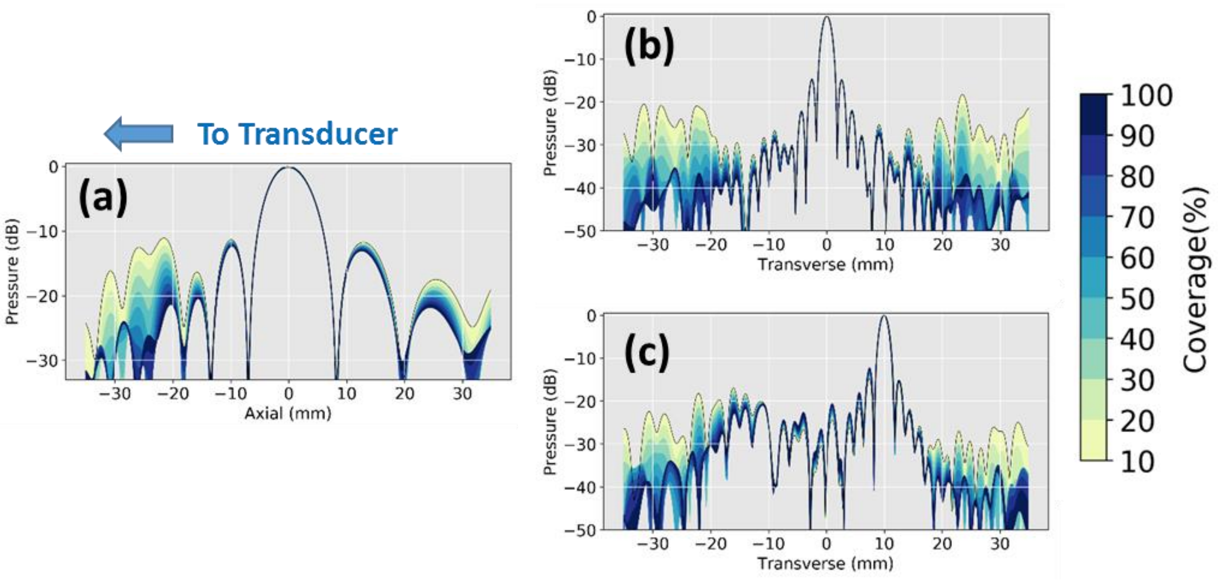

Figure 5.2 *Simulated effect of array coverage on grating lobe levels. Coverage % indicates the fraction of cap area that is occupied by active transmit area.* ***(a)*** *Beam profile along the sonication axis.* ***(b)*** *Transverse profile in the focal plane.* ***(c)*** *Same profile as (b), but when the focus is steered 1 cm off-axis. These simulations used the final design geometry, ROC=72 mm, diameter=103 mm, 128 elements, but element sizes were varied and allowed to overlap. The fabricated design has a coverage fraction of 46%.*

The optical tracking system was used in a final step to collect surface points on the interior spherical face of the transducer. These points were used in a least-squares fit to localize the transducer's geometric center within optically-tracked coordinates, and using the transform chain, project transducer elements into the coordinate system of the 3-axis stage. This Cartesian coordinate system was then used to define a 3D simulation grid. Elements were placed in the simulation grid along with the registered CT scan, and simulated using k-Wave [19]. Sound speed, density, and attenuation were linearly mapped from CT Hounsfield units, similar to the procedure in Marquet *et al.* [122]. The registration did not provide information about alignment and the azimuthal rotation of the transducer about its axis, and simulation setup assumed the sonication axis was parallel to the x-axis and used an arbitrary azimuthal rotation.

5.4 Results

5.4.1 Array coverage percentage and steering

Simulations of array coverage at the final spherical geometry demonstrate, for the non-steered case, a uniform downward trend in grating lobe and side lobe levels as coverage/density increases from 10% to 100% (**Figure 5.2**). Color contours correspond to array density. Secondary lobe height decreased with higher array coverage along the axial and transverse profiles (**Figure 5.2a and 5.2b**). Conversely, inter-lobe minima trend to higher pressures with increasing array coverage, demonstrating that larger elements lead to more diffuse acoustic output in peripheral lobe regions. Relative variability due to

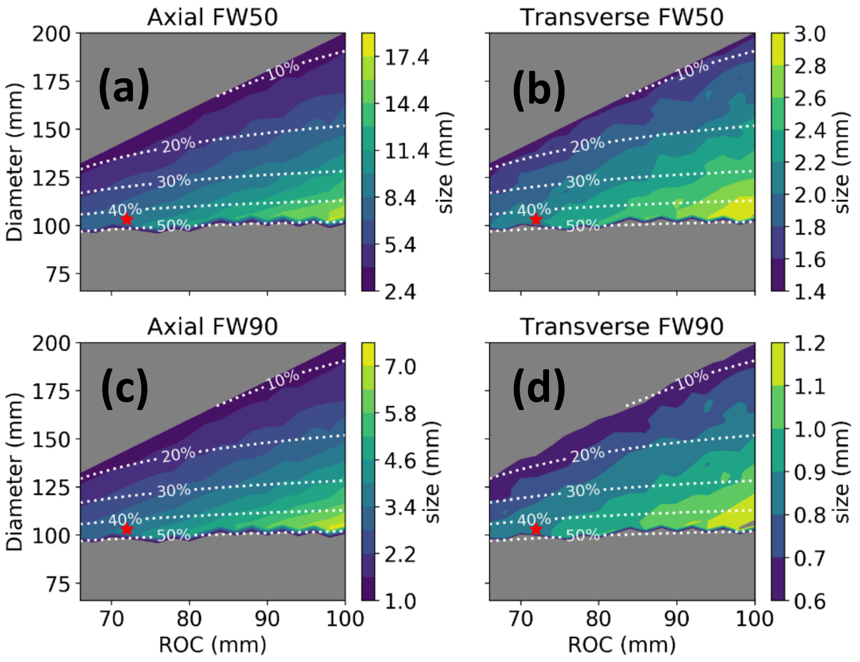

Figure 5.3 Size of the natural focus as a function of spherical geometry, using Rayleigh-Sommerfeld pressure. ***(a)-(b):*** *Full-width half max (FW50).* ***(c)-(d):*** *Full-width at 90% max (FW90).* ***Left column****: size along an axial profile.* ***Right column****: size along profile in focal plane. Color contours indicate size in each direction. They are diagonally oriented along lines of constant focal ratio (ROC / Diameter), with fluctuations due to randomization of array elements. White contours show the array coverage percent, which is determined by fitting the largest number of elements onto the cap with the stated non-overlap and PCD-avoidance constrains. A red star indicates the chosen design. ROC = Radius of curvature.*

changing array density decreases towards the central maximum. When the beam is steered off-axis (**Figure 5.2c**), some maxima see the trend reverse, becoming higher with increasing array density. These results are consistent with previously cited studies about the effects of array density and directivity on grating lobes and steering.

The influence of spherical geometry on focus size can be seen in **Figure 5.3**, which shows the full-width at 50% and 90% of the pressure maximum (FW50 and FW90, respectively) in the axial and transverse directions. It can be seen from the diagonally oriented contour lines in these figures that--at a fixed frequency and element size--focal size is correlated with f-number (focal length divided by diameter of aperture). Array coverage contours are overlaid, based on the maximum number of elements that fit onto the cap within the stated constraints. We chose a design that produced a small focus, has a convenient focal length with respect to macaque head size, and had nearly the maximum coverage achievable. The chosen design is denoted with a red star and achieves a balance of focus size and area coverage.

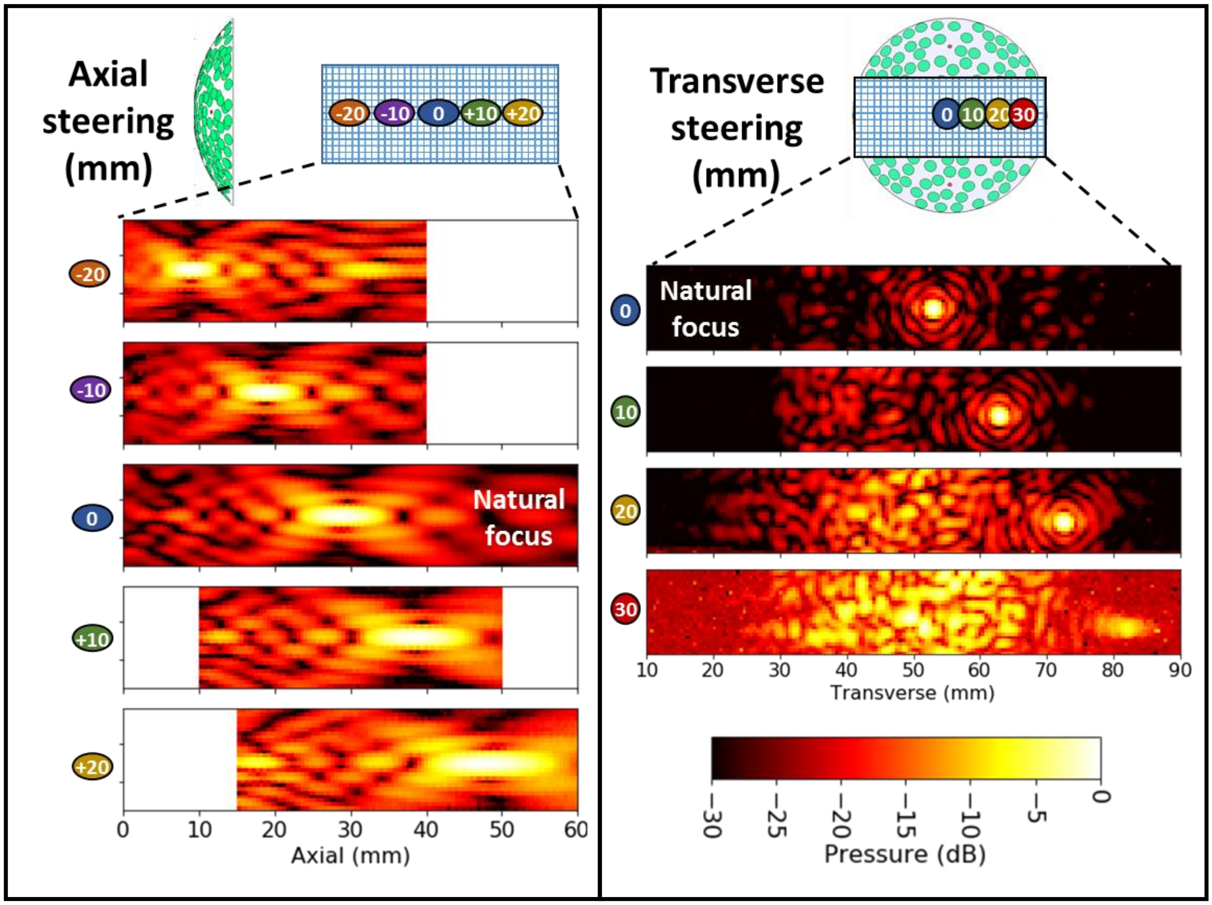

Figure 5.4 *Hydrophone beam maps and grating lobes as the focus is electronically steered.* ***Left:*** *steering in 10 mm increments along the sonication axis, from -20 to +20 mm.* ***Right****: steering in the focal plane up to +30 mm. Focus degradation occurs rapidly when steering off-axis.*

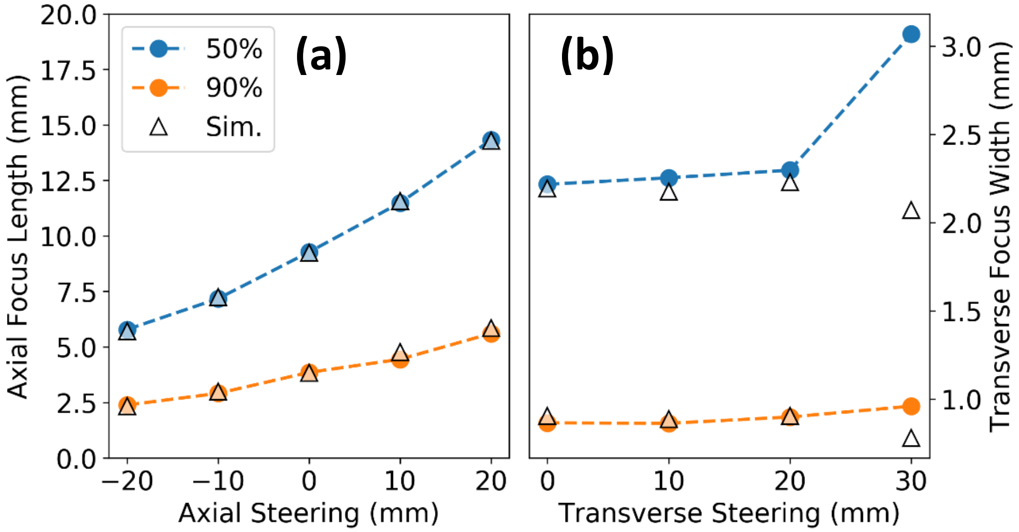

Figure 5.6 *Dimensions of the pressure focus measured with needle hydrophone data from Figure 5.4 as the focus is electronically steered.* ***(a)*** *Axial steering.* ***(b)*** *Transverse steering. '50%' is the full-width half max in each direction. '90%' is the full-width at 0.9 of the max. Triangles show corresponding values from simulated pressure.*

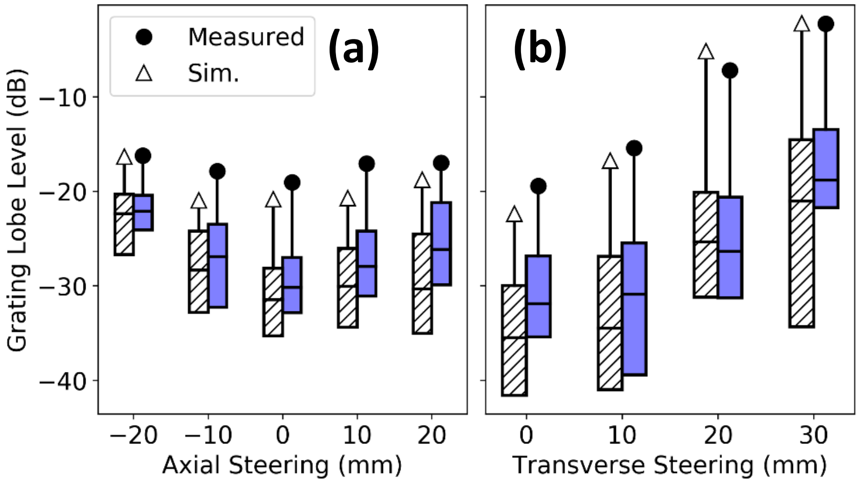

Figure 5.5 *Distributions of grating lobe levels during electronic steering from simulated pressure fields (hatched) and measured hydrophone data in Figure* ***5****.4 (solid fill). The boxes represent 25th, 50th, 75th percentiles, and the max. Pressures are relative to the steered focus in each case. Distributions exclude the region immediately around the focus and first lobe.* ***(a)*** *Axial steering* ***(b)*** *Transverse steering.*

5.4.2 Output measurements

The chosen design is spherically focused with radius of curvature 72 mm and 103 mm diameter at the opening face (f-number 0.7), and a coverage fraction of 46%. The focus size has full-width at half maximum (same as FW50) of 9.3 mm and 2.2 mm in the axial and lateral directions, respectively. Linear simulations were in good agreement with the low-power hydrophone field measurements.

Focal pressure, width, and grating lobe levels in the presence of steering were measured in 10 mm steering increments (**Figure 5.4**). With no steering, the axial grating lobes peaked at –19 dB, while the first side lobe surrounding the focus peaked at –9.7 dB. Beam maps collected in the axial plane show no significant pre- or post-focal maxima up to 20 mm steering, while steering in the focal plane show focus degradation and grating lobes appearing off-axis. **Figure 5.5** plots the distribution of maxima, excluding the focus and first sidelobe. The largest lobe level with axial steering was -15 dB at -20 mm. Transverse steering beyond 10 mm exceeded this level. Based on these data we estimate that neuromodulation pulses can be steered within an ellipse +/- 20 mm around the focus in the axial direction, and +/- 10 mm in the transverse direction, in which the peak free-field grating lobe is -15 dB. **Figure 5.6** shows focal dimensions in axial and transverse directions, as the beam is steered around the focus.

Power calibration with the transducer plus matching network resulted in linear pressure output in neuromodulation pressure range, measured waveforms <1MPa at the focus were narrow-band after a short ramp-up. Examples are shown in **Figure 5.7**. The recorded waveform at low pressure for a 30-cycle pulse had a –6 dB bandwidth of 50 kHz (**Figure 5.7b**). Matching circuit alone was narrow band (~40 kHz) at 650 kHz (IGT, private communication). Pressure output at the maximum input amplitude tested was 12.5 MPa / 8 MPa peak positive / negative (**Figure 5.7c**).

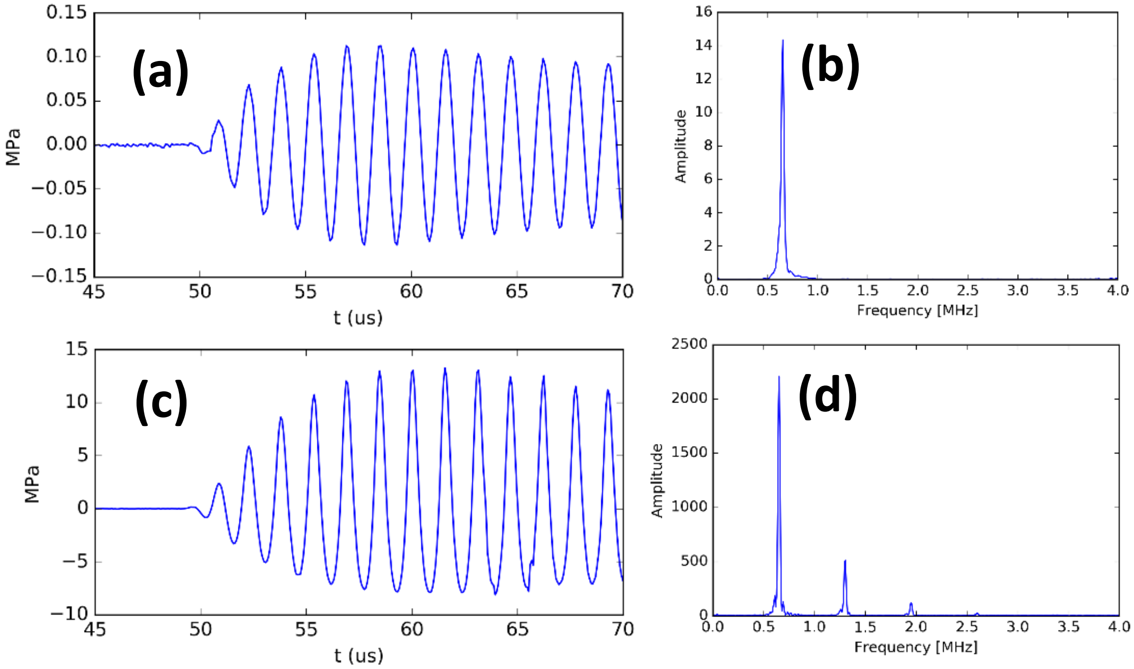

Figure 5.7 *Waveforms and spectra measured at the focus.* ***(a)-(b)*** *Needle hydrophone data when driving at 1% amplifier voltage.* ***(c)-(d)*** *Optical hydrophone data at the maximum amplitude tested (80% amplifier voltage).*

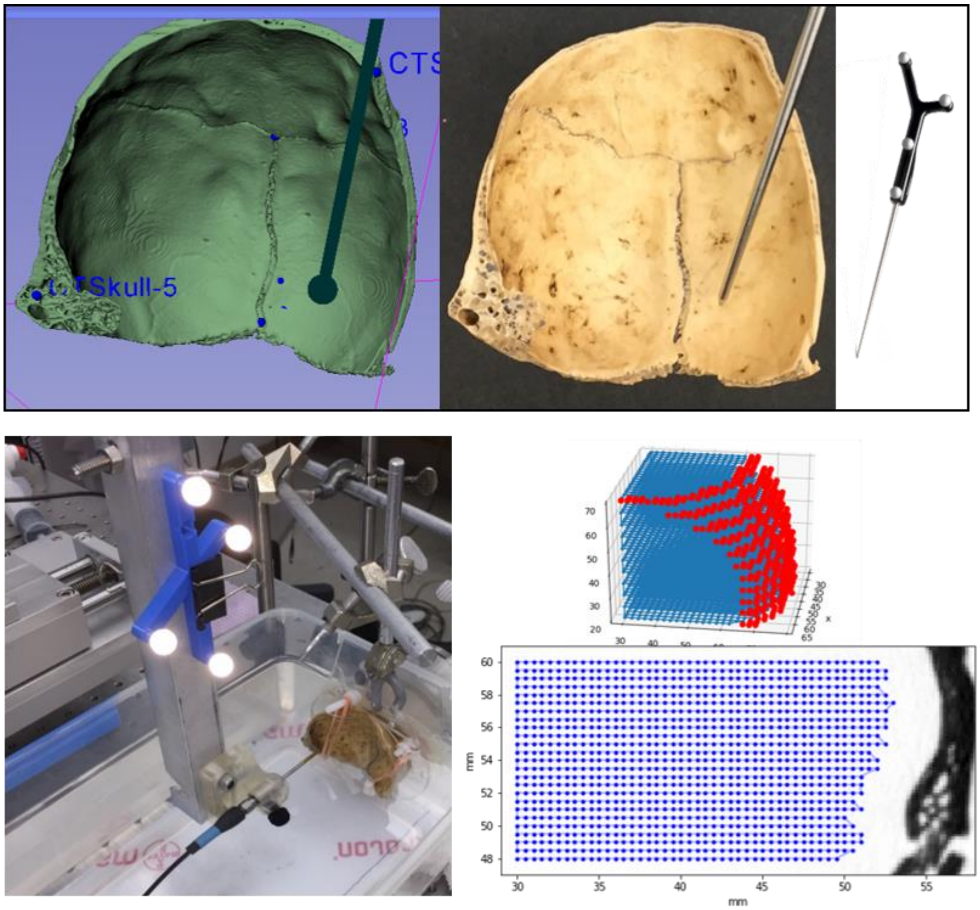

__Figure 5.8__ Steps involved in guiding the hydrophone tip along the interior of the skull piece using a three-axis stage. Steps include CT-to-physical registration, finding the hydrophone tip offset, physical-to-motor registration, and finally path planning with the projected CT scan. An example hydrophone trajectory is shown on the lower right.

5.4.3 Transcranial Evaluation

Figure 5.8 depicts the setup for transcranial beam mapping, image registration, motor trajectory planning. A map of pressure was collected for the transcranial case, and the corresponding free-field maps were collected by simply removing the skull piece. This is similar to the methods presented in Chapter 4, but with added complexity of registration between motor coordinates and the skull CT for motor planning. An axial slice through the focus is shown in **Figure 5.9**. The spatial distribution of peak pressure in the non-homogeneous k-Wave simulations was qualitatively similar. Transcranial beam measurements behind a sample skull showed focal broadening to FW50 of 11.5 and 2.7 mm compared

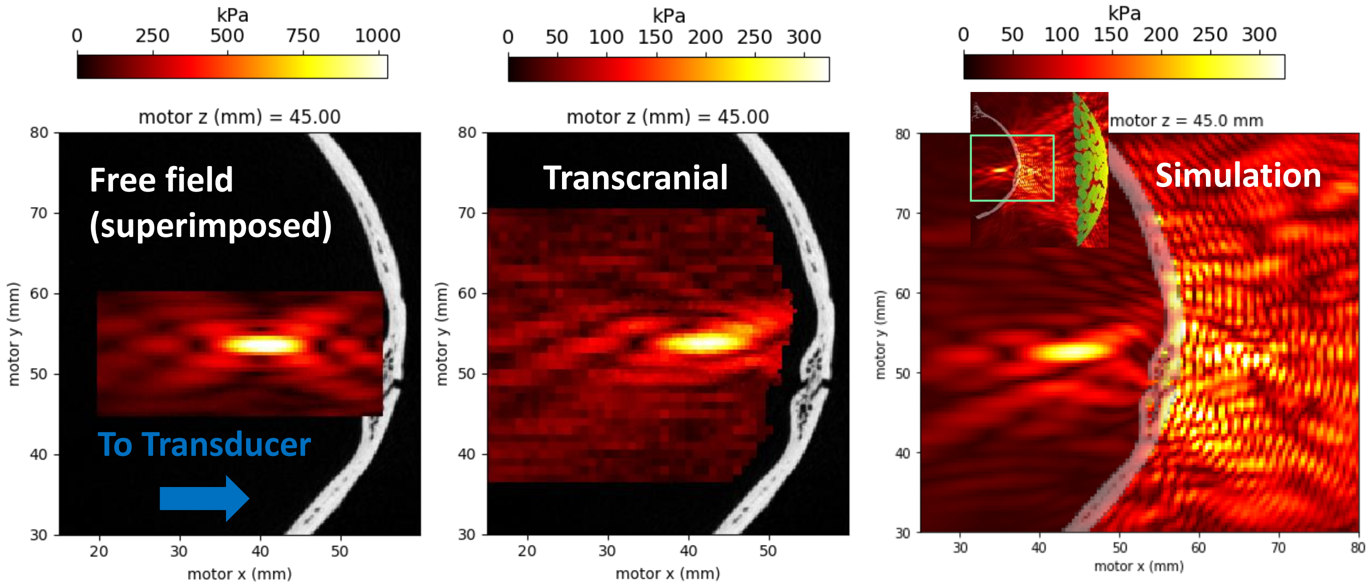

*Figure 5.9 Pressure maps in a focal plane slice of the 3D hydrophone collection using the optical tracking setup, showing the free field scan with no skull piece **(left)** and the corresponding scan behind an ex-vivo skull without aberration correction **(center)**. The skull CT was co-registered into motor coordinates and overlaid by interpolating image voxels into the transformed motor frame. For transcranial mapping, a large volume motor scan was collected first with 1 mm voxel sides, followed by a smaller high-resolution region around the focus with 0.5mm voxels. The location of the transducer along the sonication axis (approximated to be the motor -x direction) was recorded and used for the K-wave simulation shown **(right)**. Actual azimuthal rotation of the transducer, off-axis alignment, and skull parameters were not known for the simulation.*

to 9.3 mm and 2.2 mm in free field (axial and lateral), a 1.5 mm shift of the focus in the axial direction towards the transducer, and peak amplitude 28% of the free-field case **(Figure 5.10)**. Both the focal broadening and proximal shift are expected. Acoustic transparency of this skull piece at 650 kHz agreed with expectation, though it is not necessarily representative of biological variability encountered in live subjects.

5.5 Discussion

5.5.1 Transducer Design

Using simulations and knowledge gained from prior work, we designed a new randomized, relatively sparse (45%), spherical array to stimulate the S1 cortex in macaque monkeys. The size and steering constraints for our application relate directly to the geometry and distribution of elements on the transducer array. Our main design objectives were to have a small focus size, low grating lobe levels, ROC appropriate for macaques, and focal steering capability. These design factors were briefly summarized, based on previous work from both volumetric imaging and therapy. In general, focus size and grating lobes are much smaller for arrays with spherical vs. flat construction geometry, but focus degradation with off-axis steering is worse with spherical arrays. Element size and number also influence focus size and steering--a larger number of smaller elements results in focus broadening towards the transducer [104]. However, having more elements gives a higher degree of freedom and thus better performance for electronic steering and multi-focusing. For a given transducer geometry, grating lobe levels are further modified by the arrangement or spatial distribution of elements. Geometry, element size, count, and arrangement are design variables that must be chosen based on application needs. We recommend future transcranial studies report transducer focal ratio (or diameter), element size, and array sparsity in addition to ROC.

5.5.2 Transducer Output

The transducer and impedance matching network were optimized for electrical driving at 650 kHz. Other resonance frequencies were not examined but are not expected to give output of comparable quality, since piezocomposite materials have a single dominant resonance and weaker non-harmonic spurious resonances [168]. Driving the transducer at other frequencies would result in poor conversion to acoustic power, though perhaps still feasible for the low pressure, low duty-cycle pulses used in neuromodulation.

5.5.3 Transcranial Performance

A sample ex vivo skull section was used to examine skull attenuation and aberration effects on the beam at 650 kHz, using a novel approach combining optical tracking, image registration, and beam mapping. The results agree with expectation that the focus is slightly aberrated and shifted toward the transducer. Aberration correction can mostly correct for distortion and shift, but was not implemented in the present study. For example, using a hydrophone positioned in a deep-brain region behind *ex vivo* human skulls, Marquet showed an average 0.32 mm shift of the focus was recoverable using simulation-based time reversal [122]. A later MR-guided study, after applying a similar simulation-based time reversal correction for skull phase aberrations, showed average targeting accuracy in human heads of ~1 mm, below thermometry voxel resolution [9]. The larger shift (1.5 mm) observed in our experiment is a result of difference in skull thickness and geometry, and transducer focal ratio (focal ratio was not reported in the cited studies, but the figures suggest smaller f was used). Spherical transducers with smaller focal ratio (down to f=0.5, a full hemisphere) would likely see smaller transcranial spatial shift and greater

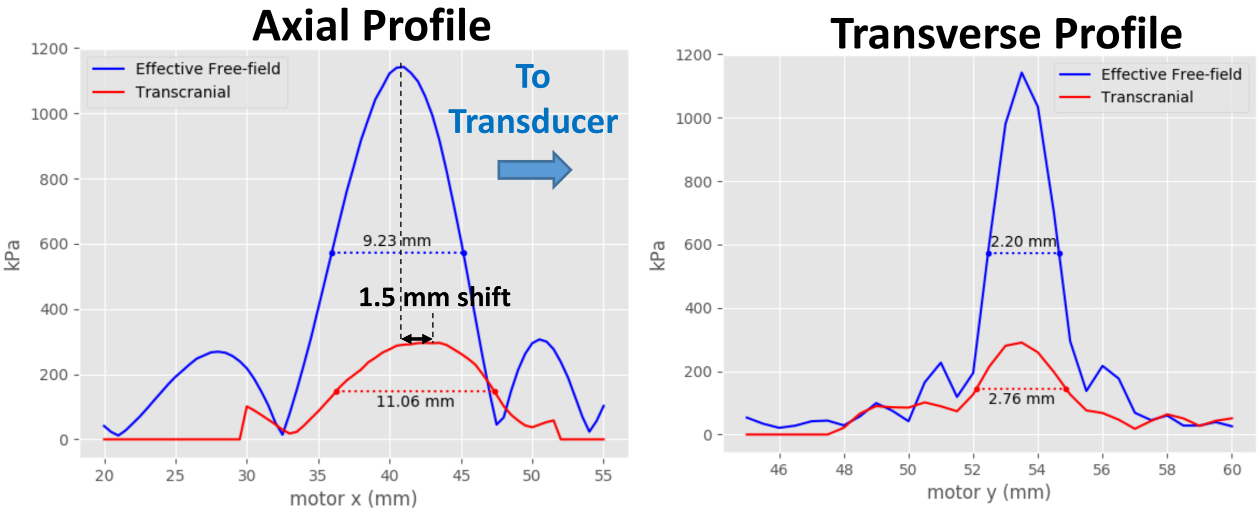

***Figure 5.10** Comparison between free-field focus and transcranial focus along the sonication axis **(left)** and in the focal plane **(right)** from hydrophone beam maps. The focus is shifted in the direction of the skull and transducer due to the increased sound speed in the skull, and broadened from phase aberration. Transverse profiles shown on the right coincide with axial focal maxima in both cases. The transcranial pressure was 28% of free-field due to reflection and attenuation by the skull piece.*

relative broadening of the focus due to aberration from a broad incidence cone. Thus, reporting focal ratio or transducer diameter helps when comparing transcranial focusing across different devices.

There are numerous additional details that were not examined which are important with *in vivo* sonication. For example, the obliquity of the acoustic axis with respect to skull geometry can refract the beam and produce warped focal regions [107]. Heating and attenuation through multiple tissue layers are also significant concerns with transcranial FUS, both because of accumulated thermal dose and beam distortion that is detrimental to targeting [169]. Attenuation due to muscle layers that surround the skull in macaques was not measured, but is not expected to be a significant risk due to the low pressure involved in neuromodulation. In our experience *in vivo* experiments using a single-element transducer with focal ratio f=1.0 have shown little risk of skin burn at pressures used for neuromodulation.

Sonication frequency was not considered as a variable, since prior work had identified 650 kHz as a safe and effective frequency for transcranial sonication for transcranial thermal lesioning, where higher frequencies are generally preferred because of increased energy absorption [105]. While it has been shown that 650 kHz can stimulate neurons, the exact mechanism has yet to be discovered, and a lower frequency may prove more effective [77], [170]. Related, it is not known precisely how the spatial distribution of pressure maps onto the location of modulated neurons. For example, the FWHM contour may not be a meaningful indicator of the modulation threshold. In a study of neuromodulation in a rat where FDG uptake was measured as an indicator for brain activity, the location of FDG-PET signal increase coincided with the estimated 90% contour of the FUS spatial peak, suggesting a threshold-based phenomenon that could be potentially be tuned with specific acoustic intensity profiles [90]. Functional and *in vitro* studies in the future will be required to resolve this question.

5.6 Conclusions

In this study, we designed and characterized a new randomized, spherically-focused array transducer for transcranial FUS in non-human primates. The transducer and generator system are MR compatible and capable of a large range of pressure output. The focus can be steered over the range of the non-human primate somatosensory cortex and a focal beam can be maintained transcranially. This MR-compatible system will be employed for combined FUS neuromodulation and functional imaging studies.

CHAPTER 6CONCLUSIONS

6.1 Original Contributions

This work has developed three novel techniques related to overarching goals of non-invasiveness, precision and selectivity image-guided FUS. Cavitation imaging and MR thermometry were used to tune mild hyperthermia to sub-cavitation levels. Optical tracking in registered images was used to accurately predict the focus and gradient alignment for MR ARFI. A new device was optimized for cortical targeting and demonstrated agreement with simulations. The tools developed in this work are facilitating further preclinical research in focused ultrasound.

Multi-focal HIFU can be used in the future in conjunction with feedback control to perform mild hyperthermia treatments with less probability of cavitation. In Chapter 3, multi-focal HIFU was used to achieve mild temperature elevation with reduced cavitation activity. Cavitation activity was monitored using the variance and PAM on two transducers. PAM was able to resolve multiple foci in the phantoms and image magnitude was highly correlated with channel variance in both pork and phantoms, leading to novel images of multi-focal distributed cavitation sources.

With both hypothesized direct neuromodulation and mediated BBB-opening, the ability to spatially pinpoint the location of desired effects makes FUS a unique probe for both understanding the brain, and potentially addressing localized pathologies. The work in Chapters 4-5 created two new tools that enable accurate targeting of FUS as a non-invasive neurological probe. Initial *in vitro* and *in vivo* experiments detailed there have validated their performance, and the door is open for future discoveries. In particular, the degree to which modulation of neural circuits is a genuine phenomenon that can be reliably controlled, and the impact this has on understanding functional networks are topics of continued debate.

6.2 Future Directions

6.2.1 Feedback controlled multi-focusing

In Chapter 3 multi-focal HIFU was introduced as a means to achieve mild hyperthermia with reduced probability of cavitation. Potential clinical and preclinical applications were discussed, such as non-mechanical modulation of biological processes like anti-tumor immune stimulation, and thermally activated drug carriers. A correlation between beam broadening and cavitation was observed for each input power tested, and this provides a potential “tuning knob” that can be used to regulate cavitation in volumetric mild hyperthermia. Previous work has shown that amplitude can be used to regulate cavitation with a PID feedback controller monitoring cavitation echoes [88], [150]. A similar controller could instead be used to de-focus or broaden the beam, rather than simply reduce its amplitude, in response to cavitation or large peak temperature (if used with MR thermometry).

6.2.2 Real-time transcranial beam prediction

The real-time beam projection is a technique with great practical potential in both research and clinical settings, and a natural next step would be take this system and develop a method for predicting skull diffraction and aberration in real time. Indeed, in the ARFI imaging experiments reported in Chapter 4, no displacement was observed in the opening trial of animal two. After repositioning the transducer to have a less oblique incidence, focal displacement was measured. The likely explanation is critical angle reflection off the skull bone, preventing transmission into the brain. A method that could predict this situation during treatment, and less severe focal distortions, would have value in transcranial targeting.

To that end, several potential approaches utilizing deep learning have been identified and are in early development stages, though none were presented in this dissertation. They include accelerated numerical approximation methods imported from other fields. For example, one group in computational fluid dynamics has developed a deep learning network for solving the Navier-Stokes equation in a turbulent convective flow [171]. Another group has outlined an early approach for real-time estimation of convective flows in Eulerian fluids [172]. The degree to which these techniques can be applied to acoustics is unclear, though similarity in the fundamental governing equations suggests it is a promising method in some regime of acoustics. Purely empirical, non-physics based approaches from image prediction may also provide insights into successful convolutional neural network architecture [173].

6.2.3 *Ex vivo* skull assessment using the cortical mapping technique

The tracked hydrophone technique used for cortical mapping in Chapter 5 is a useful tool for understanding how different transducers and steering schemes can be used in the cortex. Additionally, the tool can be useful for validating acoustic models and parameters, which tend to be most sensitive near boundaries. The ability to measure fields within 3-4 mm of the skull may be provide a new ability to characterize mode viscoelastic mode conversion between longitudinal and shear waves, a growing area of interest in transcranial acoustics [174].

6.2.4 Phased-array aberration correction

Phase aberration correction with the new transducer needs to be implemented for cortical macaque targets. Correction in deep brain targets has been performed in simulations, with hydrophones 40-50 mm from *ex vivo* skull surfaces, and with MR-ARFI displacement maximization in phantoms, animals, and cadaver heads [7], [119], [166], [175]. These methods, while proven, tend to be slow, and new techniques are in development which accelerate finding optimal array encoding for phase aberration correction.

BIBLIOGRAPHY

[1] K. Hynynen, A. Darkazanli, E. Unger, and J. F. Schenck, “MRI-guided noninvasive ultrasound surgery,” *Med. Phys.*, vol. 20, no. 1, pp. 107–115, Jan. 1993.

[2] H. Wain, P. Vanbaren, S. Member, E. S. Ebbini, and C. A. Cain, “Ultrasound Surgery : Comparison of Strategies Using Phased Array Systerns,” vol. 43, no. 6, pp. 1085–1098, 1996.

[3] J. L. Mestas, R. A. Fowler, T. J. Evjen, L. Somaglino, A. Moussatov, J. Ngo, S. Chesnais, S. Rognvaldsson, S. L. Fossheim, E. A. Nilssen, and C. Lafon, “Therapeutic efficacy of the combination of doxorubicin-loaded liposomes with inertial cavitation generated by confocal ultrasound in AT2 Dunning rat tumour model,” *J Drug Target*, vol. 22, no. 8, pp. 688–697, 2014.

[4] G. ter Haar and C. Coussios, “High intensity focused ultrasound: Physical principles and devices,” *Int. J. Hyperth.*, vol. 23, no. 2, pp. 89–104, Jan. 2007.

[5] J. Unga and M. Hashida, “Ultrasound induced cancer immunotherapy,” *Adv. Drug Deliv. Rev.*, vol. 72, pp. 144–153, Jun. 2014.

[6] Z. Hu, X. Y. Yang, Y. Liu, M. a. Morse, H. K. Lyerly, T. M. Clay, and P. Zhong, “Investigation of HIFU-induced anti-tumor immunity in a murine tumor model,” *AIP Conf. Proc.*, vol. 829, pp. 241–245, 2006.

[7] B. Larrat, M. Pernot, G. Montaldo, M. Fink, and M. Tanter, “MR-guided adaptive focusing of ultrasound,” *IEEE Trans. Ultrason. Ferroelectr. Freq. Control*, vol. 57, no. 8, pp. 1734–1747, 2010.

[8] P. Gélat, G. ter Haar, and N. Saffari, “Towards the optimisation of acoustic fields for ablative therapies of tumours in the upper abdomen,” *J. Phys. Conf. Ser.*, vol. 457, p. 12002, 2013.

[9] D. Chauvet, L. Marsac, M. Pernot, A.-L. Boch, R. Guillevin, N. Salameh, L. Souris, L. Darrasse, M. Fink, M. Tanter, and J.-F. Aubry, “Targeting accuracy of transcranial magnetic resonance–guided high-intensity focused ultrasound brain therapy: a fresh cadaver model,” *J. Neurosurg.*, vol. 118, no. 5, pp. 1046–1052, May 2013.

[10] N. P. K. Ellens, I. Kobelevskiy, A. Chau, A. C. Waspe, R. M. Staruch, R. Chopra, and K. Hynynen, “The targeting accuracy of a preclinical MRI-guided focused ultrasound system,” *Med. Phys.*, vol. 42, no. 1, pp. 430–439, 2015.

[11] R. L. King, J. R. Brown, and K. B. Pauly, “Localization of Ultrasound-Induced In Vivo Neurostimulation in the Mouse Model,” *Ultrasound Med. Biol.*, vol. 40, no. 7, pp. 1512–1522, 2014.

[12] H. Baek, K. J. Pahk, and H. Kim, “A review of low-intensity focused ultrasound for neuromodulation,” *Biomedical Engineering Letters*, vol. 7, no. 2. 2017.

[13] W. J. Elias, N. Lipsman, W. G. Ondo, P. Ghanouni, Y. G. Kim, W. Lee, M. Schwartz, K. Hynynen, A. M. Lozano, B. B. Shah, D. Huss, R. F. Dallapiazza, R. Gwinn, J. Witt, S. Ro, H. M. Eisenberg, P. S. Fishman, D. Gandhi, C. H. Halpern, R. Chuang, K. Butts Pauly, T. S. Tierney, M. T. Hayes, G. R. Cosgrove, T. Yamaguchi, K. Abe, T. Taira, and J. W. Chang, “A Randomized Trial of Focused Ultrasound Thalamotomy for Essential Tremor,” *N. Engl. J. Med.*, vol. 375, no. 8, pp. 730–739, 2016.

[14] H. Ruhnke, T. Eckey, M. K. Bohlmann, M. P. Beldoch, A. Neumann, A. Agic, J. Hägele, K. Diedrich, J. Barkhausen, and P. Hunold, “MR-guided HIFU treatment of symptomatic uterine fibroids using novel feedback-regulated volumetric ablation: Effectiveness and clinical practice,” *Fortschr Rontgenstr*, vol. 185, no. 10, pp. 983–991, 2013.

[15] J. D. Jackson, *Classical Electrodynamics, 3rd Edition*. Wiley; 3 edition (August 10, 1998), 1998.

[16] W. D. O’Brien, “Ultrasound-biophysics mechanisms.,” *Prog. Biophys. Mol. Biol.*, vol. 93, no. 1–3, pp. 212–55, 2007.

[17] A. Partanen, M. Tillander, P. S. Yarmolenko, B. J. Wood, M. R. Dreher, and M. O. Kohler, “Reduction of peak acoustic pressure and shaping of heated region by use of multifoci sonications in MR-guided high-intensity focused ultrasound mediated mild hyperthermia.,” *Med. Phys.*, vol. 40, no. 1, pp. 13301-1-13301–13, Jan. 2013.

[18] J. Gu and Y. Jing, “Modeling of wave propagation for medical ultrasound: A review,” *IEEE Trans. Ultrason. Ferroelectr. Freq. Control*, vol. 62, no. 11, pp. 1979–1993, 2015.

[19] B. E. Treeby, J. Jaros, A. P. Rendell, and B. T. Cox, “Modeling nonlinear ultrasound propagation in heterogeneous media with power law absorption using a k-space pseudospectral method.,” *J. Acoust. Soc. Am.*, vol. 131, no. 6, pp. 4324–36, Jun. 2012.

[20] N. Ellens, A. Pulkkinen, J. Song, and K. Hynynen, “The utility of sparse 2D fully electronically steerable focused ultrasound phased arrays for thermal surgery: a simulation study,” *Phys. Med. Biol.*, vol. 56, no. 15, pp. 4913–4932, 2011.

[21] R. Salomir, J. Palussire, F. C. Vimeux, J. a. De Zwart, B. Quesson, M. Gauchet, P. Lelong, J. Pergrale, N. Grenier, and C. T. W. Moonen, “Local hyperthermia with MR-guided focused ultrasound: Spiral trajectory of the focal point optimized for temperature uniformity in the target region,” *J. Magn. Reson. Imaging*, vol. 12, no. 4, pp. 571–583, 2000.

[22] T.-C. Shih, P. Yuan, W.-L. Lin, and H.-S. Kou, “Analytical analysis of the Pennes bioheat transfer equation with sinusoidal heat flux condition on skin surface.,” *Med. Eng. Phys.*, vol. 29, no. 9, pp. 946–53, Nov. 2007.

[23] J. G. Lynn and T. J. Putnam, “Histology of Cerebral Lesions Produced by Focused Ultrasound.,” *Am. J. Pathol.*, vol. 20, no. 3, pp. 637–49, 1944.

[24] W. J. Fry, W. H. Mosberg, J. W. Barnard, and F. J. Fry, “Production of focal destructive lesions in the central nervous system with ultrasound.,” *J. Neurosurg.*, vol. 11, no. 119, pp. 471–478, 1954.

[25] J. E. Kennedy, G. R. ter Haar, and D. Cranston, “High intensity focused ultrasound: surgery of the future?,” *Br. J. Radiol.*, vol. 76, no. 909, pp. 590–599, Sep. 2003.

[26] N. McDannold, “Quantitative MRI-based temperature mapping based on the proton resonant frequency shift: review of validation studies.,” *Int. J. Hyperthermia*, vol. 21, no. September, pp. 533–546, 2005.

[27] B. Quesson, F. Vimeux, R. Salomir, J. a. De Zwart, and C. T. W. Moonen, “Automatic control of hyperthermic therapy based on real-time fourier analysis of MR temperature maps,” *Magn. Reson. Med.*, vol. 47, no. 6, pp. 1065–1072, 2002.

[28] G. T. Clement, P. J. White, R. L. King, N. McDannold, and K. Hynynen, “A magnetic resonance imaging-compatible, large-scale array for trans-skull ultrasound surgery and therapy.,” *J. Ultrasound Med.*, vol. 24, pp. 1117–1125, 2005.

[29] K. Hynynen, G. T. Clement, N. McDannold, N. Vykhodtseva, R. King, P. J. White, S. Vitek, and F. A. Jolesz, “500-Element ultrasound phased array system for noninvasive focal surgery of the brain: A preliminary rabbit study with ex vivo human skulls,” *Magn. Reson. Med.*, vol. 52, no. 1, pp. 100–107, 2004.

[30] J. W. Hand, A. Shaw, N. Sadhoo, S. Rajagopal, R. J. Dickinson, and L. R. Gavrilov, “A random phased array device for delivery of high intensity focused ultrasound,” *Phys. Med. Biol.*, vol. 54, no. 19, pp. 5675–5693, 2009.

[31] L. J. Savic, M. De Lin, R. Duran, R. E. Schernthaner, B. Hamm, J.-F. Geschwind, K. Hong, and J. Chapiro, “Three-Dimensional Quantitative Assessment of Lesion Response to MR-guided High-Intensity Focused Ultrasound Treatment of Uterine Fibroids,” *Acad. Radiol.*, no. 1, 2015.

[32] S. Ellis, V. Rieke, M. Kohi, and A. C. Westphalen, “Clinical applications for magnetic resonance guided high intensity focused ultrasound (MRgHIFU): Present and future,” *J. Med. Imaging Radiat. Oncol.*, vol. 57, no. 4, pp. 391–399, 2013.

[33] J. E. Kennedy, “High-intensity focused ultrasound in the treatment of solid tumours.,” *Nat. Rev. Cancer*, vol. 5, no. 4, pp. 321–7, 2005.

[34] L. Zhang, H. Zhu, C. Jin, K. Zhou, K. Li, H. Su, W. Chen, J. Bai, and Z. Wang, “High-intensity focused ultrasound (HIFU): effective and safe therapy for hepatocellular carcinoma adjacent to major hepatic veins.,” *Eur. Radiol.*, vol. 19, no. 2, pp. 437–45, Feb. 2009.

[35] T. A. Jones, J. Chin, D. Mcleod, J. Barkin, A. Pantuck, and L. S. Marks, “High Intensity Focused Ultrasound for Radio-Recurrent Prostate Cancer: A North American Clinical Trial,” *J. Urol.*, vol. 199, no. 1, pp. 133–139, 2017.

[36] K. Hynynen, “MRI-guided focused ultrasound treatments,” *Ultrasonics*, vol. 50, no. 2, pp. 221–229, 2010.

[37] L. G. Merckel, L. W. Bartels, M. O. Köhler, H. J. G. D. van den Bongard, R. Deckers, W. P. T. M. Mali, C. a Binkert, C. T. Moonen, K. G. a Gilhuijs, and M. a a J. van den Bosch, "MR-guided high-intensity focused ultrasound ablation of breast cancer with a dedicated breast platform.," *Cardiovasc. Intervent. Radiol.*, vol. 36, no. 2, pp. 292–301, Apr. 2013.

[38] T. D. Khokhlova, Y.-N. Wang, J. C. Simon, B. W. Cunitz, F. Starr, M. Paun, L. A. Crum, M. R. Bailey, and V. A. Khokhlova, "Ultrasound-guided tissue fractionation by high intensity focused ultrasound in an in vivo porcine liver model," *Proc. Natl. Acad. Sci.*, vol. 111, no. 22, pp. 8161–8166, 2014.

[39] T. Li, H. Chen, T. Khokhlova, Y.-N. Wang, W. Kreider, X. He, and J. H. Hwang, "Passive cavitation detection during pulsed HIFU exposures of ex vivo tissues and in vivo mouse pancreatic tumors.," *Ultrasound Med. Biol.*, vol. 40, no. 7, pp. 1523–34, Jul. 2014.

[40] E. Vlaisavljevich, Y. Y. Durmaz, A. Maxwell, M. Elsayed, and Z. Xu, "Nanodroplet-mediated histotripsy for image-guided targeted ultrasound cell ablation.," *Theranostics*, vol. 3, no. 11, pp. 851–64, Jan. 2013.

[41] J. Rassweiler, M.-C. Rassweiler, T. Frede, and P. Alken, "Extracorporeal shock wave lithotripsy: An opinion on its future," *Indian J. Urol.*, vol. 30, no. 1, p. 73, 2014.

[42] E. Vlaisavljevich, A. Maxwell, M. Warnez, E. Johnsen, C. A. Cain, and Z. Xu, "Histotripsy-induced cavitation cloud initiation thresholds in tissues of different mechanical properties.," *IEEE Trans. Ultrason. Ferroelectr. Freq. Control*, vol. 61, no. 2, pp. 341–52, Feb. 2014.

[43] K. Kieran, T. L. Hall, J. E. Parsons, J. S. Wolf, J. B. Fowlkes, C. a Cain, and W. W. Roberts, "Refining histotripsy: defining the parameter space for the creation of nonthermal lesions with high intensity, pulsed focused ultrasound of the in vitro kidney.," *J. Urol.*, vol. 178, no. 2, pp. 672–6, Aug. 2007.

[44] B. Hildebrandt, "The cellular and molecular basis of hyperthermia," *Crit. Rev. Oncol. Hematol.*, vol. 43, no. 1, pp. 33–56, Jul. 2002.

[45] C. Lafon, V. Zderic, M. L. Noble, J. C. Yuen, P. J. Kaczkowski, O. a. Sapozhnikov, F. Chavrier, L. a. Crum, and S. Vaezy, "Gel phantom for use in high-intensity focused ultrasound dosimetry," *Ultrasound Med. Biol.*, vol. 31, no. 10, pp. 1383–1389, 2005.

[46] Y. Kim, H. K. Lim, H. Rhim, and M. W. Lee, "Best Practice & Research Clinical Gastroenterology Ablation of hepatocellular carcinoma," *Best Pract. Res. Clin. Gastroenterol.*, vol. 28, no. 5, pp. 897–908, 2014.

[47] P. Kornprat and W. Jarnagin, "Role of intraoperative thermoablation combined with resection in the treatment of hepatic metastasis from colorectal cancer," *Arch. …*, vol. 142, no. 11, pp. 1087–1092, 2007.

[48] J. C. Hu, A. Laviana, and A. Sedrakyan, "High-Intensity Focused Ultrasound for Prostate Cancer," *Jama*, vol. 315, no. 24, p. 2659, 2016.

[49] A. C. Y. Chan, T. T. Cheung, S. T. Fan, K. S. H. Chok, S. C. Chan, R. T. P. Poon, and C. M. Lo, “Survival analysis of high-intensity focused ultrasound therapy versus radiofrequency ablation in the treatment of recurrent hepatocellular carcinoma.,” *Ann. Surg.*, vol. 257, no. 4, pp. 686–92, Apr. 2013.

[50] F. Wu, Z.-B. Wang, W. Chen, J. Zou, J. Bai, H. Zhu, K. Li, C. Jin, F. Xie, and H. Su, “Advanced hepatocellular carcinoma: treatment with high-intensity focused ultrasound ablation combined with transcatheter arterial embolization.,” *Radiology*, vol. 235, no. 2, pp. 659–67, May 2005.

[51] Y. Kim, B. Keserci, A. Partanen, H. Rhim, H. K. Lim, M. J. Park, and M. O. Köhler, “Volumetric MR-HIFU ablation of uterine fibroids: role of treatment cell size in the improvement of energy efficiency.,” *Eur. J. Radiol.*, vol. 81, no. 11, pp. 3652–9, Nov. 2012.

[52] E. D. Louis, R. Ottman, and a Hauser, “How common is the most common adult movement disorder? Estimates of the Prevelence of essential tremor thoughout the world,” *Mov. Disord.*, vol. 13, no. 1, pp. 5–10, 1998.

[53] P. R. Lyons KE, “Deep brain stimulation and tremor,” *Neurotherapeutics*, vol. 5, no. 2, pp. 331–338, 2008.

[54] N. Lipsman, T. G. Mainprize, M. L. Schwartz, K. Hynynen, and A. M. Lozano, “Intracranial Applications of Magnetic Resonance-guided Focused Ultrasound,” *Neurotherapeutics*, vol. 11, no. 3, pp. 593–605, 2014.

[55] T. R. Wang, R. F. Dallapiazza, S. Moosa, D. Huss, B. B. Shah, and W. J. Elias, “Thalamic Deep Brain Stimulation Salvages Failed Focused Ultrasound Thalamotomy for Essential Tremor: A Case Report,” *Stereotact. Funct. Neurosurg.*, 2018.

[56] A. Zimmermann, D. Bernuit, C. Gerlinger, M. Schaefers, and K. Geppert, “Prevalence, symptoms and management of uterine fibroids: An international internet-based survey of 21,746 women,” *BMC Womens. Health*, vol. 12, no. 1, p. 6, 2012.

[57] G. K. Hesley, K. R. Gorny, and D. A. Woodrum, “MR-guided focused ultrasound for the treatment of uterine fibroids,” *Cardiovasc. Intervent. Radiol.*, vol. 36, no. 1, pp. 5–13, 2013.

[58] C. M. C. Tempany, E. A. Stewart, N. McDannold, B. J. Quade, F. A. Jolesz, and K. Hynynen, “MR Imaging–guided Focused Ultrasound Surgery of Uterine Leiomyomas: A Feasibility Study,” *Radiology*, vol. 226, no. 3, pp. 897–905, 2003.

[59] F. M. Fennessy, C. M. Tempany, N. J. McDannold, M. J. So, G. Hesley, B. Gostout, H. S. Kim, G. A. Holland, D. A. Sarti, K. Hynynen, F. A. Jolesz, and E. A. Stewart, “Uterine Leiomyomas: MR Imaging–guided Focused Ultrasound Surgery—Results of Different Treatment Protocols [1],” *Radiology*, vol. 243, no. 3, pp. 885–893, 2007.

[60] F. A. Taran, C. M. C. Tempany, L. Regan, Y. Inbar, A. Revel, and E. A. Stewart, “Magnetic resonance-guided focused ultrasound (MRgFUS) compared with abdominal hysterectomy for treatment of uterine leiomyomas,” *Ultrasound Obstet. Gynecol.*, vol. 34, no. 5, pp. 572–578, 2009.

[61] E. V. A. Bouwsma, G. K. Hesley, D. A. Woodrum, A. L. Weaver, P. C. Leppert, L. G. Peterson, and E. A. Stewart, “Comparing focused ultrasound and uterine artery embolization for uterine fibroids - Rationale and design of the Fibroid Interventions: Reducing Symptoms Today and Tomorrow (FIRSTT) trial,” *Fertil. Steril.*, vol. 96, no. 3, pp. 704–710, 2011.

[62] S. Chen, E. Pitre, D. Kaunels, and S. Singh, “Uterine-Preserving Interventions for the Management of Symptomatic Uterine Fibroids : A Systematic Review of Clinical and Cost-Effectiveness,” *Ottawa: CADTH Rapid Response Repport*, no. January, pp. 0–140, 2016.

[63] E. A. Stewart, J. Rabinovici, C. M. C. Tempany, Y. Inbar, L. Regan, B. Gastout, G. Hesley, H. S. Kim, S. Hengst, and W. M. Gedroye, “Clinical outcomes of focused ultrasound surgery for the treatment of uterine fibroids,” *Fertil. Steril.*, vol. 85, no. 1, pp. 22–29, 2006.

[64] G. Pron, J. Bennett, A. Common, J. Wall, M. Asch, and K. Sniderman, “The Ontario Uterine Fibroid Embolization Trial. Part 2. Uterine fibroid reduction and symptom relief after uterine artery embolization for fibroids,” *Fertil. Steril.*, vol. 79, no. 1, pp. 120–127, 2003.

[65] G. Carrafiello, C. Recaldini, F. Fontana, F. Ghezzi, S. Cuffari, D. Laganà, and C. Fugazzola, “Ultrasound-guided radiofrequency thermal ablation of uterine fibroids: Medium-term follow-up,” *Cardiovasc. Intervent. Radiol.*, vol. 33, no. 1, pp. 113–119, 2010.

[66] E. K. Abdalla, “Commentary: Radiofrequency ablation for colorectal liver metastases: do not blame the biology when it is the technology,” *Am. J. Surg.*, vol. 197, no. 6, pp. 737–739, 2009.

[67] R. G. Holt and R. A. Roy, “Measurements of bubble-enhanced heating from focused, Mhz-frequency ultrasound in a tissue-mimicking material,” *Ultrasound Med. Biol.*, vol. 27, no. 10, pp. 1399–1412, Oct. 2001.

[68] J. Wu and W. L. Nyborg, “Ultrasound, cavitation bubbles and their interaction with cells.,” *Adv. Drug Deliv. Rev.*, vol. 60, no. 10, pp. 1103–16, Jun. 2008.

[69] C.-Y. Lai, C.-H. Wu, C.-C. Chen, and P.-C. Li, “Quantitative relations of acoustic inertial cavitation with sonoporation and cell viability.,” *Ultrasound Med. Biol.*, vol. 32, no. 12, pp. 1931–1941, 2006.

[70] D. Needham, G. Anyarambhatla, G. Kong, and M. W. Dewhirst, “A new temperature-sensitive liposome for use with mild hyperthermia: Characterization and testing in a human tumor xenograft model,” *Cancer Res.*, vol. 60, no. 5, pp. 1197–1201, 2000.

[71] A. Kheirolomoom, C. Y. Lai, S. M. Tam, L. M. Mahakian, E. S. Ingham, K. D. Watson, and K. W. Ferrara, “Complete regression of local cancer using temperature-sensitive liposomes combined with ultrasound-mediated hyperthermia,” *J. Control. Release*, vol. 172, no. 1, pp. 266–273, 2013.

[72] A. Gasselhuber, M. R. Dreher, A. Partanen, P. S. Yarmolenko, D. Woods, B. J. Wood, and D. Haemmerich, “Targeted drug delivery by high intensity focused ultrasound mediated hyperthermia combined with temperature-sensitive liposomes: Computational modelling and preliminary in vivo validation,” *Int. J. Hyperth.*, vol. 28, no. 4, pp. 337–348, Jun. 2012.

[73] S. M. Park, M. S. Kim, S. J. Park, E. S. Park, K. S. Choi, Y. S. Kim, and H. R. Kim, "Novel temperature-triggered liposome with high stability: Formulation, in vitro evaluation, and in vivo study combined with high-intensity focused ultrasound (HIFU)," *J. Control. Release*, vol. 170, no. 3, pp. 373–379, 2013.

[74] T. Ta, E. Bartolak-Suki, E. J. Park, K. Karrobi, N. J. McDannold, and T. M. Porter, "Localized delivery of doxorubicin in vivo from polymer-modified thermosensitive liposomes with MR-guided focused ultrasound-mediated heating," *J. Control. Release*, vol. 194, pp. 71–81, 2014.

[75] F. J. FRY, H. W. ADES, and W. J. FRY, "Production of Reversible Changes in the Central Nervous System by Ultrasound," *Science (80-.).*, vol. 127, no. 3289, pp. 83–84, Jan. 1958.

[76] W. J. Tyler, Y. Tufail, M. Finsterwald, M. L. Tauchmann, E. J. Olson, and C. Majestic, "Remote excitation of neuronal circuits using low-intensity, low-frequency ultrasound," *PLoS One*, vol. 3, no. 10, 2008.

[77] H. Kim, A. Chiu, S. D. Lee, K. Fischer, and S. S. Yoo, "Focused ultrasound-mediated non-invasive brain stimulation: Examination of sonication parameters," *Brain Stimul.*, vol. 7, no. 5, pp. 748–756, 2014.

[78] P. P. Ye, J. R. Brown, and K. B. Pauly, "Frequency dependence of ultrasound neurostimulation in the mouse brain," *Ultrasound Med. Biol.*, vol. 42, no. 7, 2016.

[79] T. Deffieux, Y. Younan, N. Wattiez, M. Tanter, P. Pouget, and J. F. Aubry, "Low-intensity focused ultrasound modulates monkey visuomotor behavior," *Curr. Biol.*, vol. 23, no. 23, pp. 2430–2433, 2013.

[80] D. M. Panczykowski, E. A. Monaco, and R. M. Friedlander, "Transcranial Focused Ultrasound Modulates the Activity of Primary Somatosensory Cortex in Humans," *Neurosurgery*, vol. 74, no. 6, pp. N8–N9, Jun. 2014.

[81] W. Lee, H.-C. Kim, Y. Jung, Y. A. Chung, I.-U. Song, J.-H. Lee, and S.-S. Yoo, "Transcranial focused ultrasound stimulation of human primary visual cortex," *Sci. Rep.*, vol. 6, no. September, p. 34026, 2016.

[82] B. Krasovitski, V. Frenkel, S. Shoham, and E. Kimmel, "Intramembrane cavitation as a unifying mechanism for ultrasound-induced bioeffects," *Proc. Natl. Acad. Sci.*, vol. 108, no. 8, pp. 3258–3263, Feb. 2011.

[83] V. Krishna, F. Sammartino, and A. Rezai, "A review of the current therapies, challenges, and future directions of transcranial focused ultrasound technology advances in diagnosis and treatment," *JAMA Neurol.*, vol. 75, no. 2, pp. 246–254, 2018.

[84] S. E. Bullard, M. Griss, S. Greene, and A. Gekker, *Encyclopedia of Clinical Neuropsychology*, vol. 28, no. 1. 2013.

[85] E. A. Neuwelt, P. a Barnett, D. D. Bigner, and E. P. Frenkel, "Effects of adrenal cortical steroids and osmotic blood-brain barrier opening on methotrexate delivery to gliomas in the rodent: the factor of the blood-brain barrier.," *Proc. Natl. Acad. Sci.*, vol. 79, no. 14, pp. 4420–4423, 1982.

[86] K. Hynynen, “the Threshold for Thermally Significant Cavitation in Dog Thigh Muscle Invivo,” *Ultrasound Med. Biol.*, vol. 17, no. 2, pp. 157–169, 1991.

[87] N. McDannold, N. Vykhodtseva, and K. Hynynen, “Blood-Brain Barrier Disruption Induced by Focused Ultrasound and Circulating Preformed Microbubbles Appears to Be Characterized by the Mechanical Index,” *Ultrasound Med. Biol.*, vol. 34, no. 5, pp. 834–840, 2008.

[88] C. D. Arvanitis, N. Vykhodtseva, F. Jolesz, M. Livingstone, and N. McDannold, “Cavitation-enhanced nonthermal ablation in deep brain targets: feasibility in a large animal model,” *J. Neurosurg.*, vol. 124, no. 5, pp. 1450–1459, May 2016.

[89] N. McDannold, N. Vykhodtseva, and K. Hynynen, “Targeted disruption of the blood-brain barrier with focused ultrasound: Association with cavitation activity,” *Phys. Med. Biol.*, vol. 51, no. 4, pp. 793–807, 2006.

[90] H. Kim, M.-A. Park, S. Wang, A. Chiu, K. Fischer, and S.-S. Yoo, “PET/CT imaging evidence of FUS-mediated (18) F-FDG uptake changes in rat brain,” *Med. Phys.*, vol. 40, no. 3, p. 33501, 2013.

[91] R. Alkins, A. Burgess, M. Ganguly, G. Francia, R. Kerbel, W. S. Wels, and K. Hynynen, “Focused ultrasound delivers targeted immune cells to metastatic brain tumors,” *Cancer Res.*, vol. 73, no. 6, pp. 1892–1899, 2013.

[92] R. D. Airan, R. A. Meyer, N. P. K. Ellens, K. R. Rhodes, K. Farahani, M. G. Pomper, S. D. Kadam, and J. J. Green, “Noninvasive Targeted Transcranial Neuromodulation via Focused Ultrasound Gated Drug Release from Nanoemulsions,” *Nano Lett.*, vol. 17, no. 2, pp. 652–659, 2017.

[93] J. A. Gallego-Juarez, “Piezoelectric ceramics and ultrasonic transducers,” *J. Phys. E.*, vol. 22, no. 10, pp. 804–816, Oct. 1989.

[94] L. Bleustein, “A new wave in piezoelectric materials,” *Appl. Phys. Lett.*, vol. 13, no. 1968, pp. 412–413, 1968.

[95] J. Y. Chapelon, D. Cathignol, C. Cain, E. Ebbini, J. U. Kluiwstra, O. A. Sapozhnikov, G. Fleury, R. Berriet, L. Chupin, and J. L. Guey, “New piezoelectric transducers for therapeutic ultrasound,” *Ultrasound Med. Biol.*, vol. 26, no. 1, pp. 153–159, 2000.

[96] G. S. Chen, H. C. Liu, and Y. L. Lin, “Comparison between 1-3 piezocomposite and PZT ceramic for high-intensity focused ultrasound transducer applications,” *AIP Conf. Proc.*, vol. 1481, no. 2012, pp. 47–52, 2012.

[97] K. S. Ramadan, D. Sameoto, and S. Evoy, “A review of piezoelectric polymers as functional materials for electromechanical transducers,” *Smart Mater. Struct.*, vol. 23, no. 3, 2014.

[98] O. Martínez, C. J. Martín, G. Godoy, and L. G. Ullate, “2D array based on fermat spiral,” *Phys. Procedia*, vol. 3, no. 1, pp. 399–406, 2010.

[99] G. R. Lockwood, P. C. Li, M. O’Donnell, and F. Stuart Foster, “Optimizing the radiation pattern of sparse periodic linear arrays,” *IEEE Trans. Ultrason. Ferroelectr. Freq. Control*, vol. 43, no. 1, pp. 7–14, 1996.

[100] E. S. Ebbini, H. Yao, and A. Shrestha, “Dual-Mode Ultrasound Phased Arrays for Image-Guided Surgery,” *Ultrason. Imaging*, vol. 28, no. 2, pp. 65–82, Apr. 2006.

[101] H. Wang, E. S. Ebbini, M. O’Donnell, and C. a. Cain, “Phase aberration correction and motion compensation for ultrasonic hyperthermia phased arrays: experimental results,” *IEEE Trans. Ultrason. Ferroelectr. Freq. Control*, vol. 41, no. I, pp. 34–43, 1994.

[102] P. Vanbaren, C. Simon, C. A. Cain, and E. S. Ebbini, “Array System for Ultrasound Thermotherapy,” pp. 1269–1272, 1996.

[103] H. Kim, A. Chiu, S. Park, and S.-S. Yoo, “Image-guided navigation of single-element focused ultrasound transducer,” *Int. J. Imaging Syst. Technol.*, vol. 22, no. 3, pp. 177–184, 2012.

[104] D. N. Stephens, D. E. Kruse, S. Qin, and K. W. Ferrara, “Design aspects of focal beams from high-intensity arrays,” *IEEE Trans. Ultrason. Ferroelectr. Freq. Control*, vol. 58, no. 8, pp. 1590–1602, 2011.

[105] G. T. Clement, J. Sun, T. Giesecke, and K. Hynynen, “A hemisphere array for non-invasive ultrasound brain therapy and surgery.,” *Phys. Med. Biol.*, vol. 45, no. 12, pp. 3707–19, Dec. 2000.

[106] D. R. Daum and K. Hynynen, “A 256-element ultrasonic phased array system for the treatment of large volumes of deep seated tissue,” *IEEE Trans. Ultrason. Ferroelectr. Freq. Control*, vol. 46, no. 5, pp. 1254–1268, 1999.

[107] A. Hughes, Y. Huang, A. Pulkkinen, M. L. Schwartz, A. M. Lozano, and K. Hynynen, “A numerical study on the oblique focus in MR-guided transcranial focused ultrasound,” *Phys. Med. Biol.*, vol. 61, no. 22, pp. 8025–8043, 2016.

[108] E. S. Ebbini and C. A. Cain, “A spherical-section ultrasound phased array applicator for deep localized hyperthermia,” *IEEE Trans. Biomed. Eng.*, vol. 38, no. 7, pp. 634–643, 1991.

[109] FDA, “Information for Manufacturers Seeking Marketing Clearance of Diagnostic Ultrasound Systems and Transducers,” *Ultrasound*, 2008. [Online]. Available: https://www.fda.gov/downloads/MedicalDevices/DeviceRegulationandGuidance/GuidanceDocuments/ucm070911.pdf.

[110] S. A. Goss, L. A. Frizzell, J. T. Kouzmanoff, J. M. Barich, and J. M. Yang, “Sparse random ultrasound phased array for focal surgery,” *IEEE Trans. Ultrason. Ferroelectr. Freq. Control*, vol. 43, no. 6, pp. 1111–1121, Nov. 1996.

[111] L. A. Frizzell, S. A. Goss, J. T. Kouzmanoff, J. M. Barich, and J. M. Yang, “Sparse random ultrasound phased array for focal surgery,” *IEEE Trans. Ultrason. Ferroelectr. Freq. Control*, vol. 43, no. 6, pp. 1111–1121, Nov. 1996.

[112] L. R. Gavrilov and J. W. Hand, “A theorical assessment of the relative performance of spherical phase arrays for ultraosund surgery,” *IEEE Trans. Ultrason. Ferroelectr. Freq. Control. vol. 47, No. 1, January 2000*, vol. 47, no. 1, pp. 125–139, 2000.

[113] X. Ji, G. F. Shen, J. F. Bai, D. H. Li, Y. Yu, S. Qiao, and Y. Z. Chen, "Multi-element ultrasound phased array applicator for the ablation of deep-seated tissue," *J. Shanghai Jiaotong Univ.*, vol. 16, no. 1, pp. 55–60, 2011.

[114] P. Ramaekers, M. de Greef, R. Berriet, C. T. W. Moonen, and M. Ries, "Evaluation of a novel therapeutic focused ultrasound transducer based on Fermat's spiral," *Phys. Med. Biol.*, vol. 62, no. 12, pp. 5021–5045, 2017.

[115] B. W. Clare and D. L. Kepert, "The optimal packing of circles on a sphere," *J. Math. Chem.*, vol. 6, no. 1, pp. 325–349, 1991.

[116] K. D. Price, V. W. Sin, C. Mougenot, S. Pichardo, T. Looi, A. C. Waspe, and J. M. Drake, "Design and validation of an MR-conditional robot for transcranial focused ultrasound surgery in infants," *Med. Phys.*, vol. 43, no. 9, pp. 4983–4995, 2016.

[117] B. T. Svedin, M. J. Beck, J. R. Hadley, R. Merrill, J. T. de Bever, B. D. Bolster, A. Payne, and D. L. Parker, "Focal point determination in magnetic resonance-guided focused ultrasound using tracking coils," *Magn. Reson. Med.*, vol. 77, no. 6, pp. 2424–2430, 2017.

[118] B. F. Osmanski, G. Montaldo, M. Tanter, and M. Fink, "Aberration correction by time reversal of moving speckle noise," *IEEE Trans. Ultrason. Ferroelectr. Freq. Control*, vol. 59, no. 7, pp. 1575–1583, 2012.

[119] T. Deffieux and E. E. Konofagou, "Numerical Study of a Simple Transcranial Focused Ultrasound System Applied to Blood Brain Barrier Opening," *IEEE Trans. Ultrason. Ferroelectr. Freq. Control*, vol. 57, no. 12, 2010.

[120] A. Partanen, P. S. Yarmolenko, A. Viitala, S. Appanaboyina, D. Haemmerich, A. Ranjan, G. Jacobs, D. Woods, J. Enholm, B. J. Wood, and M. R. Dreher, "Mild hyperthermia with magnetic resonance-guided high-intensity focused ultrasound for applications in drug delivery," *Int. J. Hyperth.*, vol. 28, no. 4, pp. 320–336, 2012.

[121] R. O. Illing, J. E. Kennedy, F. Wu, G. R. Ter Haar, A. S. Protheroe, P. J. Friend, F. V. Gleeson, D. W. Cranston, R. R. Phillips, and M. R. Middleton, "The safety and feasibility of extracorporeal high-intensity focused ultrasound (HIFU) for the treatment of liver and kidney tumours in a Western population," *Br. J. Cancer*, vol. 93, no. 8, pp. 890–895, 2005.

[122] F. Marquet, M. Pernot, J.-F. Aubry, G. Montaldo, L. Marsac, M. Tanter, and M. Fink, "Non-invasive transcranial ultrasound therapy based on a 3D CT scan: protocol validation and *in vitro* results," *Phys. Med. Biol.*, vol. 54, no. 9, pp. 2597–2613, 2009.

[123] A. F. Hinsche and R. M. Smith, "Image-guided surgery," *Curr. Orthop.*, vol. 15, no. 4, pp. 296–303, 2001.

[124] D. E. Azagury, M. M. Dua, J. C. Barrese, J. M. Henderson, N. C. Buchs, F. Ris, J. M. Cloyd, J. B. Martinie, S. Razzaque, S. Nicolau, L. Soler, J. Marescaux, and B. C. Visser, "Image-guided surgery," *Curr. Probl. Surg.*, vol. 52, no. 12, pp. 476–520, 2015.

[125] F. Lindseth, T. Lang, T. Selbekk, R. Hansen, I. Reinertsen, C. Askeland, O. Solheim, G. Unsgrd, R. Mrvik, and T. A. Nagelhus Hernes, "Ultrasound-Based Guidance and Therapy," in *Advancements and Breakthroughs in Ultrasound Imaging*, InTech, 2013.

[126] D. P. Perrin, N. V. Vasilyev, P. Novotny, J. Stoll, R. D. Howe, P. E. Dupont, I. S. Salgo, and P. J. del Nido, "Image Guided Surgical Interventions," *Curr. Probl. Surg.*, vol. 46, no. 9, pp. 730–766, 2009.

[127] J. B. West and C. R. Maurer, "Designing optically tracked instruments for image-guided surgery," *IEEE Trans. Med. Imaging*, vol. 23, no. 5, pp. 533–545, 2004.

[128] J. M. Fitzpatrick, J. B. West, and C. R. Maurer, "Predicting error in rigid-body point-based registration," *IEEE Trans. Med. Imaging*, vol. 17, no. 5, pp. 694–702, 1998.

[129] M. I. Miga, D. W. Roberts, F. E. Kennedy, L. A. Platenik, A. Hartov, K. E. Lunn, and K. D. Paulsen, "Modeling of retraction and resection for intraoperative updating of images," *Neurosurgery*, vol. 49, no. 1, pp. 75–85, 2001.

[130] R. H. Conley, I. M. Meszoely, J. A. Weis, T. S. Pheiffer, L. R. Arlinghaus, T. E. Yankeelov, and M. I. Miga, "Realization of a biomechanical model-assisted image guidance system for breast cancer surgery using supine MRI," *Int. J. Comput. Assist. Radiol. Surg.*, vol. 10, no. 12, pp. 1985–1996, 2015.

[131] R. Steinmeier, J. Rachinger, M. Kaus, O. Ganslandt, W. Huk, and R. Fahlbusch, "Factors influencing the application accuracy of neuronavigation systems," *Stereotact. Funct. Neurosurg.*, vol. 75, no. 4, pp. 188–202, 2000.

[132] J. M. Fitzpatrick, "Fiducial registration error and target registration error are uncorrelated," in *Proceedings of SPIE*, 2009, vol. 7261, p. 726102.

[133] J. B. West and J. M. Fitzpatrick, "The Distribution of Target Registration Error in Rigid-Body, Point-Based Registration," *Inf. Process. Med. Imaging 1999*, vol. 20, no. 9, pp. 460–465, 1999.

[134] R. F. Labadie, B. M. Davis, and J. M. Fitzpatrick, "Image-guided surgery: What is the accuracy?," *Curr. Opin. Otolaryngol. Head Neck Surg.*, vol. 13, no. 1, pp. 27–31, 2005.

[135] W. Lee, H. Kim, Y. Jung, I.-U. Song, Y. A. Chung, and S.-S. Yoo, "Image-guided transcranial focused ultrasound stimulates human primary somatosensory cortex.," *Sci. Rep.*, vol. 5, p. 8743, 2015.

[136] P. Zhang, J. A. Kopechek, and T. M. Porter, "The impact of vaporized nanoemulsions on ultrasound-mediated ablation.," *J. Ther. ultrasound*, vol. 1, p. 2, Jan. 2013.

[137] C. Desjouy, A. Poizat, B. Gilles, C. Inserra, and J.-C. Bera, "Control of inertial acoustic cavitation in pulsed sonication using a real-time feedback loop system.," *J. Acoust. Soc. Am.*, vol. 134, no. 2, pp. 1640–6, 2013.

[138] N. Hockham, C. C. Coussios, and M. Arora, "A real-time controller for sustaining thermally relevant acoustic cavitation during ultrasound therapy," *IEEE Trans. Ultrason. Ferroelectr. Freq. Control*, vol. 57, no. 12, pp. 2685–2694, 2010.

[139] P. Novák, E. G. Moros, J. J. Parry, B. E. Rogers, R. J. Myerson, a Zeug, J. E. Locke, R. Rossin, W. L. Straube, and a K. Singh, “Experience with a small animal hyperthermia ultrasound system (SAHUS): report on 83 tumours.,” *Phys. Med. Biol.*, vol. 50, no. 21, pp. 5127–39, Nov. 2005.

[140] T. Ta, E. Bartolak-Suki, E. J. Park, K. Karrobi, N. J. McDannold, and T. M. Porter, “Localized delivery of doxorubicin in vivo from polymer-modified thermosensitive liposomes with MR-guided focused ultrasound-mediated heating,” *J. Control. Release*, vol. 194, pp. 71–81, 2014.

[141] K. W. Ferrara, “Driving delivery vehicles with ultrasound,” *Adv. Drug Deliv. Rev.*, vol. 60, no. 10, pp. 1097–1102, 2008.

[142] D. L. Miller and C. Dou, “The potential for enhancement of mouse melanoma metastasis by diagnostic and high-amplitude ultrasound,” *Ultrasound Med. Biol.*, vol. 32, no. 7, pp. 1097–1101, 2006.

[143] J. R. McLean and A. J. Mortimer, “A cavitation and free radical dosimeter for ultrasound,” *Ultrasound Med. Biol.*, vol. 14, no. 1, pp. 59–64, 1988.

[144] E. Y. Lau, M. L. Berkowitz, and E. Schwegler, “Shock Wave-Induced Damage of a Protein by Void Collapse,” *Biophys. J.*, vol. 110, no. 1, pp. 147–156, 2016.

[145] M. Lafond, J. L. Mestas, F. Prieur, K. Chettab, S. Geraci, P. Clézardin, and C. Lafon, “Unseeded Inertial Cavitation for Enhancing the Delivery of Chemotherapies: A Safety Study,” *Ultrasound Med. Biol.*, vol. 42, no. 1, pp. 220–231, 2015.

[146] E. S. Ebbini and C. a Cain, “Multiple-focus ultrasound phased-array pattern synthesis: optimal driving-signal distributions for hyperthermia.,” *IEEE Trans. Ultrason. Ferroelectr. Freq. Control*, vol. 36, no. 5, pp. 540–8, Jan. 1989.

[147] M. O. Köhler, C. Mougenot, B. Quesson, J. Enholm, B. Le Bail, C. Laurent, C. T. W. Moonen, and G. J. Ehnholm, “Volumetric HIFU ablation guided by multiplane MRI thermometry,” *AIP Conf. Proc.*, vol. 1113, no. 2009, pp. 228–230, 2009.

[148] C. Coviello, R. Kozick, J. Choi, M. Gyöngy, C. Jensen, P. P. Smith, and C.-C. Coussios, “Passive acoustic mapping utilizing optimal beamforming in ultrasound therapy monitoring.,” *J. Acoust. Soc. Am.*, vol. 137, no. 5, p. 2573, 2015.

[149] V. Rieke and K. B. Pauly, “MR thermometry,” *J. Magn. Reson. Imaging*, vol. 27, pp. 376–390, 2008.

[150] C. D. Arvanitis, M. S. Livingstone, and N. McDannold, “Combined ultrasound and MR imaging to guide focused ultrasound therapies in the brain.,” *Phys. Med. Biol.*, vol. 58, no. 14, pp. 4749–61, 2013.

[151] C. H. Farny, R. G. Holt, and R. A. Roy, “Temporal and Spatial Detection of HIFU-Induced Inertial and Hot-Vapor Cavitation with a Diagnostic Ultrasound System,” *Ultrasound Med. Biol.*, vol. 35, no. 4, pp. 603–615, 2009.

[152] Z. Kyriakou, M. I. Corral-Baques, A. Amat, and C. C. Coussios, “HIFU-Induced Cavitation and Heating in Ex Vivo Porcine Subcutaneous Fat,” *Ultrasound Med. Biol.*, vol. 37, no. 4, pp. 568–579, 2011.

[153] K. J. Haworth, V. A. Salgaonkar, N. M. Corregan, C. K. Holland, and T. D. Mast, “Using Passive Cavitation Images to Classify High-Intensity Focused Ultrasound Lesions,” *Ultrasound Med. Biol.*, vol. 41, no. 9, pp. 2420–2434, Sep. 2015.

[154] M. E. Poorman, V. L. Chaplin, K. Wilkens, M. D. Dockery, T. D. Giorgio, W. A. Grissom, and C. F. Caskey, “Open-source, small-animal magnetic resonance-guided focused ultrasound system,” *J. Ther. Ultrasound*, vol. 4, no. 1, p. 22, 2016.

[155] X. Wu and M. Sherar, “Theoretical evaluation of moderately focused spherical transducers and multi-focus acoustic lens/transducer systems for ultrasound thermal therapy.,” *Phys. Med. Biol.*, vol. 47, no. 9, pp. 1603–21, May 2002.

[156] A. D. Wiles, A. Likholyot, D. D. Frantz, and T. M. Peters, “A statistical model for point-based target registration error with anisotropic fiducial localizer error,” *IEEE Trans. Med. Imaging*, vol. 27, no. 3, pp. 378–390, 2008.

[157] N. McDannold and S. E. Maier, “Magnetic resonance acoustic radiation force imaging,” *Med. Phys.*, vol. 35, no. 8, p. 3748, 2008.

[158] Y. Hertzberg, a Volovick, Y. Zur, Y. Medan, S. Vitek, and G. Navon, “Ultrasound focusing using magnetic resonance acoustic radiation force imaging: application to ultrasound transcranial therapy.,” *Med. Phys.*, vol. 37, no. 2010, pp. 2934–2942, 2010.

[159] J. L. B. Robertson, B. T. Cox, J. Jaros, and B. E. Treeby, “Accurate simulation of transcranial ultrasound propagation for ultrasonic neuromodulation and stimulation,” *J. Acoust. Soc. Am.*, vol. 141, no. 3, pp. 1726–1738, 2017.

[160] G. W. Miller, M. Eames, J. Snell, and J. F. Aubry, “Ultrashort echo-time MRI versus CT for skull aberration correction in MR-guided transcranial focused ultrasound: In vitro comparison on human calvaria,” *Med. Phys.*, vol. 42, no. 5, pp. 2223–2233, 2015.

[161] N. Liu, A. Liutkus, and J. Aubry, “Random calibration for accelerating MR-ARFI guided ultrasonic focusing in transcranial therapy,” *Phys. Med. Biol.*, vol. 60, p. 1069, 2015.

[162] W. Lee, Y. A. Chung, Y. Jung, I.-U. Song, and S.-S. Yoo, “Simultaneous acoustic stimulation of human primary and secondary somatosensory cortices using transcranial focused ultrasound,” *BMC Neurosci.*, vol. 17, no. 1, p. 68, 2016.

[163] G. Malietzis, L. Monzon, J. Hand, H. Wasan, E. Leen, M. Abel, A. Muhammad, P. Price, and P. Abel, “High-intensity focused ultrasound: Advances in technology and experimental trials support enhanced utility of focused ultrasound surgery in oncology,” *Br. J. Radiol.*, vol. 86, no. 1024, 2013.

[164] A. Payne, U. Vyas, N. Todd, J. de Bever, D. a Christensen, and D. L. Parker, “The effect of electronically steering a phased array ultrasound transducer on near-field tissue heating.,” *Med. Phys.*, vol. 38, no. 9, pp. 4971–81, Sep. 2011.

[165] U. Vyas, E. Kaye, and K. B. Pauly, “Transcranial phase aberration correction using beam simulations and MR-ARFI,” *AIP Conf. Proc.*, vol. 1503, pp. 185–190, 2012.

[166] L. Marsac, D. Chauvet, B. Larrat, M. Pernot, B. Robert, M. Fink, a L. Boch, J. F. Aubry, and M. Tanter, “MR-guided adaptive focusing of therapeutic ultrasound beams in the human head.,” *Med. Phys.*, vol. 39, no. 2, pp. 1141–9, Feb. 2012.

[167] E. a. Kaye, Y. Hertzberg, M. Marx, B. Werner, G. Navon, M. Levoy, and K. B. Pauly, “Application of Zernike polynomials towards accelerated adaptive focusing of transcranial high intensity focused ultrasound,” *Med. Phys.*, vol. 39, no. October, p. 6254, 2012.

[168] P. Reynolds, J. Hyslop, and G. Hayward, “Analysis of spurious resonances in single and multi-elfment piezocomposite ultrasonic transducers,” *IEEE Symp. Ultrason. 2003*, vol. 2, no. c, pp. 1650–1653, 2003.

[169] J. K. Mueller, L. Ai, P. Bansal, and W. Legon, “Computational exploration of wave propagation and heating from transcranial focused ultrasound for neuromodulation,” *J. Neural Eng.*, vol. 13, no. 5, p. 56002, 2016.

[170] C. Constans, T. Deffieux, P. Pouget, M. Tanter, and J. F. Aubry, “A 200-1380-kHz Quadrifrequency Focused Ultrasound Transducer for Neurostimulation in Rodents and Primates: Transcranial in Vitro Calibration and Numerical Study of the Influence of Skull Cavity,” *IEEE Trans. Ultrason. Ferroelectr. Freq. Control*, vol. 64, no. 4, 2017.

[171] J. Ling, A. Kurzawski, and J. Templeton, “Reynolds averaged turbulence modelling using deep neural networks with embedded invariance,” *J. Fluid Mech.*, vol. 807, no. May, pp. 155–166, 2016.

[172] J. Tompson, K. Schlachter, P. Sprechmann, and K. Perlin, “Accelerating Eulerian Fluid Simulation With Convolutional Networks,” 2016.

[173] J. Flynn, I. Neulander, J. Philbin, and N. Snavely, “DeepStereo: Learning to Predict New Views from the World’s Imagery,” 2015.

[174] S. Pichardo, C. Moreno-Hernández, R. Andrew Drainville, V. Sin, L. Curiel, and K. Hynynen, “A viscoelastic model for the prediction of transcranial ultrasound propagation: Application for the estimation of shear acoustic properties in the human skull,” *Phys. Med. Biol.*, vol. 62, no. 17, 2017.

[175] B. Larrat, M. Pernot, J.-F. Aubry, E. Dervishi, R. Sinkus, D. Seilhean, Y. Marie, a-L. Boch, M. Fink, and M. Tanter, “MR-guided transcranial brain HIFU in small animal models.,” *Phys. Med. Biol.*, vol. 55, no. 2, pp. 365–88, Jan. 2010.